McGill

A Prototype Modular Detector Design for High Resolution Positron Emission Tomography Imaging

Nan Zhang

Biomedical Engineering Department
McGill University, Montreal

January, 2003

A thesis submitted to the Faculty of Graduate Studies and Research in partial fulfilment of the requirements of the degree of Doctor of Philosophy in Biomedical Engineering

Your file Votre référence
ISBN: 0-612-88605-0
Our file Notre référence
ISBN: 0-612-88605-0

ACKNOWLEDGMENTS

My sincerest thanks go to my supervisor, Dr. Christopher J. Thompson, for his constant encouragement, advice, patience, and guidance over this project. This work would not have been possible without his support.

My grateful acknowledgment is also given to my supervisory committee, Dr. Henrietta L. Galliana in the Biomedical Engineering Department, Dr. Bruce Pike and Dr. Ernst Meyer in the Montreal Neurological Institute, for their guidance throughout the project.

I would like to acknowledge my friends and colleagues in the Research Computing Laboratory of the Montreal Neurological Institute, Marie-Laure A. Camborde, Francois Cayouette, Khanh Q. Nguyen, and Dylan Togane, for their support and contribution in this project. I would like to thank in particular Francois Cayouette, his computer engineering expertise and insight knowledge on scintillation simulation was greatly appreciated.

Many thanks to Toula Papadopoulos, Dean Jolly, and Shadreck Mzengeza in the Montreal Neurological Institute, Steve Kecani and Eddie del Campo in the Physics Department, for their assistance and advice in this project.

My deepest gratitude goes to my wife, Amy Jin Zhang, for her understanding, patience, tolerance, and support. Thank my sons, Larry and Eric, who are the constant sources of inspiration and diversion.

This thesis is dedicated to my mother Gui-Rong Che and my father Chun-Gao Zhang, for their immutable encouragement and perspective.

ABSTRACT

Current challenges facing us in developing dedicated positron emission tomography (PET) systems for metabolic breast mammography (PEM) and small animal (ANIPET) are to achieve high spatial resolution (less than 2 mm) and high efficiency. It is also crucial to extend the sensitive areas of PEM detectors to their periphery in order to overcome the difficulty in imaging near a patient's chest wall. This limitation of the periphery dead region was revealed in the clinical trials of our previously developed PEM-I system.

In the new study, we developed prototype detectors by using position-sensitive photomultiplier tubes (PS-PMTs) and pixelated bismuth germanate (BGO) crystals with depth encoding scheme to detect and localize gamma rays. We used the following methods in crystal processing:

- Crystal cutting - each crystal block was cut by diamond saw into small elements of 2.1 mm x 2.1 mm (2.2 mm pitch) on two opposite faces. The elements on one face of the block offset by half the crystal pitch from those on the opposite face in both X and Y dimensions. The depths of two layers were 11.5 mm and 6.5 mm, respectively. The middle solid space between the two layers was 2 mm.
- Crystal polishing and encapsulating - The very roughly cut surfaces were chemically polished by acid etching method and the cut slots were encapsulated with an epoxy-compound mixture.
- Crystal separating - the pseudo discrete crystal blocks were cut along the middle solid space into two discrete segments.
- Crystal coupling - the two crystal segments were glued together and optically coupled to the PS-PMTs window.

We also developed front-end electronic circuits including high-voltage dividers, anode resistor chains, position readout circuits, and last-dynode timing circuits. Methods for combining four PS-PMTs with simple X+, X-, Y+, Y- outputs have been developed to further simplify the position recording. The detectors were constructed in the structure of arrays (two in the system) - modules (four in each array) - units (four in each module). The basic unit of one crystal and one PS-PMT was formed as field replaceable unit. The acquired list-mode data were analyzed with MATLAB and C. Different methods to generate distortion look-up-table were examined and evaluated.

Our new prototype detectors have spatial resolutions of 1.8 mm (vs. 2.8 mm in PEM-I), timing resolution of 10.3 ns (vs. 12 ns in PEM-I), and a field-of-view of 88 mm x 88 mm (vs. 64 mm x 56 mm in PEM-I). Our analysis shows that the design improves the spatial resolution, enhances the detector field-of-view, and significantly reduces the peripheral dead regions.

RÉSUMÉ

Les défis actuels qui nous font faces quant au développement du système de la tomographie par émission de positrons (PET) pour l'étude métabolique de la mammographie du sein (PEM) et l'étude du petit animal (ANIPET) sont de parvenir à obtenir une haute résolution spatiale (plus petit que 2 mm) ainsi qu'une grande efficacité. Il est aussi crucial d'étendre les zones sensibles à la détection PEM aux endroits plus périphériques et ce afin de surmonter la difficulté de prendre des images près de la cage thoracique. Cette limite au sujet des zones mortes périphériques avait été révélée lors des essais cliniques de notre système précédant le PEM-I.

Dans cette nouvelle étude, nous avons développé des détecteurs prototypes en utilisant des tubes photomultiplicateurs sensibles à la position (PS-PMTs) et des cristaux scintillateurs en germanate de bistmuth (BGO) avec un système de codage à haute résolution pour détecter et localiser les rayons gammas. Les méthodes pour le traitement du cristal qui ont été utilisées sont les suivantes :

- La coupure du cristal – avec une chaîne à diamant, chaque bloc de cristal a été coupé en petits éléments de 2.1 mm x 2.1 mm (2.2 mm d'écartement) sur deux faces opposées. Les éléments sur la face d'un bloc sont décalés de la moitié de l'écartements des cristaux de la face opposée et ce par rapport aux axes X et Y. La profondeur des deux couches sont 11.5 mm et 6.5 mm, respectivement. L'espace solide central entre les deux couches est de 2 mm.
- Le polissage et l'encapsulement du cristal – La surface coupée avec la scié a été polie chimiquement avec l'application d'acide et les entailles ont été encapsulées avec un mélange composé d'époxy.
- La séparation du cristal – Les blocs de cristal distincts ont été coupés au long de l'espace solide central en deux segments distincts.
- La réunion des cristaux – les deux segments de cristal ont été collés ensemble et réunis optiquement à la fenêtre du PS-PMTs.

Nous avons aussi développé des châssis d'électronique incluant des diviseurs à haut voltage, des chaînes de résistances, des circuits lecteurs de position, et enfin des circuits reliés à la mesure du temps. Les méthodes pour combiner les quatre PS-PMTs avec simples sorties X+, X–, Y+, Y– ont été développées pour une plus grande simplification de l'enregistrement de la position. Les détecteurs ont été construits en forme de rangées (deux dans le système) – de modules (quatre pour chacune des rangées) – et d'unités (quatre dans chacun des modules). L'unité de base comprenant un cristal et un PS-PMT a été formée pour être une unité remplaçable. Les données acquises en mode liste ont été analysées avec MATLAB et C. Différentes méthodes pour générer une table de conversion avec distorsion ont été examinées et évaluées.

Nos nouveaux détecteurs prototypes ont une résolution spatiale de 1.8 mm (vs. 2.8 mm avec le PEM-I), une résolution temporelle de 10.3 ns (vs. 12 ns avec le PEM-I) et le champ de vision est de 88 mm x 88 mm (vs. 64 mm x 56 mm avec le PEM-I). Les analyses préliminaires ont montrées que ce modèle améliore la résolution spatiale, augmente la détection du champ de vision et réduit significativement les régions périphériques mortes.

ACRONYMS

ADC	Analog to Digital Converter
APD	Avalanche Photodiode
BGO	Bismuth Germanate
CFA	Current Feedback Amplifier
CT	Computed Tomography
DCI	Delayed Charge Integration
DOI	Depth of Interaction
^{18}F-FDG	2-Fluoro-2-deoxy-D-glucose, fluorine-18 labeled
FOV	Field of View
FWHM	Full Width at Half Maximum
FWTM	Full Width at Tenth Maximum
GSO	Cerium activated Gadolinium Orthosilicate
HV	High Voltage
LSO	Cerium activated Lutetium Oxyorthosilicate
LUT	Look Up Table
MC-PMT	Multi-channel PMT
MRI	Magnetic Resonance Imaging
NaI (Tl)	Thallium activated Sodium Iodide
NIH	National Institutes of Health, U.S.A.
NSS/MIC	Nuclear Science Symposium and Medical Imaging Conference
PCB	Printed Circuit Board
PEM	Positron Emission Mammography
PET	Positron Emission Tomography
PMT	Photomultiplier Tube
PSF	Point Spread Function
PS-PMT	Position-Sensitive Photomultiplier Tube
RSS	Root-Sum-Square

SNR	Signal to Noise Ratio
TAC	Time to Amplitude Converter
Tg	Glass Transition Temperature (Epoxy)
TNS	IEEE Transaction on Nuclear Science
VFA	Voltage Feedback Amplifier

TABLE OF CONTENTS

TABLE OF FIGURES

TABLE OF TABLES

INTRODUCTION

Dedicated Positron Emission Tomography (PET) instruments for small animal (ANIPET system) and metabolic breast imaging (PEM-I) were previously developed in our laboratory of the Montreal Neurological Institute, McGill University. Each system consists of two detectors; each detector is constructed with four 36 mm × 36 mm × 20 mm bismuth germanate (BGO) crystal blocks optical coupled to a position-sensitive photomultiplier tube (PS-PMT) - Hamamatsu R3941-05. Electronic circuits in these detectors include high voltage dividers, crossed anode read-out resistor chains, position preamplifiers, and fast timing amplifiers. The system spatial resolution is 2.8 mm; timing resolution is 12 ns. The detector effective field-of-view is 64 mm × 56 mm.

Our clinical studies with PEM-I system revealed that the detectors have a relatively large peripheral dead region. This is mainly caused by the intrinsic structure of the PS-PMT. The R3941 is a mesh type PS-PMT with a thick glass envelope. The PMT light-photon input window is in a photocathode head-on configuration. The cross-anode outputs have 18 anodes in the X-axis and 16 anodes in the Y-axis. Even though the outer dimension of the PMT is 78 mm × 78 mm, its effective input window, or the effective field-of-view, is only about 60 mm × 54 mm. In the detectors of PEM-I and ANIPET, BGO crystals cover the PMT window in a region of 72 mm × 72 mm. After previous efforts to develop and improve readout weighting matrix for the PMT, we identified crystal elements in the area of 64 mm × 56 mm. However, there are still 7-mm peripheral dead regions in each end of X-axis, 11-mm in each end of Y-axis. Since PMTs can only operate in a light tight environment, inevitably the detector enclosure further enlarges the dead region. In PEM studies, the overall peripheral non-sensitive area limits imaging near a patient's chest wall resulting in degrading diagnostic accuracy and efficiency.

One of the main challenges in PET instrumentation research and development is to achieve high spatial resolution, ideally in less than 2 mm. Even though PET cannot approach the fine resolution attainable from anatomical diagnostic instruments, such as

X-ray radiography, computed tomography (CT) and magnetic resonance imaging (MRI), spatial resolution of 1 to 2 mm is still desirable in organ function studies.

In order to enlarge detector field of view, achieve higher spatial resolution, and reduce the detector peripheral dead region, we developed prototype modular detectors for our proposed PEM-II scanner.

Thesis Outline

The thesis consists of seven chapters organized as follows.

Chapter 1, "Primary Physics Principles of Positron Emission Tomography", is a primary outlook of the physical basis and principles of PET. It also includes a brief description of PMTs and their structures.

Chapter 2, "Overview of Detector Development in Positron Emission Tomography", is a brief overview of the PET detector theories and major detector development in the fields of positron emission mammography (PEM) and animal PET.

Chapter 3, "Improving the Performance of Small Planar Detectors of PEM-I and ANIPET System", describes our investigated techniques to improve the performance of PEM-I and ANIPET detector. This work was presented at the IEEE 2000 Nuclear Science Symposium and Medical Imaging Conference (NSS/MIC) in Lyon France, and published in the IEEE Transaction on Nuclear Science (TNS) (February 2002).

Chapter 4, "Crystal Process in Prototype PEM-II Detector", describes the detailed crystal processing techniques that we investigated for our PEM-II detector. The work was presented at the IEEE 2002 NSS/MIC in Norfolk, Virginia U.S.A., and submitted to IEEE TNS (November 2002).

Chapter 5, "Front-End Analog Circuits in the Prototype PEM-II Detector", presents the electronic circuits that we designed and developed for our PEM-II detector. This work was presented at the IEEE 2001 NSS/MIC in San Diego, California U.S.A., and published in the IEEE TNS (October 2002).

Chapter 6, "Optimize Position Readout Circuits in PET Front-End Electronics", presents a theoretical analysis of the front-end electronic circuits for PET detectors. The methods we investigated for front-end electronics adjustment could be useful for general

PET detectors. The work was presented at the IEEE 2002 NSS/MIC in Norfolk, Virginia U.S.A., and submitted to IEEE TNS (November 2002).

Chapter 7, "Detector Evaluation and Results", illustrates the evaluation methods and shows the results on this project.

Appendix lists following documents: (1) A sample record of the "BGO Crystal Cutting Record"; (2) A record of "The Encapsulating Record of Mixing Epoxy EPO-TEK 301-2 with White Paste REN DW-0131"; (3) documents of "Printed Circuit Broads of PMT Socket, Position Integrator, Fast Timing Readout, and Main Amplifier Buffer Circuits"; (4) MATLAB "Crystal Identification Image Processing" software structure.

CHAPTER I

PRIMARY PHYSICS PRINCIPLES OF POSITRON EMISSION TOMOGRAPHY

1.1 Positron Emission Tomography

Positron Emission Tomography (PET) is a medical imaging technology that searches for cancer, damaged heart tissue, brain disorders and other health conditions by seeking signs of abnormal metabolism. It reveals metabolic activity of the cells, gives chemical information about the body, and provides information about function and structure [1]-[3].

PET can detect whether there are cancerous growths and where they are located. When disease strikes, the biochemistry of body tissues and cells change. For instance, cancer cells have higher metabolic rates than normal cells, often feeding on sugars like glucose. If an area is cancerous and consuming glucose, the signals will be stronger there than in surrounding tissue, and show up as a denser region on a PET scan. PET is considered the most accurate way to diagnose whether or not a tumor is benign or malignant, if it has spread, if it is responding to treatment, and if a patient is cancer free after treatment without having to do surgery or a biopsy. It is currently the most effective way to check for cancer recurrences [2].

PET is also useful in diagnosing certain cardiovascular and neurological diseases because it highlights areas with increased, diminished or no metabolic activity, thereby pinpointing problems. It can identify cardiovascular disease by measuring both blood flow (perfusion) and metabolic rate within the heart. PET has significant implications in diagnosing Alzheimer's disease, Parkinson's disease, Epilepsy and other neurological conditions, because it can vividly illustrate areas where brain activity differs from the norm. It is one of the most accurate methods available to localize areas of the brain causing Epileptic seizures and to determine if surgery is a treatment option [2].

PET often reveals illnesses much earlier than conventional diagnostic procedures, so it could eliminate the need for ineffective or unnecessary surgeries, treatments or other diagnostic tests.

Recently, PET is used in conjunction with a MRI and CT scan through "fusion" to give a full three-dimension view of an organ and the location of cancer within it. The latest PET scanners are being made a combination of PET/CT devices, The PET and CT image data sets are registered and fused to form a single image that shows the anatomical location from CT along with the metabolic activity of PET. This new technology delivers a new frontier in medical imaging [4].

1.2 Nuclear Physics in Positron Emission Tomography

1.2.1 Radionuclides Production

Radionuclide Generation

Radionuclides used for radioisotopes in the nuclear medicine are all man-made rather than naturally occurring. They are made from nuclear reactions by bombarding nuclei of stable atoms with subnuclear particles (such as neutrons and protons), so a stable nucleus is converted into one which is unstable and radioactive. The most common methods to make radionuclides for nuclear medicine use nuclear reactors and accelerators.

Nuclear reactors have provided large quantities of radionuclides for nuclear medicine. For example, ^{131}I that is used for hyperthyroid diagnosis and treatment can be generated in a reactor. The reaction of ^{131}I from ^{131}Te is:

$$^{130}Te(n,\gamma)^{131}Te \xrightarrow{\beta^-} {}^{131}I \qquad (1.1)$$

A medical cyclotron is a charged-particle accelerator that is used to produce a variety of radionuclides for nuclear medicine. Some of the most common nuclides used for PET studies are listed in Table 1.1. Cyclotron produced short-lived β^+ emitters, such as ^{11}C, ^{15}O, and ^{13}N, represent elements of the most prevalent in biologic substances (carbon, oxygen, and nitrogen), so they can be used to label various physiologically important

tracers. In addition, the annihilation photons released following β^+ emission from these traces can be utilized for novel three-dimensional imaging PET techniques.

TABLE 1.1. SOME CYCLOTRON-PRODUCED RADIONUCLIDES USED IN PET

Nuclide	Decay mode	Common Production Reaction	Natural Abundance of Target Isotope (%)
^{11}C	β^+ (99+%)	$^{10}B(d, n)^{11}C$ $^{11}B(p, n)^{11}C$	19.7 80.3
^{15}O	β^+ (99.9%)	$^{14}N(d, n)^{15}O$	99.6
^{13}N	β^+ (100%)	$^{12}C(d, n)^{13}N$	98.9
$^{18}F^*$	β^+ (97%), EC	$^{11}Ne(d, \alpha)^{18}F$	90.9

*Note: The radionuclide ^{18}F decays by both positron emission (β^+) and electron capture (EC) competitively - 3 % of the nuclei decay by (EC, γ) and 97 % by (β^+, γ) [1].

Labeled Radionuclides

TABLE 1.2. LISTING OF SOME RADIOLABELS USED IN PET

Nuclide	Half Life (Min)	Maximum Energy- E_β^{max} (MeV)	Maximum Range (H_2O) (mm)	Maximum specific activity (Ci/mol)	Labeled Radiopharmaceuticals
^{11}C	20.4	0.96	4.1	9.22×10^9	^{11}CO, ^{11}C -Methionine, ^{11}C-Thymidine, etc
^{15}O	2.07	1.72	8.2	9.08×10^{10}	$^{15}O_2$, $H_2{}^{15}O$, $C^{15}O$, $C^{15}O_2$, etc.
^{13}N	9.96	1.19	5.39	1.89×10^{10}	$^{13}NH_3$, ^{13}N-amino acid
^{18}F	109.7	0.635	2.39	1.71×10^9	^{18}F-fluorodeoxyglucose

Table 1.2 lists the physical properties of radionuclide ^{18}F, ^{11}C, ^{15}O, ^{13}N, and the labeled radiopharmaceuticals used in PET studies. For example, ^{18}F labeled ^{18}F-fluorodeoxyglucose is used to measure glucose metabolism; ^{15}O labeled $H_2{}^{15}O$, $C^{15}O_2$, and ^{15}O-butanol are used to measure cerebral blood flow; ^{11}C or ^{15}O labeled ^{11}CO, $C^{15}O$ are used to measure cerebral blood volume; ^{15}O labeled $^{15}O_2$ is used to measure oxygen metabolism; ^{11}C labeled ^{11}C-nicotine, ^{11}C-raclopride, ^{11}C-schering are used for receptors;

^{13}N labeled amino acids are used to measure regional metabolism in brain; ^{18}F labeled ^{18}F-Dopa is used to measure dopamine synthesis [5].

1.2.2 Positron Decay and Annihilation

In radionuclide decay by positron emission, a proton in the nucleus is transformed into a neutron and a positively charged electron, or positron (β^+) [1].

$$p^+ \rightarrow n + e^+ + \nu + energy \tag{1.2}$$

The positron (β^+) is the anti-particle to the electron. It is ejected from the nucleus with a neutrino during the decay. The positron undergoes inelastic collisions with atomic electrons of surrounding matter, usually within a few millimeters away from the site of its origin and in about 10^{-9} seconds. The positron then combines with an electron followed by an annihilation reaction, in which the masses of positron and electron are converted into two 511 keV annihilation photons. The two photons in the form of gamma rays leave the site of the annihilation in approximately opposite directions.

$$e^+ + e^- \rightarrow \gamma + \gamma \tag{1.3}$$

The transition energy in (1.2) is divided among the kinetic energy of the positron, the daughter nucleus, and the annihilation photons (2 × 0.511 MeV = 1.022 MeV). In order to occur β^+ decay, the minimum requirement of transition energy is 1.022 MeV. The excess transition energy above 1.022 MeV (or E_β^{max}, which is the transition energy minus 1.022 MeV) is shared between the positron and the daughter nucleus. The average positron energy (kinetic energy) is approximately 1/3 E_β^{max}. Some medical important β^+ radionuclides and their E_β^{max} listed in Table 1.2.

1.2.3 Gamma-ray Interaction

The annihilation 511 keV gamma rays will most likely travel through the surrounding material of the subject (i.e. tissue, fat, and bone) and deposit all or part of their energy into the dense scintillation crystals in PET detectors. The energy transformation from gamma rays to matter is in complex interactions with atoms, nuclei, and electrons. The

two primary interactions regarding 511 keV gamma rays are photoelectric effect and Compton scattering [1][8].

Photoelectric Effect

The photoelectric effect is an atomic absorption process in which the total energy of an incident photon is absorbed in an atom. This process results in ejecting an orbital electron (photoelectron) from the atom. The photoelectron kinetic energy E_{pe} is:

$$E_{pe} = E_p - B_e \tag{1.4}$$

where E_p is primary energy which is the energy of the incident photon, B_e is the binding energy of the liberated electron that is usually ejected from a K or L shell.

Binding energies in low-Z elements (like body tissues) are only a few keV or less, thus causing small factor in photoelectric interactions. However, in heavier elements, the binding energies are in the 20-100 keV range, which may account for a significant fraction of E_p.

Compton Scattering

Compton scattering is a "collision" between a photon and an electron in the outer shell of an atom. The collision results a scattered photon of lower energy and an ejected Compton recoil electron. The energy of the scattered photon is related to the scattering angle θ as:

$$E_{SC} = \frac{E_P}{1 + (1 - \cos\theta)\dfrac{E_P}{0.511}} \tag{1.5}$$

where E_P and E_{SC} are the primary energy (energy of the incident photon) and scattered energy both in MeV; θ is the angle between the path of the scattered photon and the original γ photon.

1.2.4 Intrinsic Spatial Resolution of PET

One of the major challenges of PET and also the most flourishing research topic is the spatial resolution. An empirical study by Moses and Derenzo summarizes the various factors affecting spatial resolution [9]. The spatial resolution (Γ) is given as

$$\Gamma = 1.25 \cdot \sqrt{\left(\frac{d}{2}\right)^2 + (0.0022D^2) + s^2 + b^2} \qquad (1.6)$$

where the factor 1.25 accounts for a resolution degradation resulting from the image reconstruction process; d is the width of each crystal element; D is the detector separation which amplifies the effect of gamma ray non-collinearity; s is the positron range (FWHM); b is the block effect. The block effect accounts for the uncertainty in determining of the event location within a block detector with multiple crystal elements. If the ratio of the crystal elements to coupled PMTs is 1:1, b equals zero.

Intrinsic Limitation on Spatial Resolution

Physical limits on PET spatial resolution are due to the isotope's positron range in tissue, and the non-collinearity of the annihilation photons in the detectors' frame of reference.

- **Positron Range**

The positron range is the finite distance between the location of the positron origin and that of the annihilation. PET coincidence detection can only localizes the gamma rays annihilation position, since the trajectory of the positron is undetermined. This uncertainty results in image blurring and degrades spatial resolution.

The positron range depends upon the energy of the emitted positron and the density of the medium into which the positron is released. This is described as the distribution of the point-spread-function (PSF) [10], which is expressed by the sum of two exponentials. One accounts for small peak at a very short range where a small number of annihilations occur, another introduces broad tails corresponding to the range of the majority of positrons.

For example ^{18}F, which produces a relatively low-energy positron, the resolution broadening due to the positron range is 0.22 mm full width at half maximum (FWHM) and 1.09 mm full width at tenth maximum (FWTM) [1].

- **Angular Distribution of Annihilation Photons**

The two gamma rays emerging from the positron annihilation are actually in approximately opposite directions. The annihilation process must conserve both energy

and momentum. Typically, a positron has 10 eV residual energy prior to annihilation [12]. To conserve momentum, the annihilation gamma rays are slightly non-collinear. The deviation of the angular separation of the gamma rays is described by a Gaussian distribution in water-equivalent materials [13][14].

1.2.5 Scintillator Fundamentals

A scintillation crystal or phosphor is a material that has the ability to convert energy lost by ionizing radiation into pulse of light [6]. They are classified into two major categories - organic and inorganic scintillators [7][8]. The organic scintillator can be present in the solid (crystals or plastics), liquid, or vapor phase [8]. The inorganic scintillator is mainly in a crystal phase, which can be grouped into three following main classes:

- Impurity activated - activator sites are produced by adding impurities to the crystals.
- Self activated - activator sites are produced by a stochiometric excess of one of the constituents of the solid.
- Pure crystals - activator sites are produced by imperfections in the crystal lattice.

Table 1.3 lists some of the common inorganic scintillators and their activated factors. Impurity activated (doped) inorganic crystals like NaI(Tl), GSO and LSO as well as self-activated crystals like BGO are prevalently applied in the detectors of the Nuclear Medicine instrumentation.

TABLE 1.3. INORGANIC SCINTILLATOR EXAMPLES

Classes	Crystals	
Impurity Activated	NaI (Tl)	Thallium activated Sodium Iodide
	CsI (Tl)	Thallium activated Cesium Iodide
	GSO (Ce)	Cerium activated Gadolinium Orthosilicate
	LSO (Ce)	Cerium activated Lutetium Oxyorthosilicate.
Self Activated	CdS	Cadmium Sulfide with excess Cd
	BGO	Bismuth Germanate
Pure Crystals	Diamond	

Normally, organic scintillators are applied in low energy gamma, charged particle counting (alpha or beta detection), and fast timing applications. Inoganic scintillators are used in photon counting, x-ray detection, gamma detection and spectrometers, high and medium energy physics, and nuclear medicine imaging, etc.

Scintillation Mechanism

The main difference between organic and inorganic scintillators is in their scintillation mechanism [6]. Generally, the scintillating of an organic scintillator is known as a function of a single molecular process and is independent of the physical state of the scintillator. On the other hand, an inorganic scintillator requires a crystal lattice to scintillate.

- **Mechanism of Organic Scintillators**

Fig 1.1 shows the fluorescence and phosphorescence processes in organic scintillators. When an excitation occurs, some energy levels in the electron systems of singlet levels S_0, S_1, ..., Sn and triplet levels T_0, T_1, ..., Tn will be populated. The energy level above the S1 level will make rapid transfer (10 to 100 ps) to S1 level without radiation. The transition from the S1 level to S0 level will emit radiation with an energy of about 3-4 eV. Only certain types of molecules release a small fraction (≈ 3%) of the absorbed energy as optical photons. The de-excitation for the S1 level will follow an exponential decay with a time constant of a few nanoseconds. This is considered as the fluorescence process. As can be seen in Fig. 1.1, some excited S-states may be converted into T states. The de-excitations would emit the phosphorescence light in the phosphorescence process.

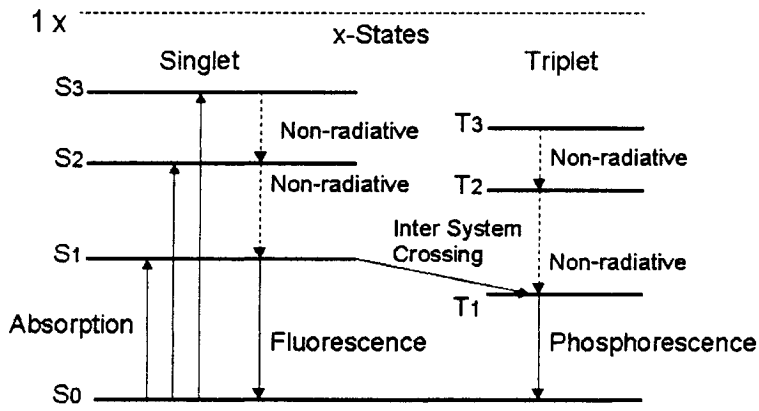

Fig. 1.1. The scintillation mechanism of organic scintillators.

- **Mechanism of Inorganic Scintillators**

Fig. 1.2 shows several energy bands in an inorganic crystal system. In the lower band (valence band), the electrons are bound at lattice sites. In the upper band (conduction band), the electrons are free to move through the crystals. The energy band between these two bands is forbidden band - no electrons can be found in this band in a pure crystal. By implanting impurities in the crystal lattice, energy states called activator sites can be created in the forbidden band, this sites are marked as activator excited states, activator centers and activator ground states.

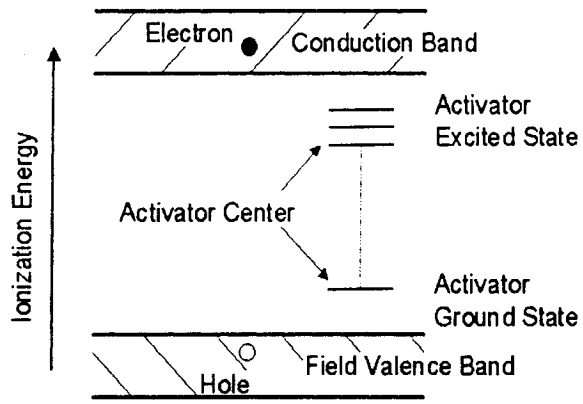

Fig. 1.2. The scintillation mechanism of inorganic scintillators.

When a scintillator absorbs irradiation, a large number of electron-hole pairs (excitons) are formed. The electrons will be excited to the conduction band leaving holes in valence band; the holes will move to the activator sites and ionize them. Then electrons will be attracted to these positive charged activator sites and neutralize them. If the activator center is configured with an allowed transition from excited state to the ground state, excitons will be rapidly de-excited with high probability of the emission of a photon. With a properly chosen activator, the light photons can be produced in such a way with an appropriate energy for detection.

Scintillation Properties

Several important properties of scintillators need to be considered when used in PET detector.

1) Density - Scintillator should be able to stop relatively high-energy gamma rays.

2) Effective Z – High Z and density scintillators present large cross sections for Compton and photoelectric interactions, and therefore offer high linear attenuation coefficient.
3) Decay constant – The light decay time should be relatively short. A long decay constant will require elongated signal integration time, which could cause baseline shift and pile-up effects at higher count rate. The decay time also affects the detector time resolution.
4) Timing resolution - The scintillation timing is dependent on the number of excited electrons, the light decay constant, and the photon emission rate; therefore, it is dependent on the production rate of photoelectrons after an event. Fast timing is crucial, since it largely determines the PET coincidence resolving time.
5) Scintillation efficiency - The scintillator index-of-refraction determines the amount of produced light trapped inside due to the internal reflections. The amount of the collected light will also determine the energy and timing resolution of the detector.
6) Hygroscopicity - Hygroscopic scintillator requires encapsulation in an airtight envelope.

TABLE 1.4. SCINTILLATION PROPERTIES OF SOME COMMON SCINTILLATORS

	NaI(Tl)	BGO	LSO	GSO	BaF_2	CsF
Density (g/cm^3)	3.67	7.13	7.4	6.71	4.89	4.64
Effective Z	50	74	66	59	54	53
Total Linear Attenuation coefficient at 511 keV (cm^{-1})	0.34	0.955	0.870	0.674	0.47	0.44
Average number of photons per keV absorbed	40	4.8	24	6.4	2.0	2.5
Relative light yield	100	15	75	16	4 (fast) 20 (slow)	5
Scintillation decay time (ns)	230	300	40	60	0.6 (fast) 620 (slow)	5
Peak emission wavelength (nm)	410	480	420	410	225 (fast) 310 (slow)	390
Index of refraction	1.85	2.15	1.82	1.85	1.49	1.48
Background radioactivity	No	No	Yes	No	No	No
Hygroscopic	Yes	No	No	No	Slightly	Yes

Note: BaF_2 has two scintillation components

Table 1.4 summarizes some of the common inorganic scintillators used in Nuclear Medicine [3][6][7][15]-[18], which include Thallium-doped Sodium Iodide (NaI(Tl)), Bismuth Germanate ($Bi_4Ge_3O_{12}$, or BGO), Cerium-doped Lutetium Oxyorthosilicate ($Ce:Lu_2SiO_5$ or Ce:LSO). Cesium Fluoride (CsF), Cerium-doped Gadolinium Oxyorthosilicate ($Ce:Gd_2SiO_5$ or Ce:GSO), Barium Fluoride (BaF_2), and Cesium fluoride (CsF).

1.2.6 Scintillation Detector - Photomultiplier Tube

A photomultiplier tube (PMT) is an optoelectronic device that converts light into photoelectrons, amplifies photoelectrons by emission of secondary electrons, then collects the electron signals from the last dynode by anodes. Fig. 1.3 demonstrates the structure and function of a typical PMT [7], which includes the essential elements of a photocathode, a series of dynodes, and an anode.

- Photocathode (cathode) - converts input light flux into electron flux.
- Dynode - multiplies electrons by secondary emission.
- Anode - collects the electron flux and supplies output signals.

The amplification ranges of PMTs are from 10^3 to 10^8, which provide output signal levels suitable for sensitive electronics detection.

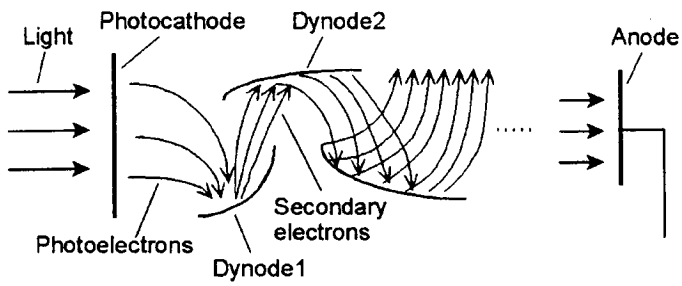

Fig. 1.3. This schematic demonstrates the structure and operation of a photomultiplier tube.

Photoemission and Secondary emission

The fundamental physical processes in PMT operations are photoemission and secondary emission [8]. Photoemission is an emission of electrons resulting from the

action of incident photons on a photocathode surface. The processes in photoemission have three phases:

(1) Photon absorption - absorbed input photon flux impart energy to electrons in the material.

(2) Electron diffusion - energized electrons diffuse through the material.

(3) Electron escape - electrons with sufficient energy escape from the material surface into the vacuum.

Only a fraction of the incident photons on a photoemissive material may cause electron emission. The main factors affecting this quantum efficiency (the ratio of the number of emitted electrons to incident photons) are the wavelength of photons and the properties of the photocathode [8].

Secondary electron emission occurs when incident electrons with sufficient kinetic energy strike the surface of a dynode. Compared with photoemission, secondary emission is caused by the impact of incident electrons rather than photons. The procedures in secondary emission are:

(1) Electron excitation - incident electrons excite the electrons in dynode material to higher energy states.

(2) Electron migrates to the surface - some of the excited electrons move toward the material surface dispensing a fraction of their excess energy.

(3) Electron emission - the surface electrons with energy higher than the surface potential barrier are emitted into the vacuum.

The secondary-emission efficiency is described as the secondary emission coefficient (δ), which is the ratio of the number of secondary electron to the number of the primary electron.

Photomultiplier Tubes in PET Detectors

PMT consists 8 to 19 dynode stages that amplify electrons by a cascade secondary electron emission process. Using low noise electron multiplier, PMT has superior sensitivity of high current amplification and high signal-to-noise ratio. Based on the dynode structures, many different types of PMTs have been employed in PET detectors that include linear-focused type, fine-mesh type, metal-channel type, and micro-channel-plate type [19][20].

- **Linear focused type**

A linear focused type PMT normally has a photocathode in a head-on configuration. It has extremely fast timing response and high pulse linearity. The basic dynode structure and electron-multiplication operation is shown in Fig. 1.3. This type PMT has been broadly used in detectors of Nuclear Medicine instrumentation, such as gamma cameras and PET scanners. Because the PMT with single anode output does not give enough information for position measurement, Anger logic readout scheme is typically required in the application of linear focused PMT [21].

- **Mesh type**

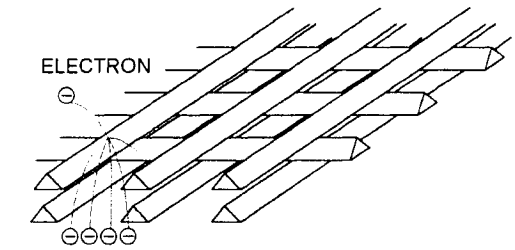

(a). coarse-mesh type

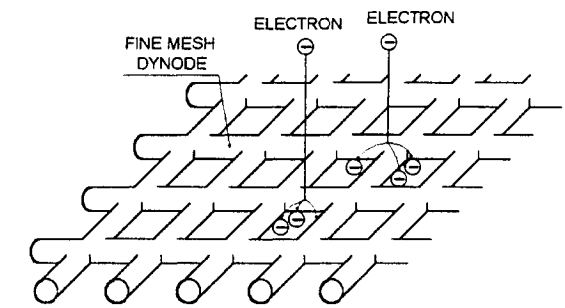

(b). fine-mesh type

Fig. 1.4. This demonstrates the dynode structure of cross-section (a) coarse mesh and (b) fine mesh PS-PMT with electron movement through dynode micro-space.

The mesh type PMT has fine mesh electrodes stacked in close proximity to compose dynodes. There are coarse mesh and fine mesh models, as shown in Fig. 1.4. Normally, the mesh diameter is only about 5 μm and its pitch is approximately 13 μm. It provides high immunity to magnetic field, good uniformity, and high pulse linearity. Furthermore, it has position-sensitive capability when PMT uses cross-anodes readout structure. The PMT is in photocathode head-on configuration with glass envelope structure. Some

models of fine mesh PMT, like PS-PMT R3941, have been used in positron emission mammography and animal PET detectors [22]-[29].

- **Metal channel type**

Metal channel type PMTs are constructed with stacked thin electrodes (Fig. 1.5). It has narrower space between dynode stages than other type of PMTs, so the metal-channel PMT has higher speed response (fast timing response). This type of PMT can be constructed with a metal package instead of traditional glass envelope. The features of compact metal package, very thin stacked electrodes, and very narrow dynode spaces enable the fabrication of metal channel PMT to achieve subminiature (very small and very thin) size. Moreover, As shown in Fig. 1.5, the electron trajectory demonstrates that this type PMT is adequate for position sensitive measurement.

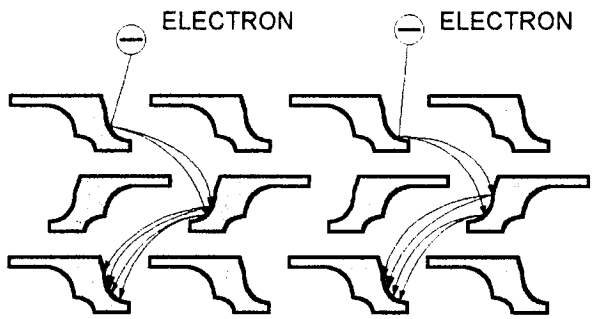

Fig. 1.5. This shows the dynode structure of cross-section metal channel PS-PMT with electron trajectories.

The metal-channel dynode structure and metal package construction make this type PMT very attractive in PET detector application. Two models of this type, R5900U-00-C8 and R7600-00-C12, have been tested in our prototype PET detectors [30].

- **Multi-channel type**

Multi-channel PMT (MC-PMT) can be considered as many PMTs in one small tube envelope. It is actually fabricated with "foil-multiplier" structure. The PMT consists several CuBe foils with a large number (64 or 96) of dynode-shaped multiplication holes, so the secondary electrons stay collimated through dynodes. Therefore, each anode output corresponds to a specific area of the photocathode providing position information.

Multi-channel PMTs feature high spatial resolution, low noise, and low inter-channel crosstalk. MC-PMT XP1722 from Photonics [31] has been used in an animal PET (microPET) system [32].

CHAPTER II

OVERVIEW OF DETECTOR DEVELOPMENT IN POSITRON EMISSION TOMOGRAPHY

2.1 Scintillator Schemes in PET Detectors

2.1.1 Investigations of Scintillation Crystals

The scintillation materials used in PET determine the detector sensitivity, the image resolution, and the count rate capability [4]. The first medical applications with positron technology were made by Dr. W. H. Sweet in the early 1950s [33]. Until 1977, almost all PET imaging systems used NaI(Tl) [34]. Due to its hygroscopic nature, NaI(Tl) is difficult to fabricate. It also has a low density and low effective atomic number, which limits the efficiency to detect 511 keV gamma ray.

In the late 1970s, BGO was introduced into use in PET [35][36]. Compared with NaI(Tl), BGO has a higher density, higher stopping power, and is not hygroscopic. The first actual tomography constructed that employed BGO was designed in 1978 by Dr. C. J. Thompson at the Montreal Neurological Institute [4]. Since then, BGO has been used in the fabrication of most PET system for over 2 decades [4].

As an alternative to BGO, GSO has been investigated for PET application since 1985 [37][38]. Compared with BGO, GSO has higher light output (30% vs. 15% of NaI(Tl)) and much faster decay time (65 ns vs. 300 ns), which reduces the detector dead time and potentially improves detector timing resolution. Recently, GSO based PET scanners that demonstrate spatial resolution of 3.5 mm have been developed for brain studies [39].

The main disadvantage of BGO and GSO is their relatively lower light yield (30% and 15% of NaI(Tl)). Furthermore, GSO has a low stopping power (0.67 cm^{-1}); BGO has slow scintillation decay time (300 ns) so the coincidence time resolution is restricted and coincidence-resolving time needs to be extended.

In the early 1990s, an improvement with the use of LSO crystal was invented by Dr. C. L. Melcher [40][41]. LSO has slightly greater density, slightly lower effective atomic

number, and five times more light output than BGO; moreover, the light output of LSO has 7.5 times faster decay time than BGO. Its overall performance results in a combined speed and light output improvement of 37.5 times over BGO [4].

It seems LSO rather than GSO would be considered a potential substitute of BGO in PET detectors. Even though LSO has superior performance to BGO and GSO, it is very costly. In addition, the produced LSO crystals seem to have considerable variability in the light output [42]. On the other hand, GSO crystals have quite uniform performance in light output and are less expensive than LSO [39].

2.1.2 Block Scintillation Crystal Design

In 1984, Dr. M. E. Casey and Dr. R. Nutt of CPS Innovations invented the concept of the "block" detector [43][44]. The design of BGO block detector has turned out to be extremely successful in high resolution and high efficiency PET cameras. Since 1985, the majority of commercial PET systems have used the concept of the block detector. Table 2.1 shows the specifications of the crystal block [45] in CTI "EXACT HR PET" and "EXACT HR PLUS PET"[46]. Fig. 2.1 shows their block geometry.

TABLE 2.1. DETECTOR BLOCK SPECIFICATION OF "EXACT HR" AND "EXACT HR PLUS"

	EXACT HR	EXACT HR PLUS
Dimension of block (mm)	50×23×30	38×36×30
Block area (mm^2)	1150	1368
Crystal matrix	8×7	8×8
Area/element (mm^2)	20.5	21.4
Dimension of element (mm)	5.2×2.9	4.39×4.05
PMT type	2 × Dual rectangular	4 × 3/4″ round
Coupling area (%)	Approx. 100	Approx. 83

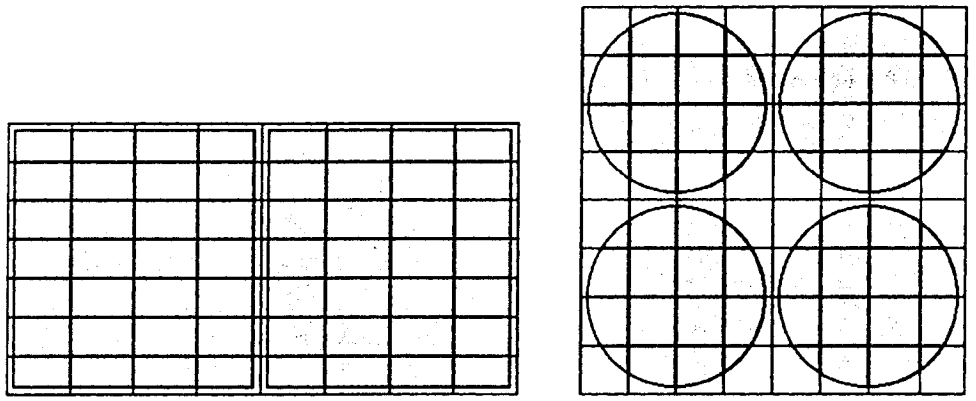

Fig. 2.1. These schematics demonstrate the block detector design of "EXACT HR" and "EXACT HR PLUS" scanners. "EXACT HR" scanners have dual-rectangular PMT and rectangular crystal matrix. "EXACT HR PLUS" scanners have circular PMT and square crystal matrix.

Modular block detector design is prevalently used in the commercial PET (CTI and GE). Most of them employ pseudo-discrete or discrete block configurations [47]-[52]. Fig. 2.2 demonstrates the pseudo-discrete pattern of CTI "EXACT HR PLUS" detectors. As can be seen, each detector module consists of one BGO block and a four PMT matrix. The crystal block is not cut to fully discrete. The cutting uneven grooves in the block controls the light distribution. By applying Anger weighting method [53], the 8 × 8 crystal elements can all be identified. The block crystal can also be cut fully to resolved discrete elements. The light distribution can be controlled by sandwiching a fiber plastic light guide between the crystal block and the PMTs.

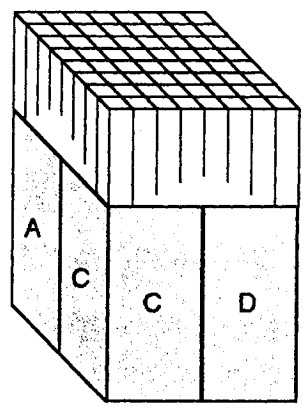

Fig. 2.2. This demonstrates the block design scheme. The crystal was cut to 8 × 8 pseudo-discrete elements; the PMTs were in 2 × 2 matrix.

An alternative method is that the crystal block is directly coupled to PMTs. The crystal block is formed by gluing discrete elements. The light distribution on the PMT windows is controlled by following methods [49][54].

(a) different degrees of polish in the surfaces of the crystal elements;

(b) different coupling material (air or optical coupling) between the crystal elements;

(c) different degrees of encapsulating epoxy mixture (transparent to optical opaque) between the crystal elements.

Fig. 2.3 illustrates the pseudo-discrete and discrete block comparisons between the CTI design and Dr. W.-H. Wong's design for high resolution MDACC PET camera [54]-[56].

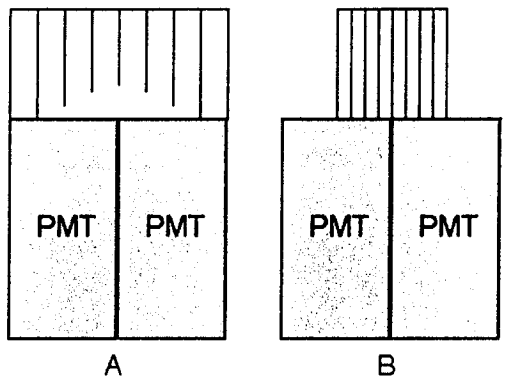

Fig. 2.3. The CTI block detector design is shown in A. The proposed high resolution MDACC PET block detector design is shown in B.

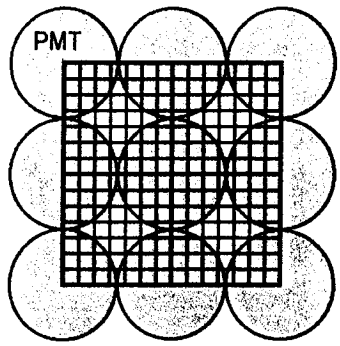

Fig. 2.4. This demonstrates the principle PMT quadrant sharing detector design of MDACC PET camera. Each principle crystal-PMT matrix include 3 × 3 PMTs and 2× 2 BGO crystal blocks.

The PMT and BGO crystal block layout in Fig. 2.3-B allows to cut crystal elements in half size while using the same dimension PMT. This method can improve the detector spatial resolution nearly by half (comparing with Fig. 2.3-A) without using more or smaller PMTs. Fig. 2.4 shows the principle crystal-PMT block matrix of the MDACC

PET detector [57], for which I designed and developed the front-end digital electronic circuits and the coincidence timing master control circuits [57][58].

CTI "EXACT HR PET" used dual-rectangular cross-section PMTs, which provide close to 100% coupling area between the BGO crystal block and PMT input windows. The rectangular or square PMTs are expensive and have very few options. In contrast, the circular cross-section PMTs are much less expensive and are available from many of manufactures, such as Photonis [31], Hamamatsu [59], Burle [60], etc.

Light distribution control is a challenge while using circular PMTs. Some of crystal elements, such as the corner and center elements in "EXACT HR PLUS" detector (Fig. 2.1) and the center elements in MDACC PET detector (Fig. 2.4), have only partial or no overlap between the scintillator and PMT active photocathode regions. In order to identify the crystal elements in these regions, sufficient scintillation light must be collected. The different trials of uneven groove cutting, fiber plastic light guide sharing, and different degree (shape) epoxy mixture painting, are all needed to ensure fully control light distributions.

2.2 Detector Designs in PEM-I and ANIPET Systems

The high resolution, high efficiency PEM-I system and ANIPET system were developed and constructed at the Montreal Neurological Institute of McGill University [22]-[28]. The detectors in PEM and ANIPET systems consist of BGO crystal blocks optically coupled to Hamamatsu R3941-05 PS-PMTs. The detector field-of-view (FOV) is 56 × 64 mm. The PEM-I and ANIPET have a spatial resolution of 2.8 mm, and the timing resolution of 8.7 ns [29].

2.2.1 PMTs and Scintillation Crystals

PS-PMT in PMT-I and ANIPET

Position sensitive PMT (PS-PMT) R3941 [100] is used for PEM-I and ANIPET systems. The PMT is in a glass envelope, with dimension of 77 mm × 77 mm × 70 mm.

Since the envelope is painted with black conductive coating (HV coating) with high voltage potential, it is surrounded with vinyle tape for hazardous protection. The PMT has 16 dynode stages, in a proximity mesh type structure. The gain of the PMT is about 4.0×10^5. The cross anode output wires have 18 in X-axis and 16 in Y-axis. The effective window of the PMT is about 66 mm (X-axis) × 55 mm (Y-axis). The PMT can be operated at a negative high voltage of up to 1300 volts.

The PMT uniformity is measured by illuminating a light spot (light wavelength is 400 nm, spot size 1 mm) via a plastic optical fiber to a PMT window [100]. The uniformity is defined as:

$$Uniformity = \frac{S.D.}{mean} \tag{2.1}$$

where S.D. is the standard deviation.

For example, a R3941 PS-PMT (serial no. AA0366) has a photocathode uniformity of 26.3%; the output gain varies from 47 to 180.

Crystal Schemes for PEM-I and ANIPET

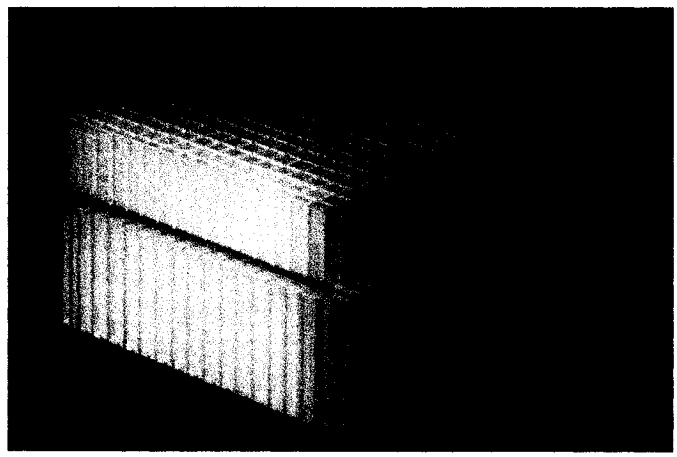

Fig. 2.5. This is a cut BGO scintillation crystal used in the PEM-I and ANIPET detectors. The cuts were made with many passes using three diamond saw blades. Each 2.1 mm × 2.1 mm crystal can be identified to produce high resolution images.

Each detector used in PEM and ANIPET systems consists of four 36 mm × 36 mm × 20 mm bismuth germanate (BGO) crystal blocks coupled to R3941 PS-PMT. As depicted in Fig. 2.5, the crystal blocks were pixelated by diamond saw into small elements of 2.0 mm × 2.0 mm on two opposite faces. The elements on one face of the block offset by half the

crystal pitch from those on the opposite face in both X and Y dimensions. The crystal elements with 11.5-mm depth are coupled to the PS-PMT window. Those with 6.5-mm depth are on the opposite face. This crystal depth scale is based on a Monte Carlo simulation results ensuring an equal probability of gamma ray interaction in each of two layers [22]. The depth-of-interaction (DOI) information can be obtained by identifying the layer in which events occur.

2.2.2 Detector Electronics

The R3941-05 includes a manufactured high-voltage divider, anode resistor chain circuit, and preamplifier (integrator) circuit. The high-voltage divider was designed in such a way that the last dynode signal can be taken out for detector timing. The X and Y-axis anode wires are connected in an Anger resistor chain readout type [21] which provide X^-, X^+, Y^-, Y^+ position signals. The standard resistor chain in this PS-PMT has 1 KΩ resistors between each anode wire. The two resistor-chain outputs in X-axis and two in Y-axis are integrated and buffered (so the outputs can drive 50Ω coax cable) from the preamplifier circuit. The manufacturer sets up the time constant as 2μs. Even though the PMT has 18 (X-axis) and 16 (Y-axis) crossed anode wires, the total position outputs from R3941-05 has only X^-, X^+, Y^-, Y^+ four output signals, which significantly simplifies the electronics complexity.

2.2.3 PEM-I and ANIPET system Outline

PEM-I System Outline

Fig. 2.6 shows the PEM-I and X-ray mammogram (Mammo Diagnost-UC system, Philips, Danbury, CT) co-registration system. The detector assembly is mounted on the mammography magnification table that attaches to the mammography gantry. The two detectors in PEM-I system are attached to a support pole. The upper detector can slide along the supporting pole so that the separation of the two detectors can be adjusted in order to match the thickness of a compressed breast [103].

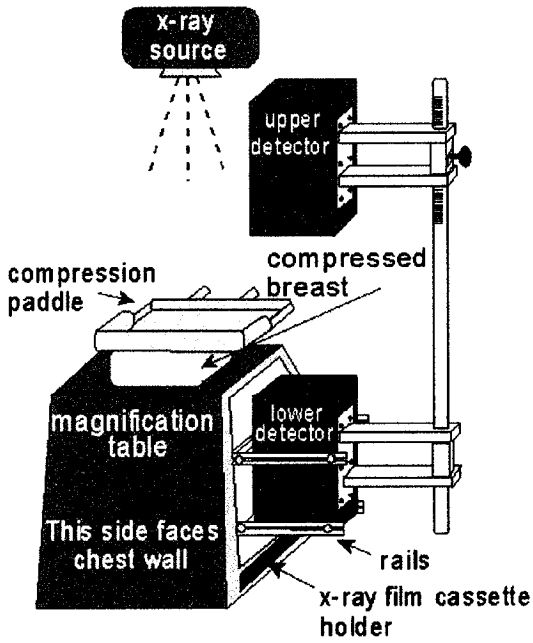

Fig. 2.6. This is the outline of PEM-I detector, which is co-registered with X-ray mammogram system.

Fig. 2.7 and Fig. 2.8 show the detector data acquisition schemes for X-ray mammogram and PEM imaging, respectively. With the system setup for mammogram imaging, the PEM detectors are located outside the X-ray field-of-view (Fig. 2.7). During acquisition for the emission image, the PEM detectors are positioned over the compressed breast (Fig. 2.8). A co-registration tool in the form of a steel wire frame, which is visible in the mammogram image, is attached to the upper detector. The frame area is equal to the useful field-of-view of the PEM scanner after projection via the X-ray magnification to the mid-depth of the compressed breast. The sides of the rectangular frame have regularly spaced marks that are used for scaling the emission images to match the mammogram images. The system arrangements ensure the acquisition of mammogram and FDG PEM images easily positioning and facilitate accurate co-registration images from two modalities [104].

The PEM-I system's spatial resolution is 2.8 mm (FWHM). A tumor uptake ratio of 6:1 (tumor-to-background ratio) is required to produce images with visually identifiable uptake [103][105].

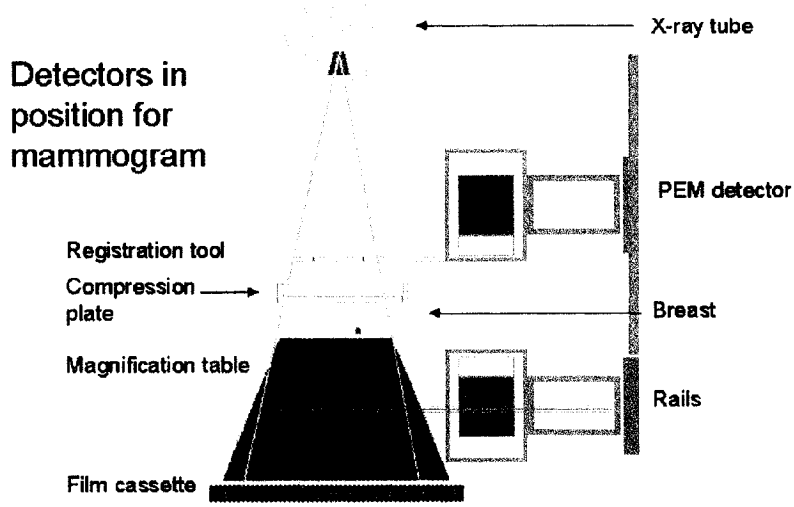

Fig. 2.7. The system is in mammogram position.

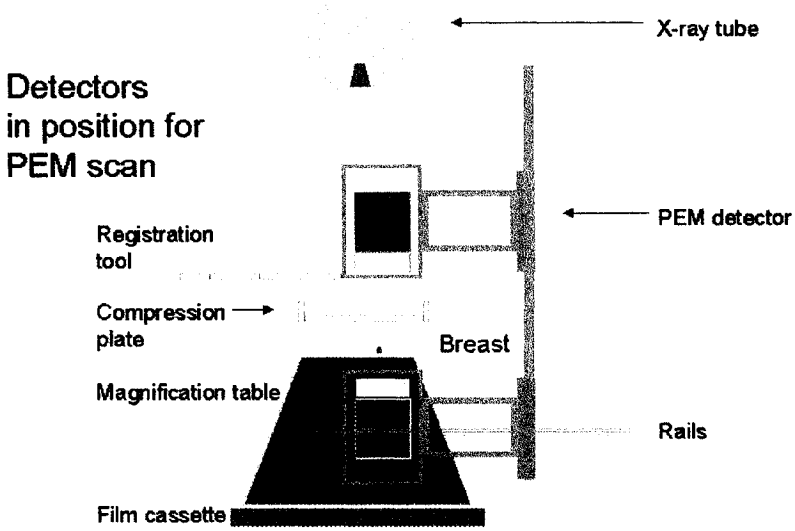

Fig. 2.8. The system is in PEM scan position.

ANIPET System outline

The ANIPET system has two emission imaging modes: longitudinal (2D-axial) and rotational (3D-rotary) [23]. The longitudinal mode produces multiple focal-plane images by back-projecting an inverse probability weighted value into the intersection of each plane with the line-of-response joining the coincidence crystals [23][73]. This technique is also used for breast cancer mammography (PEM-I). In this mode, a whole body scan

can be performed by moving the subject bed up to 256 mm through a detector 65 mm field-of-view (FOV). This produces a reconstructed image with a 256 mm × 65 mm FOV.

The rotational mode allows the detector pair to rotate around a point that is not necessarily the center line of the detectors. While the detectors rotate around the center line, the FOV is 65 mm. However, the detector can offset from the axis of rotation up to 25 mm, this setup increases the radial FOV to 90 mm.

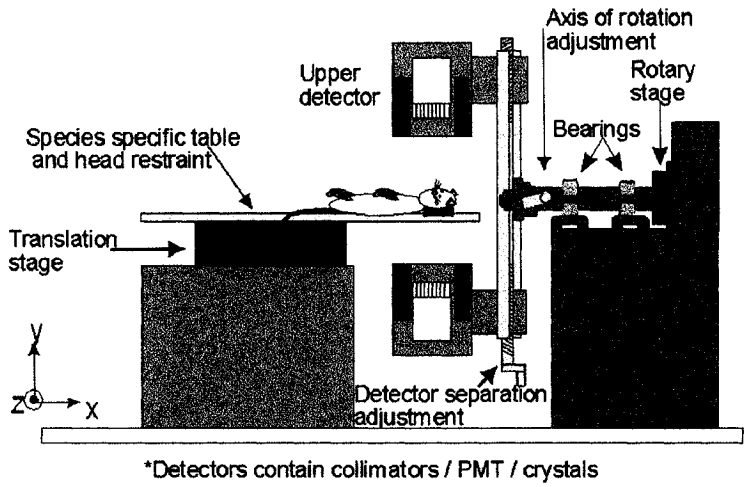

Fig. 2.9. The side view of ANIPET system.

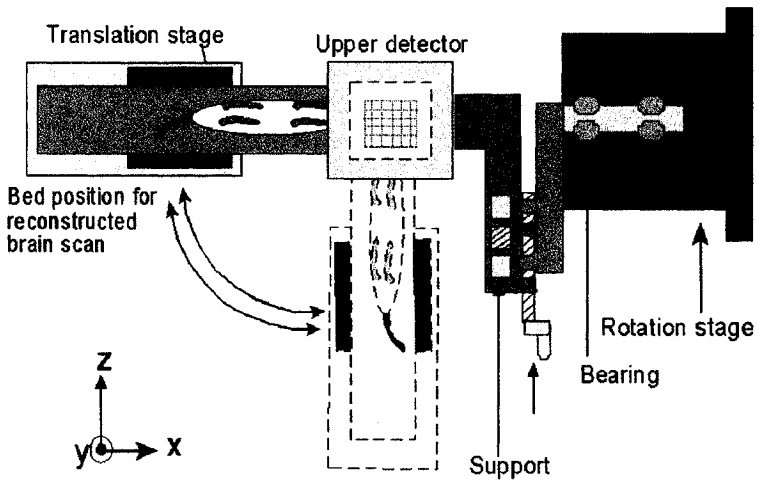

Fig. 2.10. The plan view of ANIPET system.

The side and plan view of the ANIPET scanner are illustrated in Fig. 2.9 and Fig. 2.10 [102]. The scanner bed can enter the detector either from the front or the side. This

facilitates either longitudinal or rotational scans to be performed. The bed is mounted on a translation stage. The detectors rotate on a 25 mm diameter stainless-steel shaft which is driven by the rotary stage. Table 2.2 gives the ANIPET system specifications [73].

TABLE 2.2. DETECTOR BLOCK SPECIFICATION OF ANIPET SYSTEM

	2D mode	3D mode
Detector separation (mm)	75-200	75-200
Efficiency[#]	0.8-0.1 %	0.8-0.1 %
Timing resolution (ns)	10	10
Axial FOV (mm)	256	54
Trans-Axial FOV (mm)	54	59-84
Spatial resolution (mm)	2.8	3.2

[#]The lower energy threshold is 250 keV in the efficiency measurement.

2.3 Some Dedicated Detector Designs for Small Animal and Metabolic Breast Imaging

Even though PET cannot approach the fine resolution (about 100μm) attainable with autoradiography, spatial resolution of 1-2 mm is still much more preferable in biodistribution studies, organ function studies, and tumor studies [32]. Two types of PMTs, positron-sensitive PMT (PS-PMT) and multi-channel PMT (MC-PMT), have been extensively used in the high-resolution dedicated PET systems for small animal and metabolic breast imaging.

2.3.1 Applications of Multi-Channel Photomultiplier Tubes

MicroPET system, which was developed by Dr. S. R. Cherry et al. in the University of California, Los Angeles (UCLA) for small animal imaging, is the first PET system to use a Lutetium Oxyorthosilicate (LSO) scintillator [32][64]-[66]. Between the LSO crystal and MC-PMTs in the MicroPET detector, fiber-optic coupling is employed to read out small crystal elements in order to minimize detector dead space. The system has a 1.6 mm

cubic resolution [4]; the field-of-view is 11 cm transaxial and 1.8 cm axial. The detector is in a ring of 17.1 cm diameter; the animal port diameter is 16 cm.

The MicroPET system consists thirty LSO blocks. Each block has an 8 × 8 array of discrete 2 mm × 2 mm × 10 mm elements. The crystal elements are polished on all sides, except on the front surfaces, which have a finely ground treatment. This combination has been demonstrated to yield the highest light output [67]-[71]. Each element is individually wrapped with PTFE (Teflon) tape. The block is then glued to 24 cm long, 2 mm diameter, double clad optical fibers. The opposite ends of fibers are glued into a MC-PMT XP1722. XP1722 (from Photonis, former Philips Components) [31] is a 64 channel (8 × 8 grid), 3 inch diameter PMT [70][72], which has a 4.5 mm thick fiber-optic entrance window helping to prevent spreading of the optical light.

The detector scheme has the feature of effectively one-to-one coupling between discrete crystal element and MC-PMT pixel (single channel), so the scintillation position is determined by PMT channel rather than by scintillation light sharing. Applying optical fiber coupling method can overcome peripheral dead space in the MC-PMT, so the crystal blocks can be formed tightly with no gaps. The main drawback of this design (scintillator - optical fiber – PMT) is the substantial light loss from the scintillation crystal to the PMT entrance window [64].

2.3.2 Applications of Position-Sensitive Photomultiplier Tubes

Position-sensitive PMTs (PS-PMTs) have been prevalently used in small animal PET and PEM systems. Different PS-PMTs models have been tested and employed in many research groups. For example:

- **R3941-05**, by Dr. C. J. Thompson [22][23][29][73]-[79] of McGill University, Dr. Yamashita of Hamamatsu Photonics K. K. [80], and Dr. J. Seidel and Dr. J. J. Vaquero of the National Institutes of Health (NIH) [82].
- **R5600**, by Dr. Watanabe of Hamamatsu Photonics K. K.[83].
- **R5900-C8** or **R5900U-C8** (U version has insulation cover outside the PMT metal envelope), by Dr. C. J. Thompson, Dr. S. R. Cherry [84], Dr. J. Seidel and Dr. J. J. Vaquero [85]-[87].

- **R7600-00-C12**, by Dr. C. J. Thompson [30], Dr. Nagai of Hamamatsu Photonics K. K. [89].

In addition, many different scintillation crystals, such as BGO, GSO, and LSO, have been used in the PS-PMT detectors. Again, block detector design is the main crystal scheme in these proposes. Many research groups have investigated the discrete crystal schemes (Dr. Yamashita, Dr. S. R. Cherry, Dr. J. Seidel, etc.) or pseudo-discrete patterns (Dr. C. J. Thompson, Dr. S. R. Cherry, etc.) in their PS-PMT detectors. The latest results presented the spatial resolutions of less than 2-mm in prototype PET systems. These results have demonstrated that the combination of PS-PMTs with block scintillation crystals is a promising detector configuration for dedicated PET systems for small animals and metabolic breast imaging.

2.3.3 Multi-layer Phoswich Configuration

Dedicated PET systems for small animal and breast imaging have smaller diameter of scanner ring. The DOI information from scintillation crystals become more important in order to achieve higher spatial resolution and resolution uniformity [85]-[98].

Recently Dr. J. Seidel et al. from NIH presented a design of three-layer phoswich detector scheme. Fig. 2.11 demonstrates their phoswich detector module [85]. The detector is in a 9 × 9 array. The dimension of each LSO (entrance layer), GSO (middle layer), and BGO (exit layer) element is same of 2 mm × 2 mm × 4 mm. All the elements are mirror polished to specular-reflective on all sides, except the entrance ends of the LSO crystals which are ground polished to diffuse-reflective. Each LSO/GSO/BGO phoswich element is assembled individually by permanently gluing together. The phoswich element is wrapped with Teflon tape and packed together to form the detector array.

Three levels of DOI information are obtained by delayed-charge-integration (DCI) method. This is based on the phenomenon of the three phoswich scintillators having different light decay times (LSO = 40 ns, GSO = 60 ns, BGO = 300 ns). Fig 2.12 draws the DCI processing diagram. As can be seen, the pulse of the last dynode is split into two routes. One is the current pulse which is integrated 600 ns just after the pulse arrives.

Since the pulse peaks of three phoswich scintillators all fall in this integrating region, this integrating process is also called full-charge-integration. In the another route, the last dynode output is delayed 130 ns firstly, then the pulse is integrated 600 ns. The delay time is manipulated in such a way that only the tails of the dynode pulses are integrated. This process is the case of DCI. By looking up the ratio of full to delayed integration outputs, the layer of interaction information can be obtained.

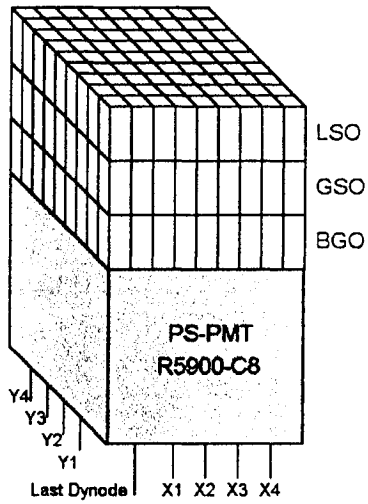

Fig. 2.11. This illustrates the module assembly of phoswich detector design.

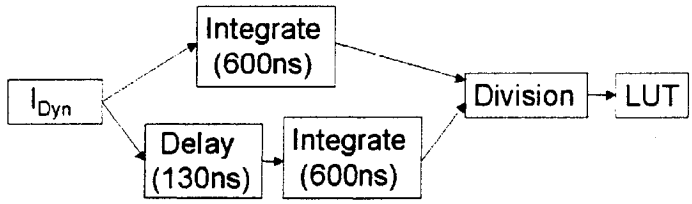

Fig. 2.12. This is diagram of DCI process. I_{Dyn} is the current output from the last dynode of the PS-PMT. LUT is division look-up-table.

2.3.4 Application of Avalanche Photodiodes

The first dedicated PET system for dynamic imaging of small laboratory animals based on avalanche photodiodes (APD) was designed and constructed by Dr. R. Lecomte et al. in the University of Sherbrooke, Sherbrooke, Quebec Canada [106]-[122]. The specification of the Sherbrooke APD PET scanner is listed in Table 2.3. The system uses small discrete scintillation detectors based on APD to achieve uniform, isotropic, and 14 μl volumetric spatial resolution with high image signal-to-noise ratio.

TABLE 2.3. PHYSICAL DESCRIPTION OF THE SHERBROOKE ANIMAL TOMOGRAPHY

Detector type	EG&G model C30994
Number of detectors	512 (256/ring)
BGO crystal size	3 mm × 5 mm × 20 mm (beveled)
Module dimension	3.8 mm × 13.2 mm × 33 mm
BGO crystal spacing	3.8 mm in-plane, 5.5 mm axially
Detector rings	2 (1 layer of modules)
Ring diameter	310 mm
Port diameter	135 mm
Useful field-of-view	118 mm
Axial field-of-view	10.5 mm
Reconstruction planes	3 (2 direct, 1 cross)
Plane interval	2.75 mm
Sampling	Calm-shell, 2 positions
Number of line-of-response	98,304 (total) / 65,536 (useful)

From (1.7), the "block effect" is zero if the coupling ratio between gamma ray detectors and their readout is 1:1. The Sherbrooke PET system uses small discrete detectors with individual readout and parallel signal processing to achieve high spatial resolution. The data acquisition system features list-mode data storage and real-time image reconstruction [120][121]. As time marks, physiological data (cardiac and respiratory gating) and other information (such as bed position, detector sampling location) are inserted into the list-mode data, images can be sorted out into static, dynamic or gated frames. Recently, Dr. Lecomte reported on cardiac studies of blood flow, metabolism and function in normal and infracted rats using the Sherbrooke APD PET scanner [122]. This presented the use of PET as an effective *in vivo* imaging tool for the investigation of cardiac physiology and metabolism in small animal models.

CHAPTER III

IMPROVING THE PERFORMANCE OF SMALL PLANAR DETECTORS OF PEM-I AND ANIPET SYSTEM

Dedicated PET instruments for small animal (ANIPET) and breast imaging (PEM-I) were previously developed in our laboratory. PS-PMTs and pixelated crystals with depth encoding scheme were used to detect and localize gamma rays. Large faceplate PS-PMTs, like R3941 which was employed in ANIPET and PET-I, show more distortion and have difficulty identifying crystal elements near their periphery. We have recently enhanced the BGO detector modules used in the PEM-I and ANIPET systems by modifying the crossed anode read-out resistor chain, modifying a faster timing amplifier circuit which takes the last dynode signal as event timing, and adding a new image weighting function to improve the crystal identification. The PMTs field of view increased from 46 mm × 58 mm to 56 mm × 64 mm and the timing resolution of system improved from 12.0 ns to 8.7 ns.

3.1 The PS-PMT Edge Effect Reduction

3.1.1 The Field-of-View of Detectors

The Hamamatsu R3941 PS-PMTs are employed in PEM and ANIPET detectors. This PS-PMT is a crossed-wire anode type with 18 wires in the X-axis and 16 wires in the Y-axis [100]. The wires are connected in an Anger resistor chain readout type [21] which provide X^-, X^+, Y^-, Y^+ positioning signals. The standard resistor chain in this PS-PMT has 1 KΩ resistors between each anode wire. This provides a linear readout of the charge deposition in the central portion of the PS-PMT. However, for events near the periphery of the PS-PMT, the charge spread can extend past the last anode wire. This truncation of the charge distribution causes the position readout to be non-linear near the edges of the

PS-PMT. In previous research by R. Clancy et al. [75], two resistors from each end of the X-axis resistor chain (R1 & R17) and two from the Y-axis resistor chain (R1 & R15) were changed to 15KΩ. The usable field-of-view increased from 40 mm × 48 mm to 46 mm × 58 mm. These changes improved the field-of-view significantly. But we found that the corners of the image were rounded and blurred. Recently we re-evaluated the electronic circuits based on this resistor chain design, and reconsidered the tradeoff of the readout linearity, sensitivity in the PS-PMT field-of-view with the charge loss compensation on the periphery.

3.1.2 The Edge Effect Reduction Re-evaluation

The gain (current amplification) of the PS-PMT is not uniform over its field of view [100]. The gain drop at the periphery is significant, and is due to electron loss at the edge of each dynode because the electrons gradually spread through the cascade multiplication [7]. Several researches have been proposed to reduce the edge effect and to make the sensitive area of the PS-PMT as large as possible [75][80].

Fig. 3.1 displays the schematic of Hamamatsu R3941 PS-PMT crossed anode resistor chain with N anode wires interconnected by resistors where N is 18 for X-axis and 16 for Y-axis.

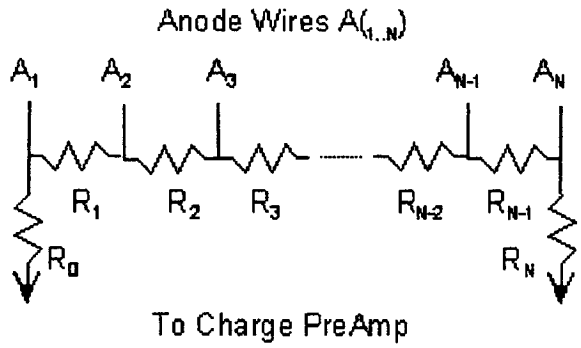

Fig. 3.1. The schematic of crossed anode wire PS-PMT read-out resistor chain.

A simple technique to increase the field-of-view in PS-PMT was developed by R. Clancy et al. [75]. Increasing the end resistors R_1 & R_{17} in X-axis and R_1 & R_{15} in Y-axis

from 1KΩ to 15KΩ, additional crystal rows and columns of proximal crystal elements were identified - overall there were 29 rows crystal elements in the X-axis and 23 columns in the Y-axis.

The studies by R. Clancy which lead to the change in resistor value from 1KΩ to 15KΩ were based on single crystal readout and moving the crystal along the edges. As the value was increased, the effect of the lost charge decreased, and the range of linear readout extended. However the image from a full crystal array has rounded corners - we could see this artifact from previous 2-D crystal identification image as the corners were rounded and overlapped. So the events could not be positioned in those regions. We re-evaluated these peripheral resistors in X-axis and Y-axis resistor chain by choosing different resistor value with 10 KΩ resistors instead.

Fig. 3.2 is the crystal identification "fish-net" array representing the boundary assignments for the both near and far elements. This is from one of the PEM detector (PS-PMT serial #: AA0366). By re-evaluating the end resistors in crossed-wire anode read-out chain for both X-axis and Y-axis, the corner linearity was improved and position sensitivity increased as well. About 28 by 32 crystal elements can be identified. So the detector field-of-view has been improved from 46 mm × 58 mm to 56 mm × 64 mm.

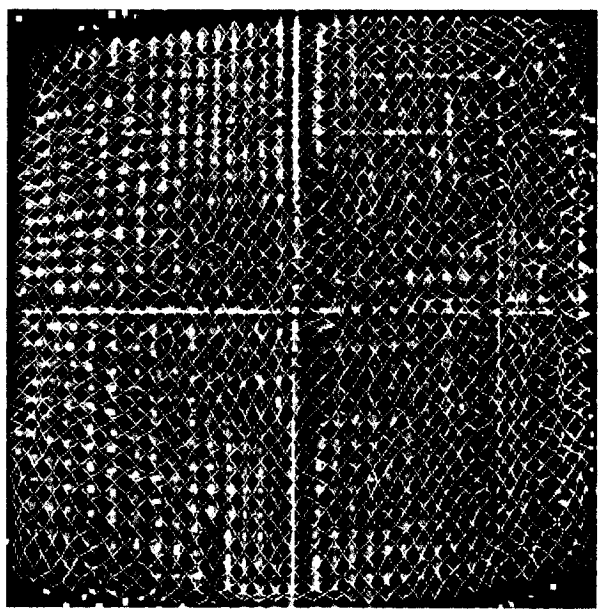

Fig. 3.2. Crystal identification map after modification of PS-PMT resistor chain. 32 rows in the X-axis and 28 columns in the Y-axis can be identified.

3.2 Fast Timing Amplifier Circuit Development

3.2.1 Detector Timing

The timing trigger of detectors could be acquired by discriminating the energy signals from the sum of anode output X^-, X^+, Y^-, Y^+ signals. If the anode outputs were used for timing, four fast preamplifier buffers and a fast summing circuit would be needed. But the trigger can also be acquired from the PS-PMT last dynode output because the last dynode gives a signal for all events, and the signals from last dynode are also synchronous with anode outputs [8]. A high gain, high speed timing amplifier circuit which evolved from a Hamamatsu original design has been installed and tested. This circuit performs the timing trigger from the output of PS-PMT last dynode by using wideband, fast setting current feedback amplifiers.

3.2.2 Developing a Fast Timing Amplifier Circuit to Improve System Timing Resolution

The event timing trigger is obtained from last dynode output by modifying the PS-PMT high voltage (HV) divider circuit. The main problem of this design is to obtain the required signal without disturbing the anode output signals. The pulses taken from a dynode are positive going which is different from anode output polarity [8].

A new Hamamatsu dynode timing amplifier circuit has been built and tested as shown in Fig. 3.3. The coupling capacitor Cc connects the output of last dynode and timing amplifier circuit. Because the last dynode is at a voltage potential of about 70 volt (negative), the Cc requires a higher voltage rating. This capacitor also should be big enough, otherwise the pulses of last dynode output would be differentiated.

A single ground point for coax cable must be used to minimize the inductive effects. The shield of coax cable is connected to HV divider ground [8] as shown in Fig. 3.3.

This timing amplifier circuit board is located in the detector housing. The total gain of the amplifier is over 600, which provides an output signal high enough to feed the constant fraction discriminator directly. A current feedback topology amplifier [81] is used. The two inputs for these kinds of amplifier are dissimilar and the current noise of

the inverting input is much larger than that of the non-inverting. Fig. 3.3 shows that the first stage of last dynode amplifier circuit is chosen non-inverting gain circuit. In this configuration, the amplifier is sensitive to stray capacitance to ground at the inverting input, so the inverting pin connections is kept small with minimal coupling to the ground in printed circuit board layout. Two to 5 pf trim feedback capacitors are also used to compensate PMT dynode output capacitance and parasitic capacitance. For ANIPET, this is more critical as the circuit should avoid picking up the noise created by the stepping motors that move the detectors and bed.

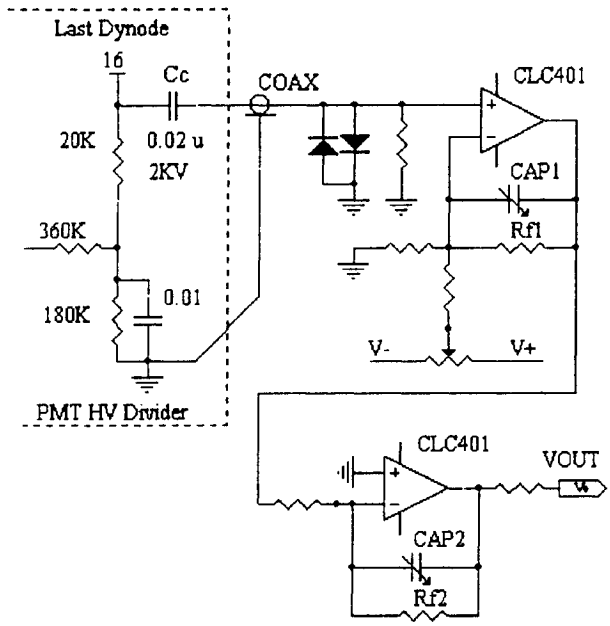

Fig. 3.3. The schematic of last dynode amplifier circuit

Timing resolution of the PEM and ANIPET system was measured by general fast-slow coincidence technique. The timing signal of one detector inputs to a Time-to-Amplitude Converter (TAC) module (CANBERRA Time Analyzer, model 1443A) directly, another timing from the opposite detector inputs to TAC through a Delay Box Module (CANBERRA Nsec Delay, Model 2058). The amplitude output from TAC which was proportional to the input timing difference was measured by a Multichannel Analyzer (Tracor Northern, model TN-1705).

Fig. 3.4 is the measured PEM system timing resolution. By applying the new timing amplifier circuit, the system timing resolution improved from 12.0 ns to 8.7 ns.

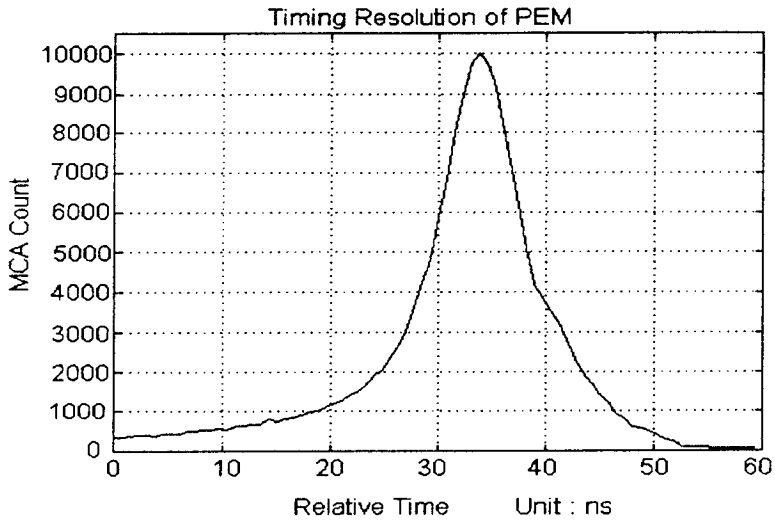

Fig. 3.4. PEM system timing resolution. FWHM is 8.7 ns.

3.3 Implement Weighting Factors to Improve Crystal Identification

3.3.1 Crystal Elements Identification

The crystal blocks in PEM and ANIPET detectors have been pixelated on two opposite faces to provide depth of interaction information. To generate spatial distortion look-up-table, a 5μCi ^{68}Ge rod source is used to irradiate only the proximal crystal elements (coupled to the PS-PMT windows directly) from the side of the detector. In order to acquire sufficient data to produce the two-dimension crystal identification image, both sides of the crystals are irradiated. Previously a graphical software was developed in MATLAB for crystal identification written by J. Robar et al. [78][105].

The crystal elements are much more clearly visible in the region close to the source in the side irradiation image. This is due to the effect of the attenuation of the gamma rays from the side of the block towards the center. Instead of merely adding the images from both side irradiation, we expected that a weighting factor could be applied such that regions where the crystal identification was good were highly weighted while the regions where adjacent crystal elements could not be easily separated were less weighted. We have added a new feature in the software which weights the images to improve the crystal elements identification.

3.3.2 Implementation of Weighting Factors

Data for the spatial distortion identification is collected by acquiring single events using a slit collimated ^{68}Ge rod source to side-irradiate the proximal crystal elements as illustrated in Fig. 3.5. In order to identify all crystals, two separate side-irradiation are done from opposite sides.

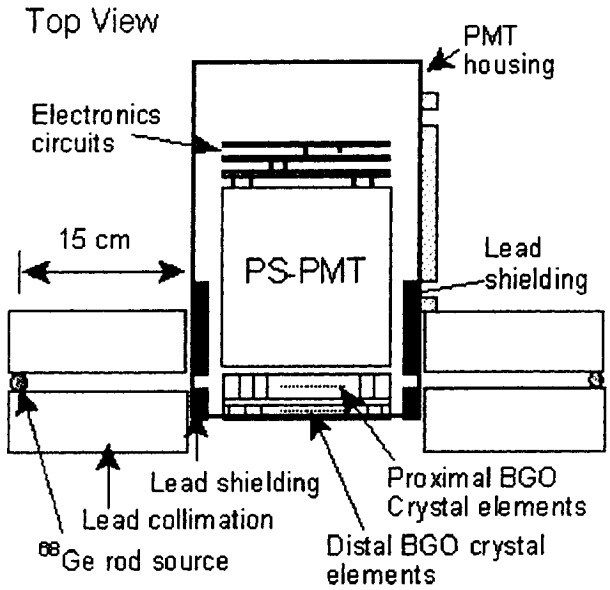

Fig. 3.5. The ^{68}Ge rod source is aligned to irradiate only the proximal elements of the BGO crystal blocks.

In PEM and ANIPET data acquisition system, the data of $\Delta X = (X^+ - X^-)$, $\Delta Y = (Y^+ - Y^-)$ and $E = (X^+ + X^- + Y^+ + Y^-)$ are digitized by Jorway Aurora Model 14 six channel ADC [129] and eight bits are saved in list files. The positioning (X,Y) is done in software by calculating $X = \Delta X/E$ and $Y = \Delta Y/E$. The two-dimension histogram of (X,Y) image are formed for energy windows of 32 - 63, 64 - 95 ... 224 - 255 from each of the two source positions.

All fourteen energy windowed images corresponding to the different energy range will be read. Generally, the images corresponding to the lower-energy windows do not shown separated crystal elements, while those in the mid-range windows will contain the images in which adjacent crystal elements can be separated. Images for the highest energy-windows may contain useful data also, but often contain few counts. The software allows the user to select image which show the best crystal identification. One can select one

energy-windowed image several times to increase the weighting of this image. The histogram image for crystal identification is the summed result of selected images.

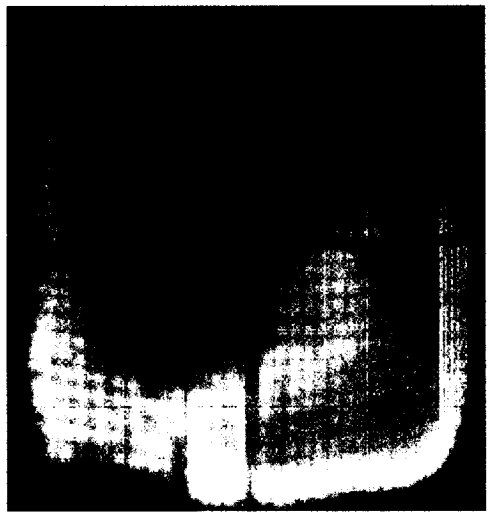

Fig. 3.6. This is the one of side-irradiation image. The energy window is from 128 to 160 and the source is at the bottom of the image.

The image of Fig. 3.6 is the image that has energy window from 128 to 160. From this image, we can find only a certain area of this image is useful for crystal element identification.

A weighting function has been developed to filter each selected windowed energy image. For each selected image which has certain energy window, we first set a weighting mark point IP(O_X,O_Y) by moving and clicking the mouse in the image range. This is illustrated in Fig. 3.7. This IP mark should be selected around the image area in which adjacent crystal elements can be separated clearly. According to the mark O_X, O_Y coordinates we establish weighting factor image WgtFac(X,Y) as following:

$$\begin{aligned} WgtFac(X,Y) = (((X-128)/128)\times X_{scale}+1) \\ \times(((Y-128)/128)\times Y_{scale}+1) \end{aligned} \tag{1}$$

where X_{scale} and Y_{scale} are defined as:

$$\begin{aligned} X_{scale} &= (Ox-128)/128 \\ Y_{scale} &= (Oy-128)/128 \end{aligned} \tag{2}$$

The weighting factor WgtFac(X,Y) is used as a filter. We can get the weighted image Wgtimg(X,Y) from the original image Orgimg(X,Y) as:

$$Wgtimg(X,Y) = Orgimg(X,Y)\times WgtFac(X,Y) \tag{3}$$

We then sum all selected images which pass the weighting process to get the final two dimension histogram image.

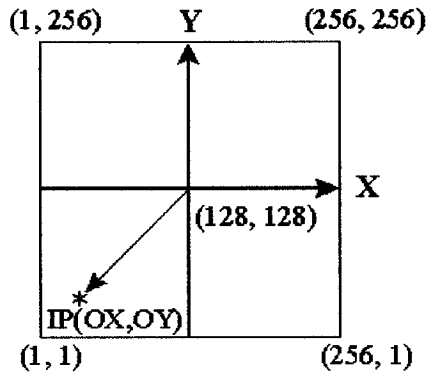

Fig. 3.7. Weighting factor selection: IP is the mouse selected point -IP(15,16) in an energy windowed image.

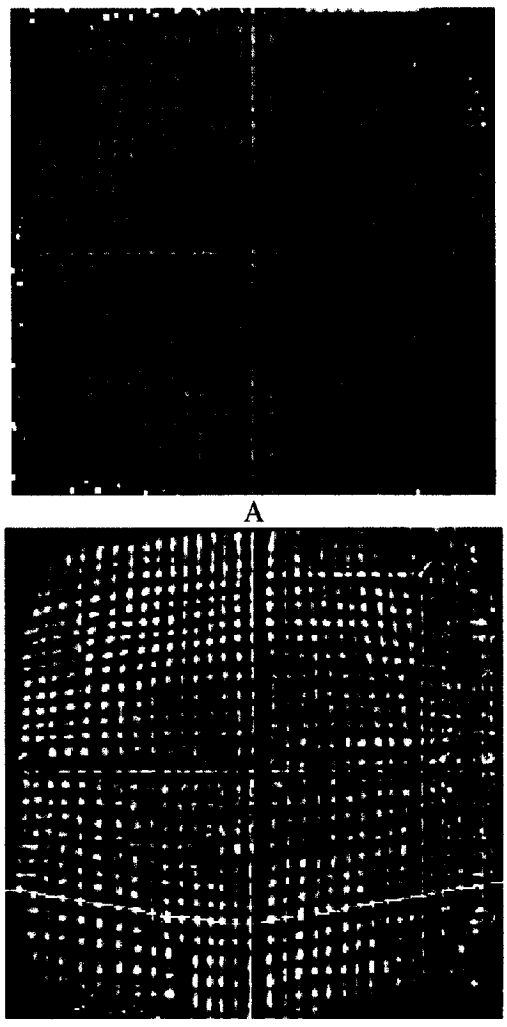

A

B

Fig. 3.8. Crystal identification image before (A) and after (B) applying weighting function to the original energy windowed image.

Fig. 3.8 is the crystal identification image after applying weighting image function. We can see the adjacent elements are separated very well. Fig. 3.9 and 3.10 are the profiles of the original and the weighted images from the same corresponding position.

Compare these profiles, we can see the peak-to-valley ratio are improved significantly. The overall peak-to-valley ratio improved by 88 %.

This Weighting Image function has been applied to improve the crystal identification for generating spatial distortion look-up-table.

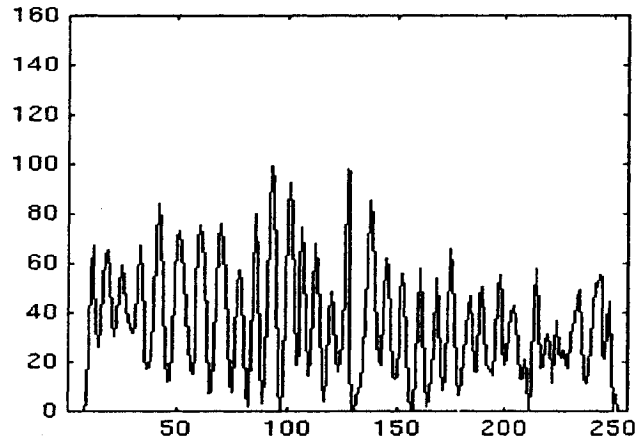

Fig. 3.9. The profile of original image.

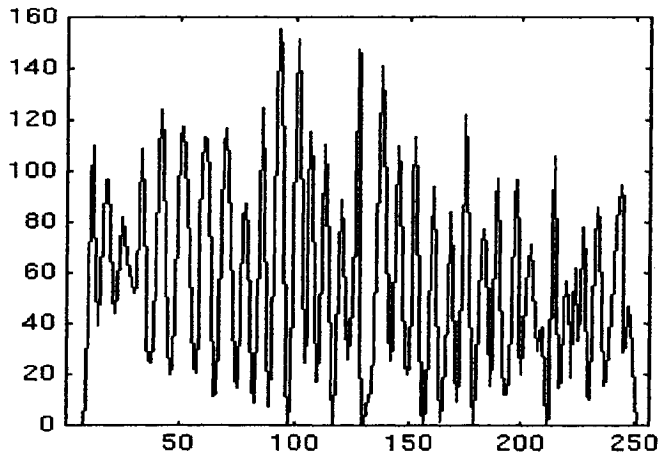

Fig. 3.10. The profile of weighted image. Compared with Fig. 3.9, the weighting affects significantly on the right region of the image.

3.4 Generating the Energy and Efficiency Look-Up-Table

The energy and efficiency tables are generated during a single reading of the flood irradiation file. The ^{68}Ge rod source is positioned at a distance of 40 cm from the detector

face in order to approximate a flood source. The single events are acquired and stored in a list file. This list file is processed with reference to the previously generated spatial distortion look-up-tables. For each event contained in the list file, the (X, Y) coordinates are used as indices to look up the distortion tables and returned corresponding crystal coordinates (Cx, Cy).

The energy of an event is the amplitude of the signal determined by summing the X^-, X^+, Y^-, Y^+ signals. The energy E of this event is read from the list file with (X, Y) coordinates. After checking the distortion look-up-table, the element of a 72 × 72 × 256 matrix specified by the indices [Cx][Cy][E] is incremented. By repeating this procedure for each of the events in the list file, an energy spectrum for each of the identified crystal elements is compiled.

The spectra of individual identified crystal elements is displayed in Fig. 3.11. The key point is how to locate the photo peaks and then setup the energy low, high thresholds to format the energy identification windows. By smoothing each energy histograms, computing the slope of spectrum segments, the photo peaks are identified more accurately without incorrectly assigning the peak of the resulting from the noise. The peak locations in Fig. 3.11 are from the automatic software identification. As there are about 896 crystal elements can be identified in one detector; the automated software gives an efficient and precise way to find the position of photopeaks.

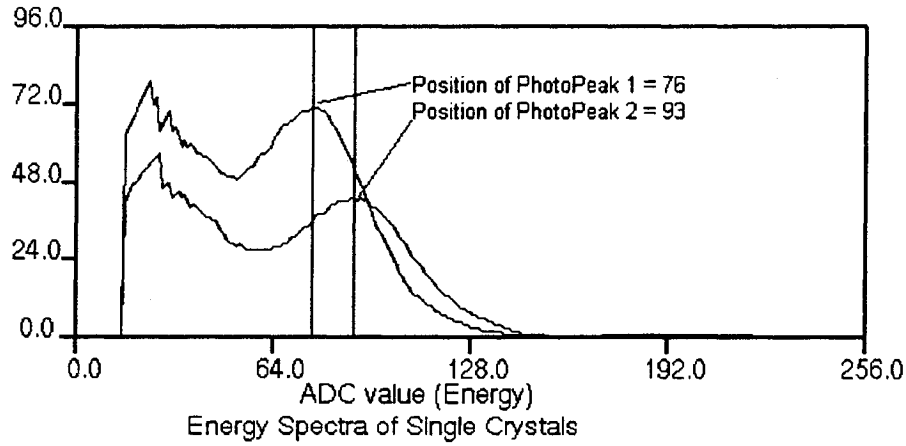

Fig. 3.11. This is the display of detector element spectrum. The positions of the photopeak are come from software automatic locating results.

The content of energy look-up-tables and efficiency tables are represented in Fig. 3.12 for ANIPET detectors. Each shaded square in energy and efficiency tables represents an identified crystal element according spatial distortion maps. The intensity of energy tables indicates the location of the energy spectrum photopeak for every crystal element, which has a digitized value from 0 to 255. The intensity of efficiency tables indicates the crystal element's relative efficiency, which is assigned a valued from 0 to 255.

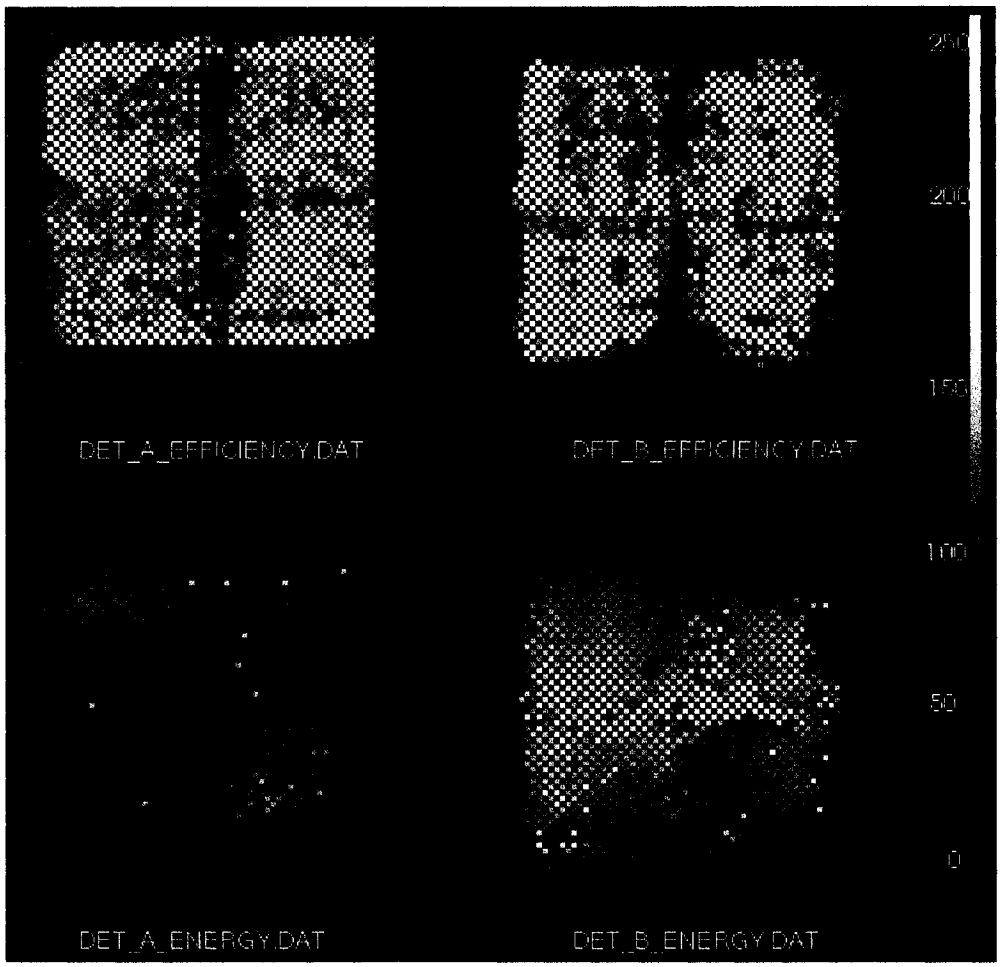

Fig. 3.12. This is the map of energy look-up-tables and efficiency tables for detector A and B of ANIPET.

Four crystal blocks coupled to a PS-PMT cover a 72 mm × 72 mm area, approximately corresponding to the dimensions of the PS-PMT outline window. The total area of efficiency look-up-table displays this area. However the anode wires span only about 55.5 mm in the X-direction and 63.6 mm in the Y-direction. After improving the performance of detectors, we can identify all the crystal elements in the area spanned by the anode wires. These images represent data acquired after the changes were made.

CHAPTER IV

CRYSTAL PROCESS IN PROTOTYPE PEM-II DETECTOR

Dedicated PET instruments for small animal (ANIPET system) and breast imaging (PEM-I) were previously developed in our lab of the Montreal Neurological Institute, McGill University [22][23][77]. Each system consists of two detectors; each detector is constructed with four 36 mm × 36 mm × 20 mm BGO crystal blocks optically coupled to a Hamamatsu R3941-05 PS-PMT [100]. Electronic circuits in these detectors consist of high voltage dividers, crossed anode read-out resistor chains, position preamplifiers, and fast timing amplifier circuits. The system spatial resolution is 2.8 mm; the timing resolution is 12 ns. The detector field-of-view is 64 mm × 56 mm [29].

Our clinical studies with PEM-I system revealed that the detectors have relatively large peripheral dead region. This is mainly caused by the PMT intrinsic structure. R3941 is a mesh type PS-PMT with a thick glass envelope. The PMT light-photon input window is in a photocathode head-on configuration. The cross-anode outputs have 18 anodes in the X-axis and 16 anodes in the Y-axis. Even though the outer dimension of the PMT is 78 mm × 78 mm, its effective input window, or the effective field-of-view, is only about 60 mm × 54 mm [100]. In the detectors of PEM-I and ANIPET, BGO crystals cover the PMT window in a region of 72 mm × 72 mm. After the previous efforts to develop and improve readout weighting matrix for the PMT, we identified crystal elements in the area of 64 mm × 56 mm [29][123]. However, there are still 7-mm periphery dead regions in each end of X-axis, 11-mm in each end of Y-axis. Since PMTs can only operate in a light tight environment, inevitably the detector enclosure further enlarges the dead region. In PEM studies, the overall peripheral non-sensitive area limits imaging near a patient's chest wall resulting in degrading diagnostic accuracy and efficiency.

One of the main challenges in PET instrumentation research and development is to achieve high spatial resolution, ideally in less than 2 mm. Even though PET cannot

approach the fine resolution attainable from anatomical diagnosis instruments, such as X-ray radiography, CT and MRI, spatial resolution of 1 to 2 mm is still desirable in organ function studies [32].

In order to enlarge detector field of view, achieve higher spatial resolution, and reduce the detector peripheral dead region, we developed prototype modular detectors for our proposed PEM-II scanner.

Crystal process for the prototype PEM-II detector is discussed in this chapter. The design and development of the front-end electronic circuits will be described in the following chapter.

4.1 Crystal Pixelating

We used Hamamatsu PS-PMT R7600-C12 [124] to build our new PEM-II detectors. R7600-C12 is a metal-channel type PMT fabricated with stacked thin electrodes. It has very narrow space between dynode stages and is constructed with a compact metal package instead of the traditional glass envelope. The PMT package has outer dimensions of 26 mm × 26 mm, and the effective window is 22 mm × 22 mm.

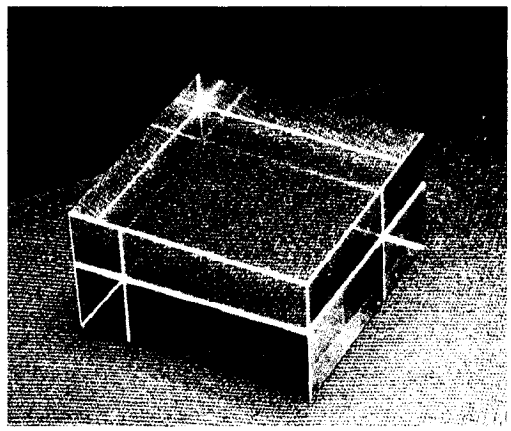

Fig. 4.1. This is one of the solid BGO crystals. All the crystal surfaces were mirror polished.

The dimensions of the solid BGO crystals we ordered [125] are 22 mm × 22 mm × 20 mm, since the effective area of the PS-PMT R7600-C12 is 22 mm × 22 mm. These crystals were finely mechanical polished on all the surfaces (Fig. 4.1). We further prepared the crystals by cutting, chemical polishing, and epoxy encapsulating.

In PET detectors, block crystal designs with discrete or pseudo-discrete schemes have been extensively investigated and used [54][126]. We investigated a pseudo-discrete design in our previous PEM-I and ANIPET [22][23][77]. The same BGO crystal pixelated scheme was used in the new PEM-II detectors.

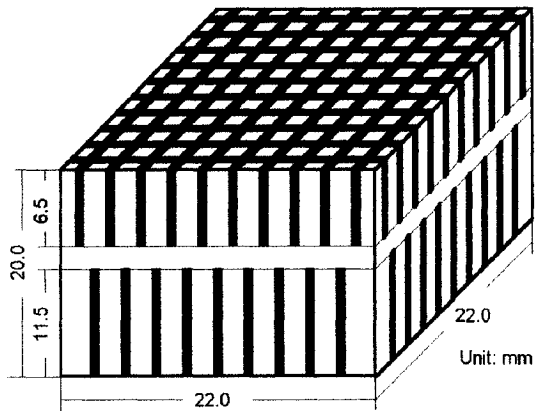

Fig. 4.2. This shows the structure and dimensions of BGO scintillation crystal for PEM-II detectors. The black regions in the graph demonstrate the saw-cut gaps.

As depicted in Fig. 4.2, the crystal blocks were pixelated by a diamond saw [127] into small elements of 2.1 mm × 2.1 mm (2.2-mm pitch) on two opposite faces. The elements on one face of the block offset by half the crystal pitch from those on the opposite face in both X and Y axes. The crystal elements with 11.5-mm depth are coupled to the PS-PMT window - we describe this layer as the "near the PMT-window layer" or the "near-layer". Those with 6.5-mm depth are on the opposite face, described as the "far-layer". These crystal depth scales are based on a Monte Carlo simulation result ensuring an equal probability of gamma ray interaction in each of two layers [22]. With this scheme, one bit depth-of-interaction information can be obtained by identifying the layer in which events occur.

Fig. 4.3 shows the diamond saw machine. Normally, three diamond blades (0.25-mm thickness) can be mounted on the shaft in a single cutting pass. The multiple blades were separated by 1.85-mm thick aluminum flanges. During the cutting operation, the blade rotation speed was adjusted to 1,000 RPM. Due to the hardness and fragility of the BGO characteristics, the feed speed was set to the machine's minimum value (about 0.05 mm/s). A specific coolant (containing a rust-inhibitor) steady streams over the crystal

surface. This prevents heat generation in the blades and the crystal - the heat expansion could break the crystal element. The coolant also washes away the BGO "saw dust".

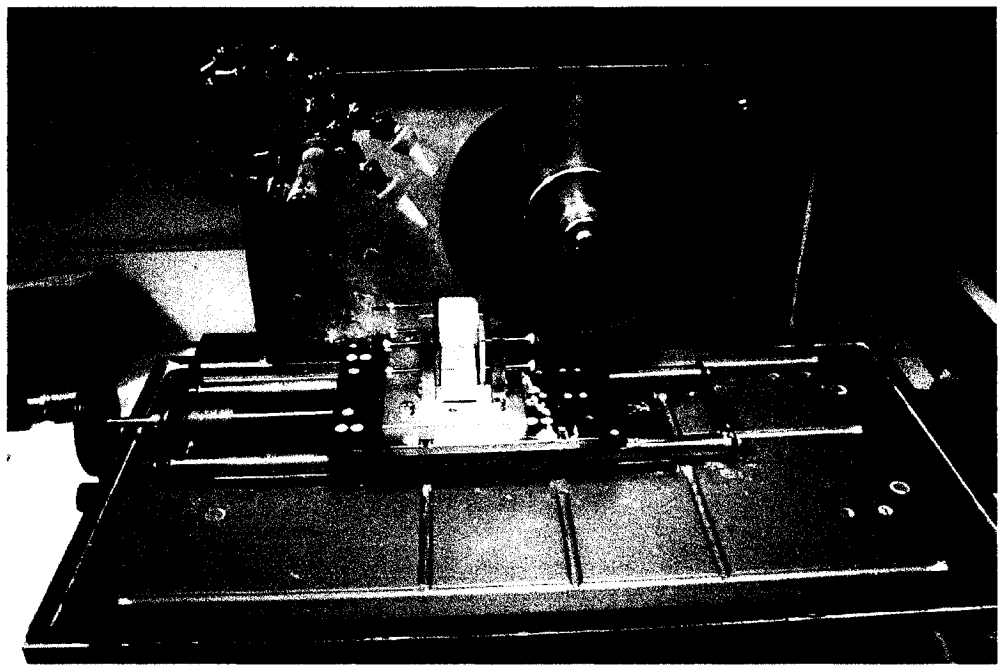

Fig. 4.3. This is the diamond saw used for cutting BGO crystals. A crystal was held in the vice below the motor shaft and the diamond blades.

4.2 Crystal Chemical Polishing

After we cut the crystals, the cut surfaces produced by diamond saw blades became very rough. This roughness would degrade the light collection [78]; therefore we need to polish the crystals. Since the cut crystals were extremely fragile, and the crystal elements are in the complex pattern, it is extremely difficult to polish the crystals mechanically. For that reason, chemical polish by acid etching was chosen to polish the surfaces of all the crystal elements.

The etching acid is a solution of 30% Hydrochloric (HCL) and 70% Nitric acid (HNO_3) [128]. The cut crystal was placed on a band of glass wool immersed into a 259 ml beaker containing the acid solution for 5 minutes (Fig. 4.4). Then the beaker was put in an ultrasound bath (ultrasonic cleaner) for another 2 minutes. Next, the crystal block was removed from acid and rinsed under a thin stream of water. Finally, it was rinsed again

with ethanol solution. By carefully following these steps, the risk of breaking the crystal elements off the block was sufficiently reduced.

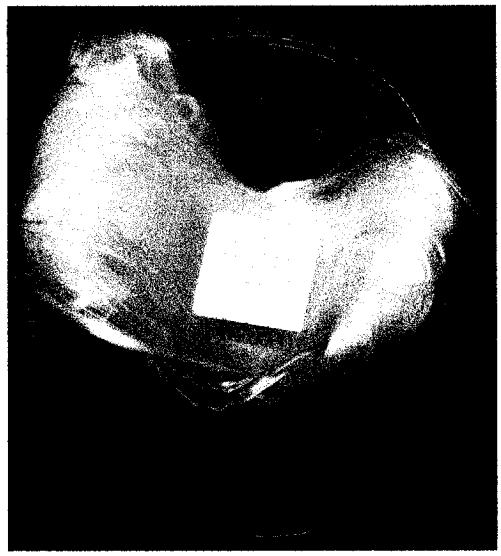

Fig. 4.4. A crystal block was sunk into the acid-etching bath held by cushion glass wool.

4.3 Crystal Epoxy Encapsulating

The acid etching makes the crystals even more fragile, any additional mechanical processing (painting, packing) would easily break the crystal elements, so we chose to encapsulate epoxy compound to coat crystal elements.

In PS-PMT detectors, maximum light output from each crystal element is preferred and no light sharing on the PMT window is required. The criteria for selecting epoxy compound are that it is both optically opaque and high reflective. Optical opaque compounds can isolate light transmitted to adjacent crystal element; high reflectivity will largely recover the light transmitted outside the event crystal volume. The reflectivity of the coating material is important because a significant fraction of the scintillation light may interact with this reflector before finally reaching PMT window [130].

The epoxy compound selected includes a two-component epoxy, and an epoxy base coloring paste. The epoxy product is "EPO-TEK 301-2" [131] containing base epoxy (part-A) and hardener (part-B) two components. Their mixed ratio is 100:35 parts by weight. This product has several superior characteristics, such as excellent adhesive ability, very low viscosity, very low shrinkage, and low outgassing. So in the curing procedure, minimal air bubbles could be generated and trapped inside epoxy resin, and

least shrinkage stress eliminates any possibility of cracking the very fragile crystal elements.

Since the mixed epoxy is transparent after curing, we colored the epoxy mixture with an epoxy-based white paste (REN DW-0131). The proportion of white paste to epoxy was 2:1 parts by weight. The mixed product was opaque, highly reflective, and still relatively low viscosity.

One original experiment record is shown in Appendix B.

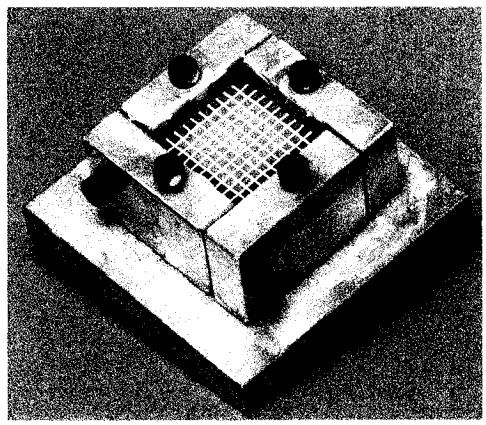

Fig. 4.5. The inner dimensions of the mode are 23.00 mm × 23.00 mm × 21.00 mm, with a tolerance of ±0.05 mm.

The low viscosity compound was chose to fill the crystal cutting gaps without trapping air bubbles, but the trade-off was that the compound could drain out of the gaps before curing. To solve this problem, an aluminum mold for confining the potting material was built with milling machine in of the Physics Department Workshop. Fig. 4.5 shows the mechanical drawing of the potting mold. The inner dimensions of the mold are 23.00 × 23.00 × 21.00 mm, with a tolerance of ±0.05 mm. The four molding walls were fixed to the aluminum plate, and secured each other with screws after the target crystal was positioned. All the molding walls were designed for easy assembly and removal. The inner walls and the top surface of the plate were all polished in order to facilitate the release of the cured crystal.

The release agent RP 79-2 [132] was chosen to facilitate the release of the cured crystal from an aluminum-encapsulating mold. It is an aerosol, semi-permanent, and Teflon based release agent formulated without wax or silicone, designed especially for epoxy

applications [133]. Sprayed RP 79-2 to the inner surfaces of mold, the epoxy curing resist is transferred from the mold to the encapsulating crystal block.

4.4 Optimizing the Crystal Process

4.4.1 Edge Crystals in the Far-Layers

After cutting, the solid crystal block had 10 × 10 elements in the near-layer, and (½ + 9 + ½) × (½ + 9 + ½) elements in the far-layer (Fig. 4.1). By evaluating crystal irradiation images, we found that the edge crystal elements in the far-layer were not visible. Images show that these edge elements were even blurring the edge near-layer elements and the inner far-layer elements as well. Hence, we decided to break off the entire far-layer edge crystal elements to reduce the image distortion. To avoid damaging the near-layer crystal elements, this procedure was done after encapsulating the near-layer. Fig. 4.6 shows a partially finished crystal. The near layer has been filled with reflector and the edge crystal elements have been removed from the far layer.

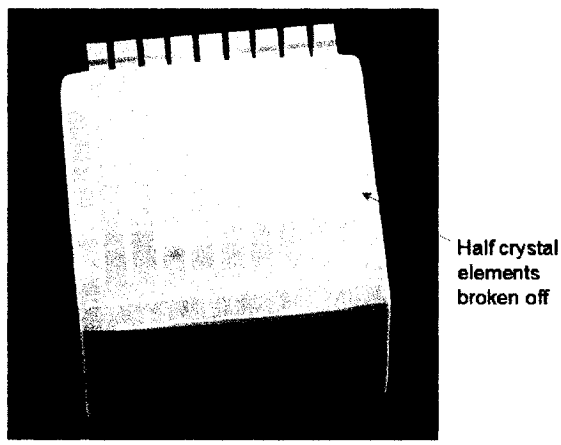

Fig. 4.6. After cutting and acid polishing, the near-layer of the crystal block was encapsulated with epoxy compound and surrounded by white Teflon tape. The half-crystal elements of the far-layer in the image were already removed.

4.4.2 The Uncut Region Between the Near and Far Layers

Fig. 4.7 shows an initial crystal identification image resulting from frontal irradiation with a ^{68}Ge source [136]. In this image, the near-layer elements can be clearly identified.

The far-layer elements can be accentuated by applying an energy-banding technique [136]. As shown in Fig. 4.7, there are near-far element overlaps in the images. These overlaps would cause difficulty in assessing the depth of interaction information.

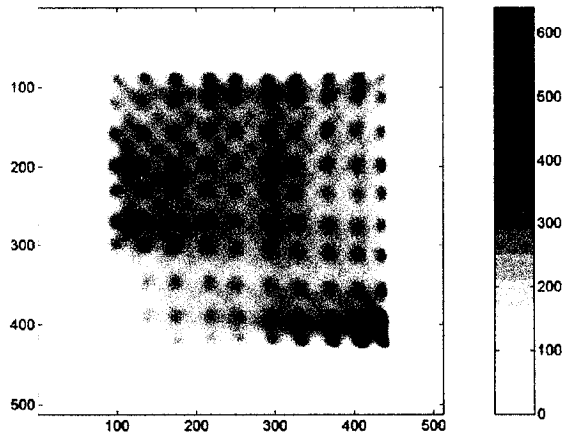

Fig. 4.7. This is a BGO crystal front-flood irradiation image with a ^{68}Ge source. The hardware lower energy threshold is 150 keV.

We subsequently investigated other methods to better identify crystal elements in both layers [136]. The most successful approach was to completely eliminate the 2-mm uncut region interconnecting the near and far layers. Our Monte-Carlo simulation also indicated that this uncut region could be a cause of the near-far image blurring [130][137].

We first cut the crystal along the uncut-region with a thick diamond saw blade (1-mm thickness). The diamond saw with the crystal in position is shown in Fig. 4.8. An aluminum mold was built with a milling machine to mount the crystal to the diamond saw table during the cutting procedure. Fig. 4.9 shows the separated two layer segments. Next, we mechanically removed the remnants of uncut regions on both segments. Then we mirror-polished the cut surfaces providing a specular-reflective finishing. Finally, the two segments were aligned and glued together by an optical coupling compound - a product of Sylgard-186 [125] containing two components of Silicone Elastomer (part A) and harder agent (part B). The mixed ratio is 10 parts elastomer to 1 part curing agent by weight. The index of refraction of Sylgard-186 is 1.465.

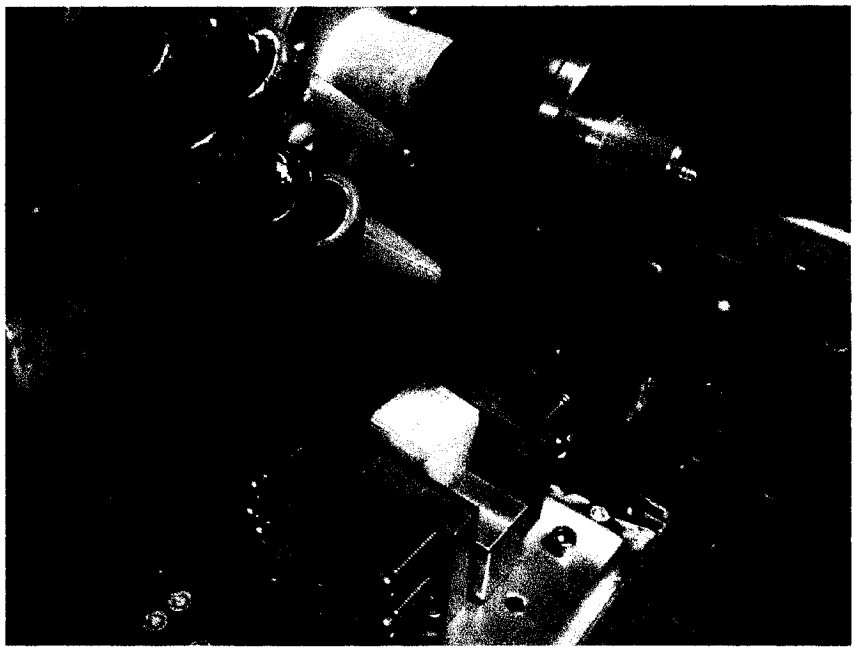

Fig. 4.8. A crystal was mounted in an aluminum mold ready for separating by a thick diamond saw blade.

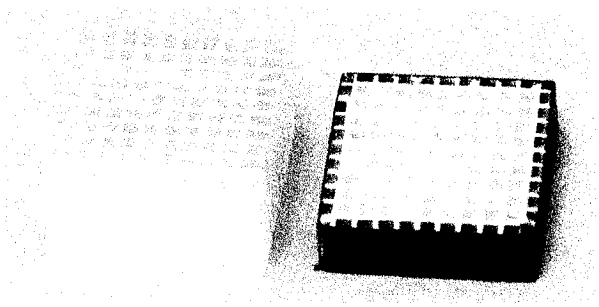

Fig. 4.9. The crystal of 22 mm × 22 mm × 20 mm was cut into two segments. The interconnecting uncut region was eliminated.

4.4.3 The Optimized Crystal Process Procedure

The optimized crystal processing procedures are illustrated in flowchart Fig. 4.10. Compared with the crystal operation procedures in PEM-I and ANIPET detectors, we added two major steps: cutting the crystal along the interconnecting uncut region and crystal segments polishing. Even though the pixelated and acid-etching crystals were very fragile, they became quite solid after encapsulating with adhesive epoxy-pigment mixture. It turns out that the process of cutting along the uncut region is much easier than pixelating the near and far layers.

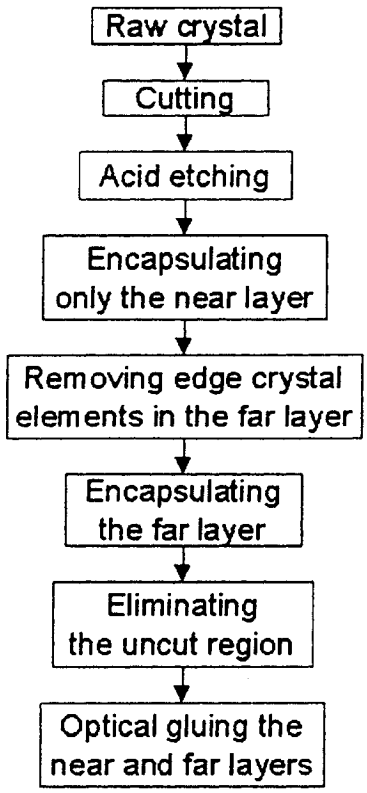

Fig. 4.10. This flow-chart illustration the optimized procedure in crystal processing.

4.5 Discussion on Encapsulating Epoxy Materials

"Block detector" design [43][44] with either discrete or pseudo-discrete block schemes has been frequently employed in PET detectors. Between the discrete crystal elements, different type of reflective / interfaces materials (even left as air gap) have been tested or simulated in the designs of utilizing different light sharing schemes to localize the event crystal elements. The specular and diffused reflecting materials include aluminum foil [45][69][145], MgO paint [45][69][144], Teflon white paint [145], TiO_2 paint [146], filter paper (0.2 μm) [45], and Teflon tape (5 layers) [45]. It appears that Teflon tape and MgO paint are better reflectors; and the diffuse reflectors are preferable to specular reflectors in mirror polished crystals [45].

While using PS-PMT [22][23] or multi-channel PMT (MC-PMT) [32][45], the event crystal element is localized by PMT's position sensitive ability rather than relying on reading light sharing on the PMT's window. The materials that surround each crystal

element should be optical opaque that can isolate light transmitted to adjacent crystal element, and high reflectivity that could maximally recover the light transmitted outside the event crystal volume.

In our PEM-II detectors, each BGO crystal has a pattern of 10 × 10 elements in the near layer and 11 × 11 in the far layer. Each element attaches to the middle solid uncut region of only 2-mm thickness. The cut gaps between crystal elements are about 0.25-mm width after acid etching. The cut and etched crystals were very fragile. Overall, this pseudo-discrete crystal design with two-layer discrete element pattern prevents us from mechanically packing each element. Any additional mechanical processing may damage or even break the crystal elements by chance. Therefore, we chose to fill epoxy compound between the element gaps as crystal optical reflector.

4.5.1 Epoxy Compound

Epoxy is postulated to contain the following molecular grouping:

$$-\underset{\underset{O}{|}}{C}-C- \tag{4.1}$$

A typical epoxy molecule made from bisphenol-A and epichlorohydrin can be represented as:

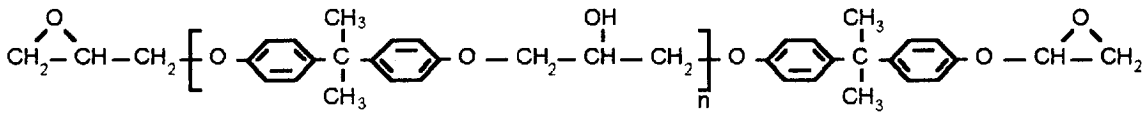

(4.2)

The value of "n", the repeating unit, is less than 1 for the lowest-molecular-weight liquid resins. As the value of "n" increased, the molecular weight also increased, and the material turns from a liquid into a solid resin [146].

Many different epoxies have been developed for connecting, splicing, bundling, coating, and encapsulating (potting) applications. Due to the various options, it is a challenge to choose an ideal epoxy suitable for a specific application. The main criteria is based on the epoxy's physical and chemical properties, which include the adhesive

strength, shrinkage and outgassing, curing and handling characteristics, consistency, and glass transition temperature (Tg) feature.

- ***Adhesives.*** The selected Epoxies should exhibit excellent adhesion to substrate like glass and crystal, so we can fill it to BGO crystal gaps. For example, EPO-TEK 301-2 has firmly adhesive ability to plastics, metals, and glass.
- ***Shrinkage and Outgassing.*** Solvent-free epoxy formulations are essential in crystal potting application because shrinkage is reduced to minimal levels when no solvent is released during the curing process. The absence of solvents also means there is no problem with outgassing, so minimal air bubbles could be generated and trapped inside resin in curing procedure. The optical-grade epoxy EPO-TEK 301-2 is an especially low-stress material, causing linear shrinkage of only 1.4 % during curing. This eliminates any possibility of cracking the very fragile BGO crystal elements. Based on outgassing test [147], The EPO-TEK 301 demonstrates a total weight loss of only 1.08 % after outgassing.
- ***Thermal Properties.*** Most epoxies are cured by exposing them to a specified temperature for adequate time. Cure temperature may range from room temperature to 150°C or higher. To avoid extra handling process with BGO crystals, we prefer epoxies with room temperature curing in crystal potting application. EPO-TEK 301-2 has the property of curing at room temperature (two days) or with heat (1.5 hour at 80°C).
- ***Shelf Life and Pot Life.*** Shelf life is the period of time for which the epoxy can be stored without any deterioration of physical, optical, or other properties. Epoxies exist in both single-component and two-component formulations. Two-component epoxy has the advantage of longer shelf life. Pot life is the period of time during which a two-component epoxy can be used after mixing without causing significant variation in its consistency. For example, two-component EPO-TEK 301-2 has shelf life around one year at room temperature, but once Part B (hardener) is mixed with Part A (resin), pot life is about eight hours. Toward the end of epoxy's pot life, the material will thicken and become more difficult to use.
- ***Viscosity.*** The consistency of uncured epoxies ranges from watery and free-flowing to the thick and non-flowing. Low viscosity materials tend to provide the widest possible

choice of application such as dispensing, coating. In our BGO crystal potting case, the viscosity of epoxy need to be especially concerned so that the selected epoxies can be poured into the crystal 0.25-mm very narrow gaps without trapping air bubbles. Very low-viscosity epoxies are suitable for crystal potting as they can flow easily between the crystal elements. Of this kind of epoxies, EPO-TEK 301-2 has low viscosity at only 300-600 centipoise (cps) @ 23°C/100 RPM.

- ***Glass Transition Temperature (Tg).*** Tg defined as the midpoint of the temperature region where the physical properties of an amorphous polymer (such as epoxy) shift from those of a hard, glassy state to those of a soft and rubbery condition. At temperatures above the Tg, the thermal coefficient of expansion (CTE) and elasticity are increased, while the strength of the bond formed by the adhesive is diminished. For example, EPO-TEK 301-2 has Tg around 80°C, the project operating temperature should be controlled to lower than this. It should also be taken into consideration that Tg is affected both by the formulation of the epoxy and by how it is cured. To maximize Tg, it is necessary to cure the epoxy for an adequate period of time [148].

4.5.2 Specified Epoxy and Color Paste for BGO Potting

The epoxy compound solutions chosen for our crystal blocks include two-component epoxy and an epoxy based white color, light opaque, and reflective paste. This is based on the suggestions of Andrew Truman from Dept. Physics, University of Southampton , and applied in our ANIPET and PEM detector [22][23][128].

Two Component Epoxy

Epoxy chosen for potting crystal elements is the product of "EPO-TEK 301-2" from Epoxy Technology Inc. [131]. Table I lists its characteristics.

This two-component epoxy has certain favorable features for crystal potting. It has a very low viscosity, thus is easily distributed through the crystal narrow gaps without trapping air bubbles; it also has low thermal expansion (62×10^{-6} in/in/°C), so does not produce exothermic heat while curing.

TABLE 4.1. CHARACTERISTICS OF PRODUCT 301-2 EPOXY

Number of Components:	Two components: "EPO-TEK" 301-2, part "A" (base epoxy), and part "B" (hardener)
Mix ratio:	100:35 Parts by Weight
Cure Temperature (minimal):	80°C - 1.5 hour / RT - 2 days
Viscosity @ 23°C:	@100rpm 300-600 cps
Index of Refraction:	1.564
Spectral Transmission:	>96% 300-900nm
Color Before/After Cure (thin film):	Clear/Clear
Lap Shear Strength (psi):	2000
Shore D Hardness:	82
Tg:	>65°C 80°C/3 hours
CTE Below Tg/Above Tg (in/in/°C):	62 x 10-6 / 177 x 10-6
Pot Life @ Room Temperature:	8 hours
Shelf Life @ Room Temperature:	1 year

Epoxy Color Paste

The selected epoxy colors are clear both before and after cure (see Table I). But the purposes of cured epoxy in crystal gaps are using it as both optical reflection and isolation. So we added an epoxy based coloring paste REN DW-0131 mixed into the EPO-TEK 301-2 epoxy.

REN DW-0131 is the coloring paste from Ren Shape Tooling system [132]. It is in a package of an easy-to-blend tube. There are seven pasting colors (white, red, blue, black, yellow, green, and brown) for customer coloring of epoxy, polyurea and polyurethane materials [133]. In our application, white color is chosen to paste the EPO-TEK 301-2 epoxy in order to maximally reflect photons back to the BGO scintillating crystal element.

4.5.3 Epoxy Resin Crystallization and Solutions

The manufacture data of epoxy compound EPO-TEK 301-2 that we ordered from Epoxy Technology [131] was September 18, 2001. When we wanted to encapsulate more BGO crystals in December 12, 2001 (less than three months after epoxy manufactured), we found that about half of epoxy base resin (part A of EPO-TEK 301-2) has been crystallized - the resin shows up as a lot of free floating crystals and solidified masses. But the shelf life of EPO-TEK 301-2 is one year. Then we contacted with Epoxy Technology to inquire. As described from Ms. Hope Jones [134], technical and application staff of Epoxy Technology, "Crystallization in base resins and two component formulations is a major inconvenience but not an insurmountable problem" [135]. To deal with the crystallization, it is necessary to understand the influence factors and find possible solutions.

Epoxy Crystallization

Crystallization shows up as cloudiness, free-floating crystals, crystal masses, or as a completely solidified mass. It is the phase change of a material from a liquid to a solid crystalline state. Because the main ingredient of most epoxy resins is a solid material at room temperature, the phenomenon of crystallization is possible in all epoxy resins and hardeners.

The factors that contribute to the crystallization process are due to the properties of epoxy resin and its storage conditions. High purity, low viscosity, impurities, extreme cold, and temperature cycles environment all increase the probability of occurrence [135]. Usually the presence of a "seed" initiates the crystallization process. The seed crystals in combination with other factors can rapidly change the liquid to a solid.

A high purity resin has been stripped of all chemical byproducts and contaminants and falls within a given range of molecular weights. It has a narrow temperature range during which it transforms from liquid to solid. When a high purity epoxy resin gets to the point where it changes from a liquid to a glassy crystalline solid state, the minute crystals acting as seeds will start to form.

Low viscosity epoxies are very low in molecular weight and short chained. The lower the viscosity the easier a liquid epoxy can move and orient itself around seed crystals.

Impurities (usually minute particulate matter) often act as seeds initialing the formation of resin crystals. Storing a seed free epoxy liquid at low temperature (0°C) will slow molecular motion and impede crystal formation and growth. But extreme cold temperature (–40°C) accelerates crystal formation once seed crystals have formed. Low enough cold can cause complete crystallization by itself without seed.

Temperature cycles as 20-30°C is the most common cause of crystallization. Once the epoxy is warmed, molecular motion is enhanced allowing liquid epoxy to orient itself around seed crystals. Subsequent cold temperature will then accelerate crystal growth. The temperature fluctuations that occur between daytime and nighttime temperature can initiate and accelerate the crystal growth process.

Solutions with Epoxy Crystallization

Minimizing temperature fluctuations in epoxy resin storage conditions may eliminate the phenomenon of crystallization. When crystallization occurs, heating method seems to be the only solution to two component epoxy formulations. Heating crystallized epoxy base resins at 50-60°C several hours would reverse the phenomenon. In practice, 226.8 g (8 oz) EPO-TEK 301-2 base epoxy resin needs three hours heating when about half was crystallized.

Along with the gentle hearing, epoxy resin should be stirred to assure the heat is being evenly distributed. All the crystals must be completely melted as any microscopic remain crystals will act as seeds and cause the crystallization to return in days. If crystals appear, merely apply heating method to melt it.

There is no good solution for crystallization of one component epoxy resin. Heating method to one component epoxy should not be used as product damage or curing may occur. If the epoxy is within the stated shelf life and the recommended storage conditions, it many have to be returned for replacement.

4.5.4 Epoxy Decapsulating Methods

Epoxies are usually noted for their chemical resistance. They are also rigid adhesives and tend to have higher temperature resistance than other organic adhesives. So

removing, or "decapsulating" the cured epoxy would be very difficult. Several techniques have been tested as kinds of "effective" in removing process [149]. The methods include chemical solution processing (chlorinated solvents such as methylene chloride, warm solution of sulfuric acid, toluene...), combination of heat and pressure, temperature degradation (burns away epoxy to carbon ash at temperatures of 400°C), using boiling water with prying action, thermal shock, etc. As mentioned in [149], several of above techniques can be "suicidal" in terms of re-useable parts. We believe that it would be extremely difficult to remove (decapsulating) epoxy coating from our BGO block due to the fact that epoxy is cured inside the very narrow (0.01 inch) gaps; with 10 × 10 (the near layer) and 11 × 11 (the far layer) crossed patterns. Furthermore, the epoxy is adhered to fragile crystal elements that we would rather to keep undamaged. So we should take great cautions in epoxy potting process in order to avoid those very uncertain epoxy-removing procedures.

4.5.5 New Epoxy Compound

Recommended by Mr. Michael J. Hodgin [138], a new Epoxy compound T905-BN2 has been applied as crystal reflector. This new epoxy has very high optical reflecting ability. Due to its very high viscosity, the T905-BN2 is suitable for coating individual polished crystal elements.

4.5.6 "PET" Film - Lumirror

"Lumirror", a biaxially oriented polyester film [139], has been applied as crystal reflecting material [140]. One of our proposals is to get the 0.01-inch thickness customer ordered Lumirror film, then accurately cut the film to a frame as demonstrated in Fig. 4.11. The size follows the dimension of proximal layer. Twenty pieces of same frames can construct proximal layer reflector (Fig. 3.12). Distal layer reflector can follow same structure.

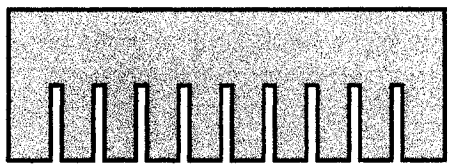

Fig. 4.11. This is the one of comb shape frame used for creating the form as crystal reflector (proximal layer). The frame could be a customer ordered 0.25 mm (0.01 inch) Lumirror.

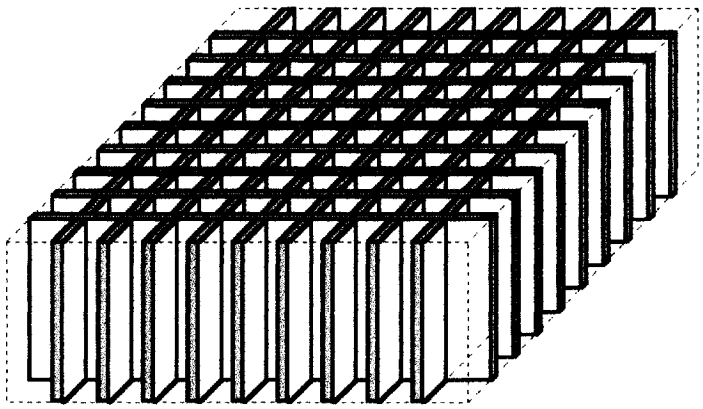

Fig. 4.12. This is the scheme of crystal reflector form for crystal proximal layer.

4.5.7 SPECTRALON and SPECTRAFLECT

Unlike plumber's Teflon tape and Lumirror film, the "professional" reflectance coating and materials can be found from Labshpere Inc. [141]. The reflective material SPECTRALON (SRM-990-Optical-Grade) and coating SPECTRAFLECT [142] are very attractive. Especially, SPECTRALON has the highest diffuse reflectance of any known substance [143]. It can also be built to different shapes as customer needed.

CHAPTER V

FRONT-END ANALOG CIRCUITS IN THE PROTOTYPE PEM-II DETECTOR

Previously, positron emission mammography (PEM-I) systems [22] and animal positron emission tomography (ANIPET) systems [23] have been developed and constructed in our Lab. The detectors in PEM-I and ANIPET systems consist of BGO crystal blocks optically coupled to Hamamatsu R3941-05 PS-PMTs. The detector field-of-view (FOV) is 56 mm × 64 mm. The timing resolution is 8.7 ns [29].

Recently, we designed and developed new high spatial resolution PET detectors for small animal and breast imaging. In these detectors, PS-PMT (R7600-C12) and dual-layer pixelated BGO crystals are employed to detect and localize gamma rays. Modified high-voltage dividers with last dynode readout circuits, front-end anode position and last dynode timing schemes have been investigated and developed for these detectors. Methods for combining four PS-PMTs with simple four (X^-, X^+, Y^-, and Y^+) outputs have been developed to further simplify the position processing. The front-end circuits are small so they can be fitted into the detector's structure. A prototype of two detector modules, each having two PS-PMTs with corresponding electronic circuits, has been built for evaluation. The crystal elements of 10 × 10 in the near layer and 9 × 9 in the far can be clearly identified.

5.1 Position Sensitive Photomultiplier Tube

Hamamatsu PS-PMT R7600-C12 [124] was used for our new PEM-II detectors. It is a metal-channel type PMT fabricated with stacked thin electrodes. The PMT is constructed with a compact metal package instead of the traditional glass envelope. One advantage is the PMT package (envelope) wall is very narrow, so the periphery dead region of the PMT light input window (faceplate) is very small. The PMT has outer dimensions of 26

mm × 26 mm, and the effective window is 22 mm × 22 mm. It is in a "flangeless type"; therefore the PMT has very flat faceplate, and it has better gain uniformity crossing the PMT window. The high voltage of the PMT can be up to negative 900 volts. The gain of the PMT is about 7×10^5. It also has fast time response – the anode pulse rise time is about 1.4 ns. The dynodes of the PMT have 11 stages, Hamamatsu gives a typical high-voltage divider schematic. The position sensitive feature is attained by reading out the cross plate 6 (X) + 6 (Y) anode outputs.

As the PMT is a vacuum device, is should be installed and handled with caution. The PMT faceplate, metal package, or pin to be pushed, to be scratched, or the PMT to be subjected to a shock might cause vacuum air leakage. Especially the vacuum exhaust very sharp tip portion should not be touched as it can be damaged easily. Light illumination to the PMT also needs to be concerned. Even when the PMT is not operated, strong illumination (like direct sunlight) striking the faceplate could permanently damage the tube.

When we assemble the PMT with BGO crystal, the PMT faceplate, base and socket should not be touched with bare hands. Dirt and fingerprints on the faceplate may cause transmittance loss; they can cause ohmic leakage on the high voltage base. The PMT can be wipe clean with alcohol.

Electrostatic Potential on PMT Package and HA coating

The polarity of the photomultiplier power-supply voltage with respect to ground can be positive or negative. Certainly the cathode must be always negative with respect to the anode. In some application, the cathode is grounded and the anode operated at a high positive potential with a capacitance-coupled output. In this case, the PMT magnetic or electrostatic shields should be connected to ground potential (photocathode potential).

In application of the cathode is at a high negative potential with respect to ground, extra precautions must be taken in the mounting and shielding of the tube. Operation of a PMT with an improper potential on the external shield may not only cause an increase in dark noise. If PMT envelope has some potential like ground, the electron path inside of the PMT might be changed, and the electron might hit the glass envelope. In this case, radiation from glass (glass scintillation) will be created. Since PMT is so sensitive and

easy to detect such radiation light, that radiation will cause of noise [150]. The improper potential on the faceplate can result in permanent damage to the photocathode by ionic conduction through the glass 0. If glass scintillation occurs in the faceplate, it can cause deterioration of the photocathode sensitivity. Once deteriorated, the sensitivity will never recover to the original level [20]. Furthermore, the proximity of a positive potential near the PMT envelope can cause a noisy operation even there is no an actual contact.

In order to prevent these effects, the envelope wall should be maintained near photocathode potential by wrapping or painting it with conductive material (Hamamatsu names this normally black conductive material as "HA coating") and connecting this material to cathode potential. The connection is usually made through a high impedance to reduce the shock hazard to personnel. If a cathode potential shield is not provided, the glass surface in the vicinity of the photo cathode must be insulated from any source of potential difference so that leakage currents to the bulb are less than 10^{-12} ampere 0.

The high-voltage of Hamamatsu PS-PMTs R3941 (for our PEM-I and ANIPET) and R7600 (for PEM-II) are all in negative polarity - grounding the anode with a high negative voltage applied to the cathode. R3941 is in a glass envelope with HA coating on it. A black tube from high isolation material is surrounded the HA coating for safety.

The metal package of R7600-C12 is connected to cathode voltage potential. As the PMT is operated under negative high voltage (we used negative 800 volts), the metal package also becomes negative high voltage. There is no any isolation from the high voltage in the PMT package. So we should have enough safety measure to prevent an operator from electric shock and equipment damage.

5.2 Front-End Position and Timing Circuits

The front-end electronics in our new detectors include crossed anode read-out circuits, modified high-voltage dividers, position preamplifier circuits with voltage-feedback amplifiers, and timing preamplifier circuits with current-feedback amplifiers. We investigated a method of combining four PS-PMTs with simplified four (X^-, X^+, Y^-, Y^+) outputs to further simplify the position processing [136].

5.2.1 Anode Position Read-out Schemes

Many different schemes for anode readout circuits [21][63][72][84]-[86] are based on the fact that a PMT behaves as an almost perfect current generator - the anode current depends only on the incident flux and is completely independent of the load [8]. The common method of reading out anode signals from a single PS-PMT is to combine all X or Y anode wires through a resistor divider chain. Then only four (X^-, X^+, Y^-, Y^+) position signals are output, regardless of the number of anode wires. Since the PS-PMT R7600-C12 has 6(X) + 6(Y) anode wires, this method reduces the number of processing signals by a factor of three.

Each detector panel in our new PEM and ANIPET cameras comprises sixteen R7600-C12 PS-PMTs. After going through the divider chain, we need to process 4 (X^-, X^+, Y^-, Y^+) × 16 (PMTs) individual position signals for each detector. So it is necessary to investigate further compression methods to simplify the electronics complexity. Some approaches, like combining PMTs through common X and Y resistive dividers, have been applied in the detector with multiple multi-channel PMT (MC-PMT) and PS-PMT applications [72][84][85].

We developed a new method to simplify the position circuits by combining four PS-PMTs with four (X^-, X^+, Y^-, Y^+) position outputs. The new arrangement will reduce the number of processing signals by an additional factor of four. In the low count rate application, this method can be extended to achieve more compression by combining 9 or 16 PS-PMTs while keeping the number of outputs fixed at four.

Each detector module with 2 × 2 PS-PMTs has individual position circuits. Fig. 5.1 illustrates the schematic for a module with four PS-PMTs (A, B, C, D). The multi-anode wires of PS-PMTs A and B (C and D) are combined through common X resistive dividers. The anode wires of PS-PMTs A and C (B and D) are combined through common Y dividers. Eight charge sensitive preamplifiers (X_{AB}^-, X_{AB}^+...) integrate the output signals from each end of the resistor chain. After four sum circuits, we have four (X^-, X^+, Y^-, Y^+) outputs for position identification.

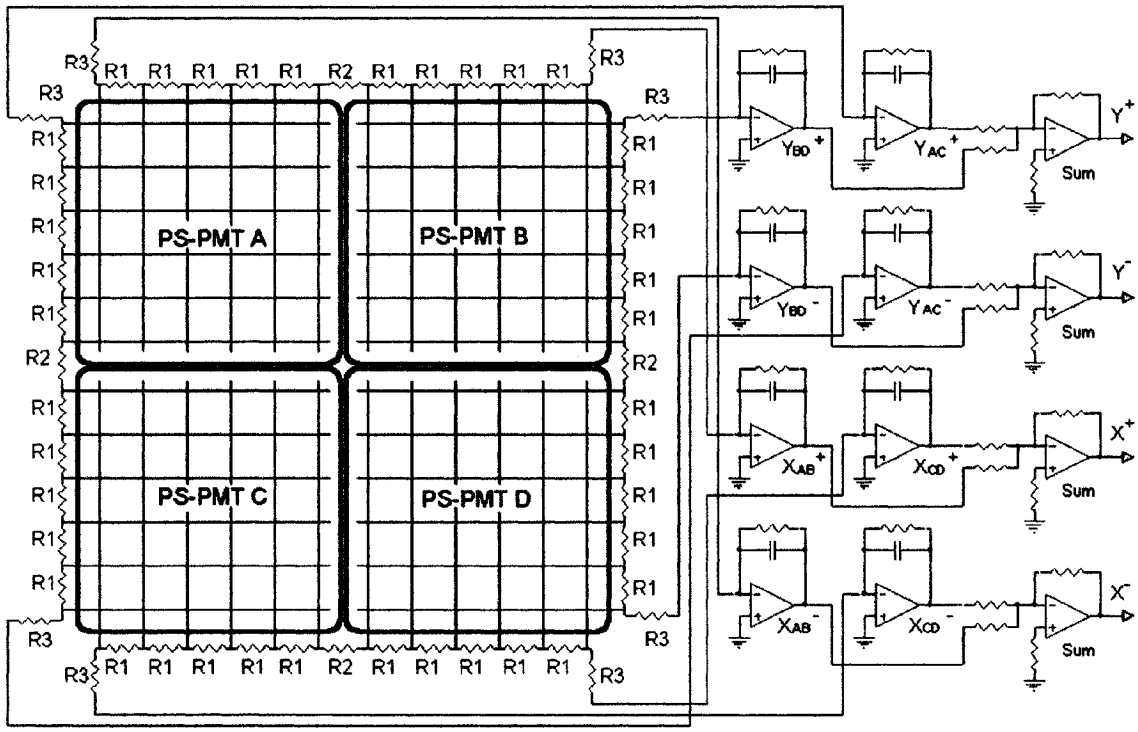

Fig. 5.1. Four PS-PMTs are combined together to build up one block to further simplify the position read-out circuits. All R1 resistors are 100Ω, R2 are 20Ω, and R3 are 70Ω. The charge sensitive preamplifiers are LT1880.

Consider the case of one photon interaction occurring in a crystal element coupled to PS-PMT A. Four integrators (X_{AB}^-, X_{AB}^+, Y_{AC}^-, Y_{AC}^+) will give position signals; another four integrators (X_{CD}^-, X_{CD}^+, Y_{BD}^-, Y_{BD}^+) stay at the background level (with electronic noise). A final position signal (for example, X^+) is the sum of signal (X_{AB}^+) with background noise (X_{CD}^+). In order to achieve a high signal-to-noise ratio, the sum amplifiers are placed after the integrators.

The event position can be located by:

$$X = \frac{X^+ - X^-}{X^+ + X^-} \tag{4.1}$$

$$Y = \frac{Y^+ - Y^-}{Y^+ + Y^-} \tag{4.2}$$

Each integrator in Fig. 5.1 is the classical second order model with a fast VFA, a feedback resistor R_f, and a charge storage capacitor C_f. The output voltage magnitude (V_M) of the charge sensitive amplifier is:

$$Vm \approx Q/C_f \tag{4.3}$$

Q is input charge with:

$$Q = \int_0^{t_w} i_t \cdot dt \tag{4.4}$$

where i_t is current output from the PMT anode, and t_w is the signal duration time. The feedback resistor R_f (~ 1MΩ) discharges C_f (~ 1.2pF) in continuous operation. R_f also gives the DC negative feedback to stabilize DC working points.

Only VFAs are suitable for integration purposes. The low bias current, high precision VFAs CLC420 and the latest LT1880 [151] were tested for our integrator circuits.

5.2.2 Last Dynode Output from HV Divider

Typically, the event-timing trigger is acquired by discriminating the energy signal from the anode output. Due to the multi-anode output structure in the PS-PMT, the electronics is simplified by taking the timing from one dynode output rather than from the sum of multi-anode signals.

The last dynode is chosen for taking event timing because:

The dynode signal is synchronous with anode output so it can be chosen for anode timing measurement [8].

The signal taken from the last dynode has an amplitude comparable to that from the anode. It has a higher signal-to-noise ratio than the other dynodes.

The Hamamatsu HV divider for R7600-C12 PS-PMT was modified in order to read out a signal from the last dynode for event timing. Fig. 5.2 shows the schematic.

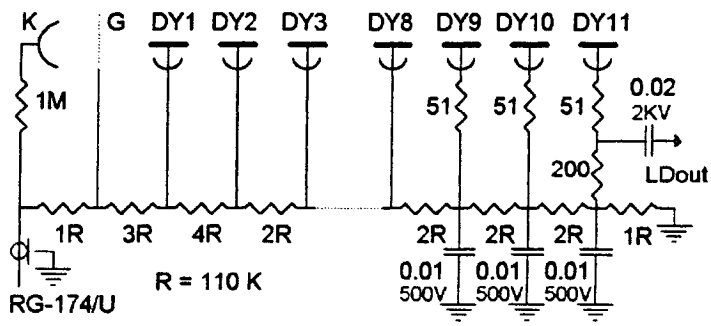

Fig. 5.2. This is the modified divider circuit. LDout is the last dynode output.

The main problem with this modification is how to obtain the signal from the last dynode without disturbing the anode signals. Compared with the manufactured HV divider circuit, three 0.01μF decoupling capacitors were changed from series decoupling to parallel. Fig. 5.2 shows a 200Ω resistor connected before the dynode output. This resistor needs to be large in order to output a high amplitude signal with a higher signal-to-noise ratio. On the other hand, if it is too large - the voltage across it exceeds a few volts - the dynode output could disturb the anode signals. When a 50Ω characteristic impedance coaxial cable is selected to transmit the dynode signal, a resistor of 200Ω to 300Ω is appropriate [8]. Because the last dynode still has about 30V (negative) voltage potential, a high voltage capacitor (0.02μF in Fig. 5.2) is used to AC couple the dynode output. The signal from the dynode has an opposite polarity from that of the anode. Fig. 5.3 shows the PS-PMT socket with modified high-voltage divider and anode resistor chains. The signal from PMT last dynode is taken out from the socket for event timing.

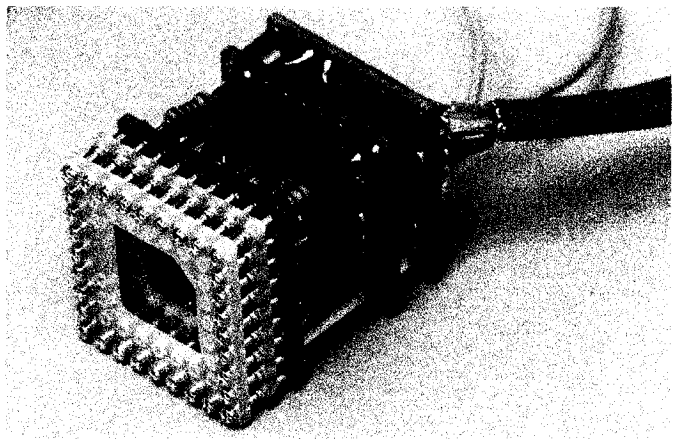

Fig. 5.3. This is a completed high-voltage divider socket with anode readout resistor chain circuit. One extra PGA socket is attached for preventing the vacuum air exhaust tip portion in the R7600-C12 PS-PMT from accidentally touching resulting in permanent PMT damage.

The CFA CLC450 (shown in Fig. 5.4 as transimpedance amplifier) was chosen to convert dynode current output to a fast response voltage signal. Compared with VFA, CFA with transimpedance setting gives a signal with a faster leading edge so it is ideal for accurate timing. Another important feature of CFA is that its inverting input impedance is very small. So CFA has much less sensitivity to inverting input capacitance [152]. With transimpedance setting (inverting mode as I/V converter), CFAs are suitable for

compensating the capacitance from PMT output. In practice, a small value feedback capacitor C_f between 1.0pF to 5.0pF is used to compensate for PS-PMT output capacitance. The feedback resistor R_f is 1KΩ.

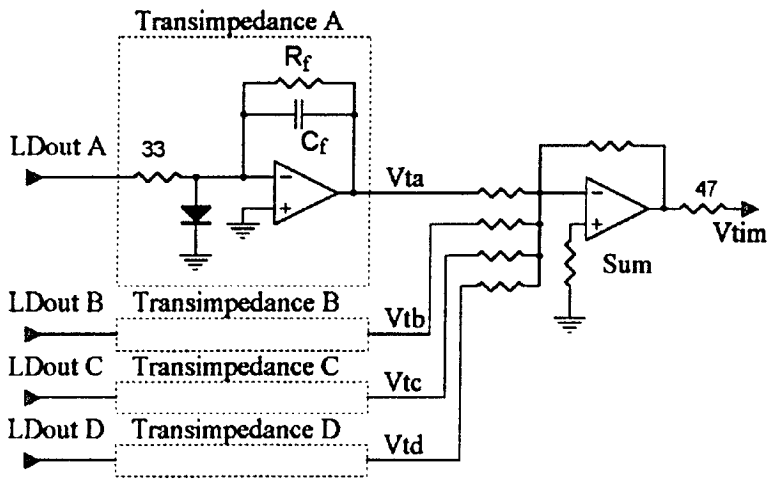

Fig. 5.4. This is schematic of timing amplifiers with transimpedance configuration. Sum and buffer amplifier is CLC420.

As shown in Fig. 5.4, each current output (LDout A, B, C, D) from a PS-PMT last dynode is converted to a voltage signal (Vta, Vtb, Vtc, Vtd) by the transimpedance amplifiers. The timing trigger (Vtim) of one detector module is simply the sum of these four voltage outputs.

Combining this timing scheme with the position read-out arrangement, one detector module with four PS-PMTs looks exactly like a four times larger PS-PMT - it has four (X^-, X^+, Y^-, Y^+) position outputs and one timing output.

5.2.3 Fast-Slow Preamplifier Design

The fast-slow preamplifier design is generally used in PET front-end electronics. The slow circuits are for position locating by integrating the anode outputs up to 800 ns in BGO scintillator applications [58]. The fast circuits are for timing processing to trigger the possible coincidence event.

The position preamplifiers usually employ wideband JFET input operational amplifiers because of their reduced input bias current. When precision is required, JFET amplifiers

are generally inadequate due to their relatively higher input offset voltage and drift [151]. Based on this consideration, we use high precision voltage-feedback amplifiers (VFAs) in the position charge sensitive preamplifier circuits.

In order to respond quickly to event timing, we chose the high bandwidth and ultra-fast setting time current-feedback amplifiers (CFAs) in our timing amplifier circuits. Compared with VFAs, CFAs have very low inverting input impedance, so they are less affected by inverting input capacitance [152]. This specification meets our needs because we know the phase shift caused by the PMT capacitance is often a source of instability.

5.2.4 Circuit Simulation and Printed Circuit Design

The Spice simulation software "Circuit Simulator" (an enhanced version of Berkeley SPICE3f5/Xspice) which is embedded in Protel 99/SE [154] was used to verify the schematic design.

The position integrating and timing amplifying circuits stack up are shown in Fig. 5.5. The printed circuit boards (PCBs) are in miniature so they can be fit in the detector enclosure. The main amplifier board, which will be mounted in a NIM module near the workstation is displayed in Fig. 5.6.

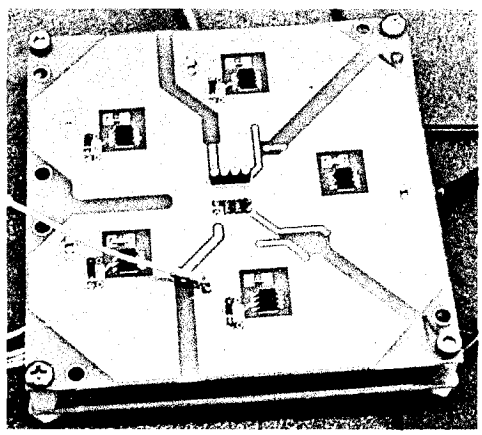

Fig. 5.5. This is the stack up of the front-end position integrator (bottom printed circuit board) and the last dynode timing amplifier circuit (top printed circuit board). The dimension of the board is 100 mm × 100 mm.

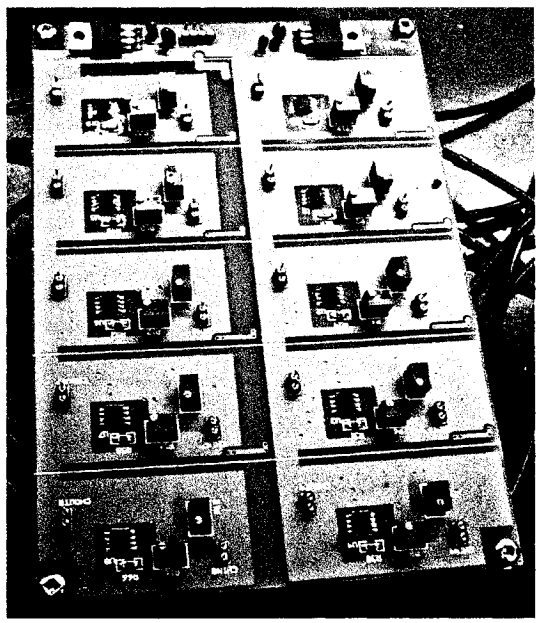

Fig. 5.6. This is the main amplifier buffer printed circuit board. The gain and DC offset are adjusted in this board. The dimension of the board is about 118 mm × 166 mm.

5.3 Detector Array, Module, and Unit Configuration

Detector Unit

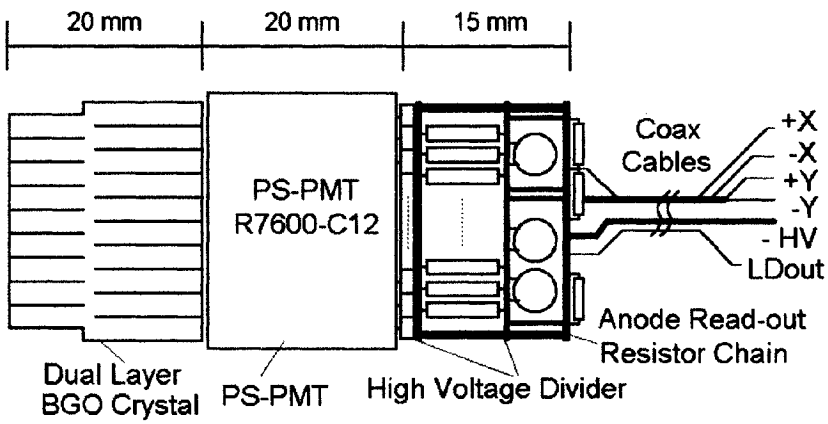

Fig. 5.7. This is the stack up layout of one detector unit. Two circuit boards with connecting resistors and capacitors function as the high voltage divider. The layout is roughly to scale. The length of one unit is about 55 mm (before coax cables).

An individual detector unit is shown in Fig. 5.7, which includes a BGO dual-layer crystal, PS-PMT R7600-C12, the HV divider, and the anode read-out resistor chain circuits. The dimensions of an uncut crystal are 22 mm × 22 mm × 20 mm. Each crystal

block has been pixelated into small elements of 2.1 mm × 2.1 mm (2.2 mm pitch) on two opposite faces. The elements on one face of the block offset by half the crystal pitch from those on the opposite face in both X and Y dimensions. The depths of near and far layer are 11.5 mm and 6.5 mm, respectively. The space between the near and far layers is 2 mm. The 1.1 mm width outer elements in the far layer are removed after the crystal block is cut.

Array, Module, and Unit Configuration

Pileup effect with a number of PS-PMTs in combination [85] was one issue we had to consider in our detector structure design. Because our BGO scintillation crystal has a complex dual-layer structure, the readout circuits should be capable of identifying all crystal elements. Detecting position accuracy was therefore another issue we were concerned with.

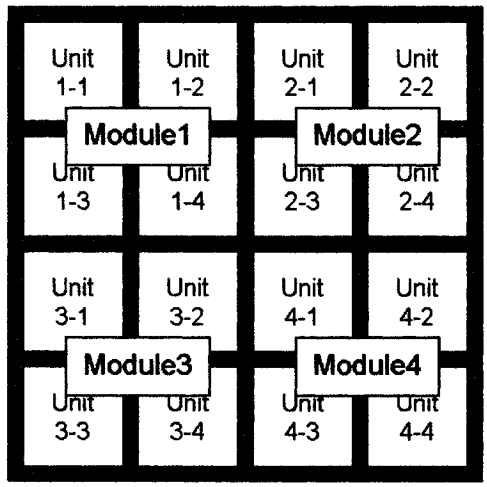

Fig. 5.8. This is the configuration map of one detector array. Each array has four modules. Every module has four detector units.

The PEM-II system is constructed with two detector arrays; each one is divided into four modules; each module consists of four detector units; each unit has one dual-layer BGO crystal optically coupled to a PS-PMT. The basic detector unit is designed as "field-replaceable-unit". Each detector module has its own position and timing electronic circuits with (X^-, X^+, Y^-, Y^+) and a timing trigger output. One module in a detector array can have coincidence with any module in the opposite detector array. The coincidence

events in different module pairs can be processed simultaneously. Fig. 5.8 shows the detector array-module-unit structure.

Each detector module has its own position and timing electronic circuits with (X^-, X^+, Y^-, and Y^+) and a timing trigger output. Signals from each module in one detector array can coincide with any module in another detector array. The coincidence events in different module pairs can be processed simultaneously.

5.4 Discussion

It is very important in PEM scanners to make the sensitive area of the detector extend to their physical edges. This allows improved imaging near the patient's chest wall, and the detectors to be packed without gaps in the sensitive area. So far we have used axial through-hole resistors and HV ceramic disc capacitors to build our HV divider circuits. The axial dimensions can be reduced by applying surface mount resistors and capacitors.

A method of simplifying the electronic processing channels by combining four PS-PMTs has been proposed. One consideration in our circuits is to modify the charge sensitive preamplifiers (Fig. 5.1). While the rising edge of the preamplifier output is mainly defined by the value of C_f and the amplifier bandwidth, the falling edge is defined by C_f and R_f. In order to integrate over 300ns (the BGO primary decay time), R_f is very large, normally above 1MΩ. Since the falling edge of the integrator output is quite slow with a timing constant τ ($R_f \times C_f$) over 1μs, other discharge schemes, such as applying an analog switch [58] and using an additional non-inverting low-gain amplifier [153], will be tried in future experiments.

CHAPTER VI

OPTIMIZING POSITION READOUT CIRCUITS IN PET FRONT-END ELECTRONICS

Most of the front-end position readout circuits in positron emission tomography (PET) detectors originate from the Anger logic design. In PET detectors with position-sensitive photomultiplier tubes (PS-PMTs) and multi-channel photomultiplier tubes (MC-PMTs), anode position readout circuits are more complex due to multi-anode outputs from a single PMT. To simplify the circuits, many researches have investigated different schemes by combining multiple PMTs with simplified X^-, X^+, Y^-, Y^+ outputs.

In this chapter, we aim at optimizing the performance of the position readout electronic circuits. First, we compared the signal-to-noise ratios in different position readout schemes. Then we examined the truncation and round-off errors in the irradiation-image processes by applying the Root-Sum-Square (RSS) analysis and the Uniform Distribution simulation methods. Furthermore, we investigated the gain adjustment and balance issues in the X^-, X^+, Y^-, Y^+ analog signal channels.

The performance of the front-end position readout circuits determines the event location in which a gamma ray interaction occurs; thus, it affects the PET spatial resolution. In order to optimize these circuits, we analyze them from the following aspects:

- Noise in different position readout schemes.
- Artifacts in the irradiation images.
- Gain optimized adjustment.
- Gain balanced adjustment.

We demonstrated that an eight-bit analog to digital converter (ADC) is probably insufficient in the position recording if a gamma-ray event position is calculated from digitized X^-, X^+, Y^-, Y^+ signals. We also reveled that an energy non-uniformity error could occur if the signal gains in the front-end analog circuits are improperly adjusted. As

a result, the quantitative gain adjustment criteria are given to optimize the PET position readout circuits.

6.1 Noise Analysis in Different Anode Readout Schemes

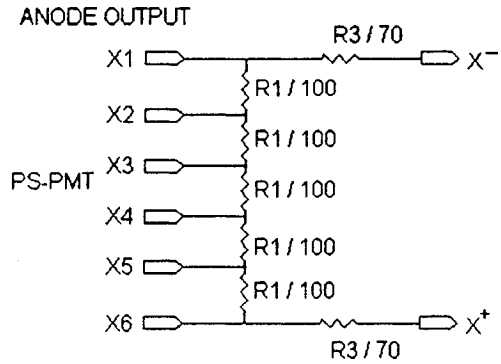

Fig. 6.1. This is an anode readout resistor-chain for a single PS-PMT. We mark the circuits as "a".

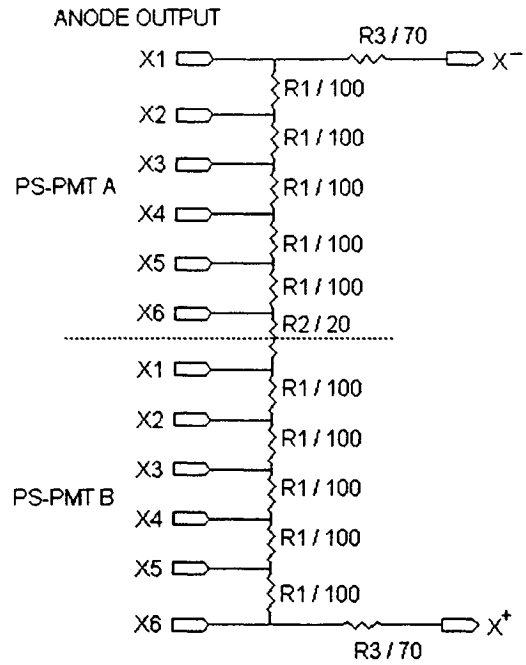

Fig. 6.2. This is the PEM-II anode readout resistor chain, which is constructed with two "a"; thus named "2a".

Many researchers have investigated different schemes by combining multiple PMTs with simplified (X^-, X^+, Y^-, Y^+) outputs [72][84][85]. In these designs, great efforts have

been taken in how to effectively reduce the readout complexity. However, the signal-to-noise issue is also necessary to be addressed.

Fig. 5.1 shows the schematic of our PEM-II position readout circuits. An anode readout resistor chain for a single PS-PMT is illustrated in Fig. 6.1 [124]. For clarifying, the anode readout resistor chain circuit in Fig. 5.1 is depicted in Fig. 6.2.

Since a PMT anode output is nearly an ideal current source [8], the current from each anode only depends on the incident flux and will not be affected by readout circuits. However, after passing through the resistor chain, the current signals from X^- and X^- in Fig. 6.2 (circuit "2a") is only one-half AC amplitude of that in Fig. 6.1 (circuit "a"), with biasing a DC offset.

Assuming the current noise from each anode is the same, the current noise output of the circuit "2a" is $\sqrt{2}$ times larger than the one in the circuit "a". Overall the signal-to-noise ratio (SNR) of the simplified anode readout circuit is $2 \cdot \sqrt{2}$ times degradation.

The anode readout resistor chain in Fig. 6.2 (circuit "2a") is basically formed from two individual PMT resistor-chain circuit of Fig. 6.1 (circuit "a"). In general, if a simplified circuit is constructed from "n" individual circuit "a", the SNR degradation is:

$$\frac{SNR(na)}{SNR(a)} \approx \frac{1}{n\sqrt{n}} \tag{6.1}$$

In conclusion, the simplification of the circuits is obtained by trading off SNR degradation. Even our position readout scheme can be applied into 3 × 3 and 4 × 4 PS-PMT combinations, in spite of count-rate and pile-up issues in these circuits, the crystal elements in the irradiation images will be more difficult to be identified because of the SNR's degradation.

6.2 Artifact in Irradiation Images

After digitizing by an analog-to-digital converter (ADC), list mode data with XA, XB, YC, YD (digitized X^-, X^+, Y^-, Y^+) are acquired to generate 2D crystal irradiation images. These intensity images are accumulated from each event - its address is calculated by:

$$Xp = 128 \times \left(1 + \frac{XB - XA}{XA + XB}\right) \tag{6.2}$$

$$Yp = 128 \times \left(1 + \frac{YD - YC}{YC + YD}\right) \tag{6.3}$$

Fig. 4.2 shows the structure of the bismuth germanate (BGO) crystal used in our PEM-II detector. In order to accentuate the image artifacts, we generated irradiation images by side irradiating the uncut region of a BGO crystal with a highly collimated ^{137}Cs source. The list mode data were acquired with a 12-bit ADC, and the 12-bit data were truncated to 10 and 8 bits for analysis (Fig. 6.3).

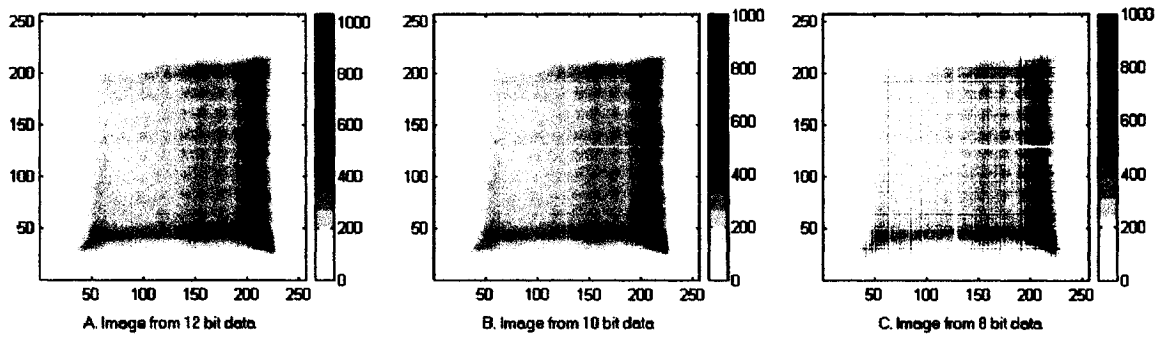

Fig. 6.3. The irradiation images of A, B, and C are created from 12 bit, 10 bit and 8 bit data, respectively.

Two types of errors, truncation and round-off error, occur in the irradiation image processes [155]-[159]:

- Truncation error - Error due to the ADC digitization of truncating analog X^- to digital XA, X^+ to XB, Y^- to YC, and Y^+ to YD.
- Round-off error - Error due to digital rounding process in (6.2) and (6.3) calculations.

We applied the Root-Sum-Square (RSS) method to analyze the truncation and round-off errors. The RSS value is calculated as [159]:

$$V(X) = E\left((X - E(X))^2\right) = \frac{1}{n}\sum_{i=1}^{n}(x_i - E(X))^2 \tag{6.4}$$

where X is a random variable with possible values of $\{x_1, x_2, ...x_n\}$, $E(X)$ is an expected value.

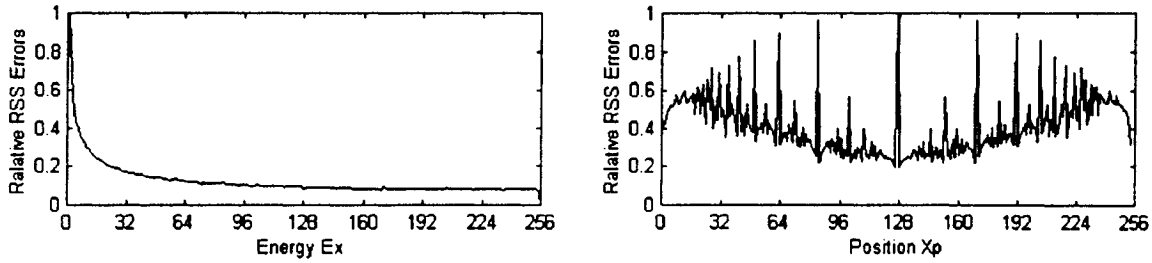

Fig. 6.4. These are the RSS analysis results. The left depicts the function of error RSS vs. energy Ex; the right shows error RSS vs. image address Xp.

The artifacts of an irradiation image in X-axis are analyzed according to (6.2). We applied the Uniform Distribution simulation method [158] to analyze the RSS function. Fig. 6.4 shows the functions of the unified RSS vs. event energy Ex $(Ex = XA + XB)$ and the unified RSS vs. event X-axis position Xp (Xp is defined in (6.2)), respectively. As can be seen, the lower energy gamma rays (scattering events) would cause more artifacts; and the artifacts mainly located at the address 127; 84 and 170; 63 and 191; 50 and 204; etc.

As revealed in Fig. 6.3, the 8-bit image (C) shows noticeable artifacts compared with 10-bit (B) and 12-bit (A) images. So 8-bit ADC is probably insufficient in the position recording if a gamma-ray event position is calculated from digitized X^-, X^+, Y^-, Y^+ signals.

6.3 Optimizing Gain Adjustment

We re-examined the irradiation images from our PEM-I system with an energy-banded window technique. The irradiation images were re-generated with different energy windows, from (32 - 63), (64 - 95), to (223 - 256). The energy-banded images reveal that while the banded window goes higher, the region of the irradiation image becomes gradually smaller. This indicates that an energy non-uniformity error could be created if the signal gains in the front-end analog circuits are adjusted improperly.

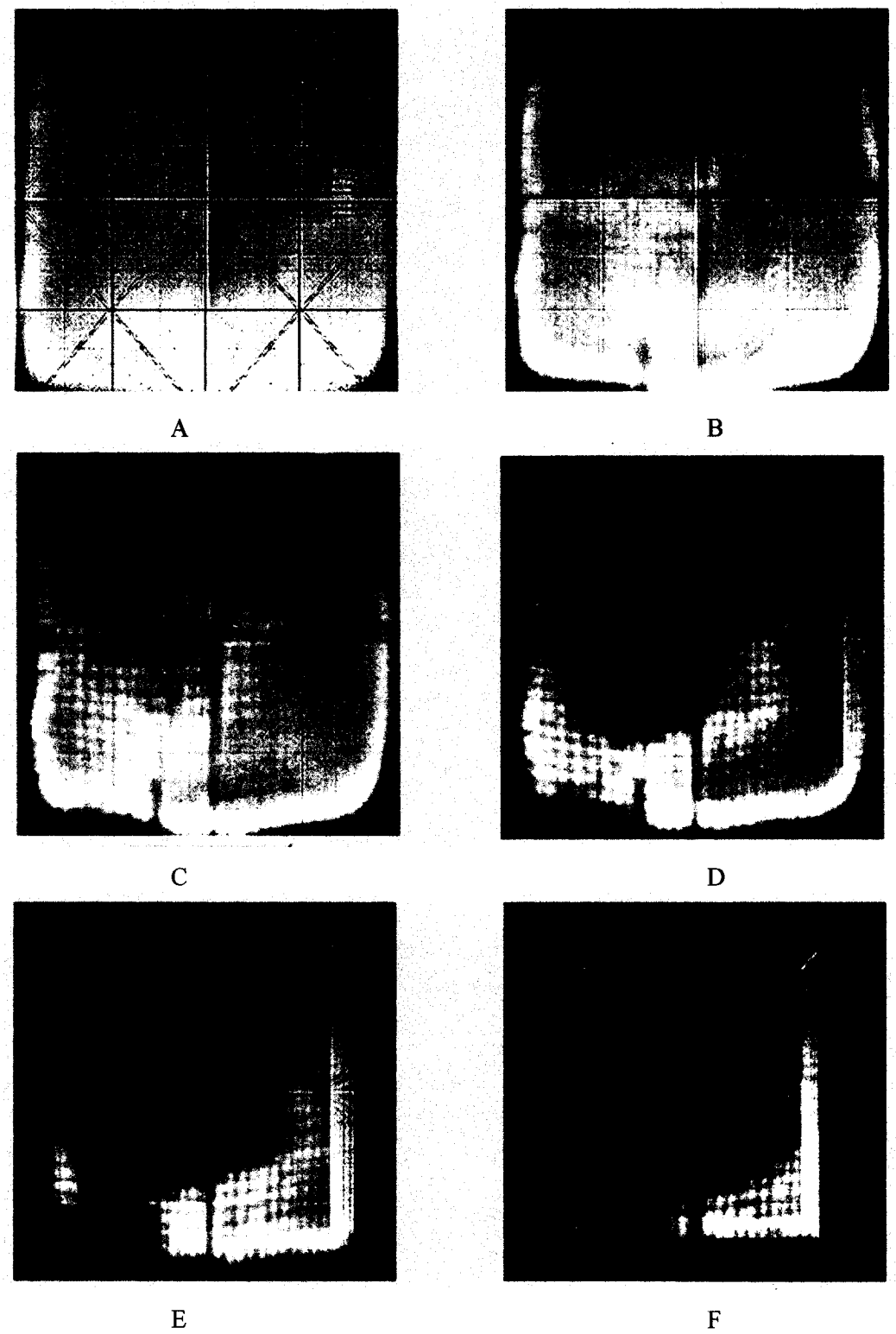

Fig. 6.5. These irradiation images from our PEM-I system were generated with different energy windows. The banded energy windows are from (32 - 63) (image A), (64 - 95) (B), (96 - 127) (C), (128 - 159) (D), (160 - 191) (E), and (192 - 223) (F).

As indicated in (6.2) and (6.3), there is no correlation between Xp and Yp. So the principle of the energy non-uniformity can be demonstrated by analyzing image in one-direction (X-axis).

Considering an 8-bit ADC digitization system, we have:

$$Ex = XA + XB \tag{6.5}$$

where:

$$0 \le XA \le 255 \tag{6.6}$$

$$0 \le XB \le 255 \tag{6.7}$$

$$0 \le Ex \le 511 \tag{6.8}$$

From (6.2), we have image X-axis address Xp. The position Xp vs. Energy Ex probability function is:

$$0 \le Xp \le 255 \qquad \text{if } 0 \le Ex \le 255 \tag{6.9}$$

$$256 - \frac{655365}{Ex} \le Xp \le \frac{65536}{Ex} \qquad \text{if } 256 \le Ex \le 511 \tag{6.10}$$

Fig. 6.6 plots the Xp probability function. The dark area in the graph demonstrates the possible recorded region in the image X-axis.

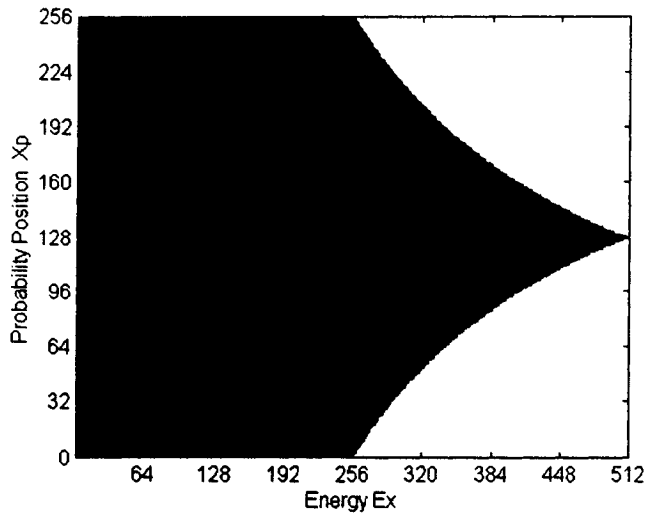

Fig. 6.6. This plots the function of probability position Xp vs. energy Ex.

For instance, we take a photon interaction with an energy Ex of 384. The event could only be recorded if its interaction occurs in such a place that its Xp (calculated from (6.2))

is between 86 to 170; the event that occurs in the regions from 1 to 85 or 171 to 255 will not be recorded.

In general, a "n" bit (such as 10 or 12 bit) digitization system has a Xp vs. Ex probability function of:

$$0 \le Xp < 2^n \qquad \text{if} \qquad 0 \le Ex < 2^n \tag{6.11}$$

$$2^n - \frac{2^{2n}}{Ex} \le Xp \le \frac{2^{2n}}{Ex} \qquad \text{if } 2^n \le Ex < 2^{n+1} \tag{6.12}$$

In Fig. 6.7, S1, S2, and S3 are three possible Ex spectra from the different X^- and X^+ gain adjustments. The gain in S1 is obviously too low. Low X^-, X^+ would cause more imaging artifacts (due to truncation and round-off error); moreover, the amplitudes of X^-, X^+ do not match the ADC input dynamic range, resulting in a lower SNR.

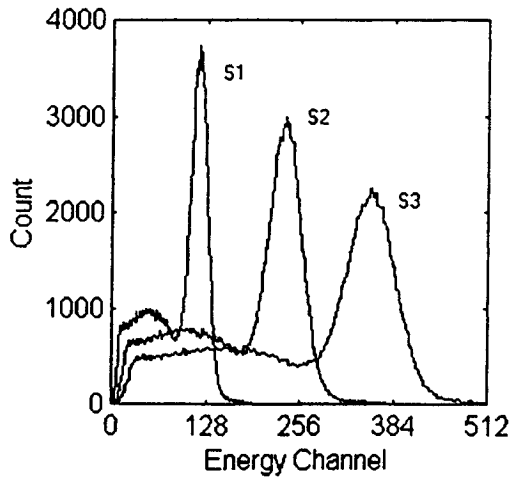

Fig. 6.7. This demonstrates three spectra with different position readout gains.

In case of S3, which is from higher X^-, X^+ gains, we could obtain an image with less digitized artifacts. We also might fully use an ADC dynamic range to achieve a higher SNR. However, an energy non-uniformity artifact will be inevitably created in the irradiation images - the peripheral regions of the irradiation images can only be accumulated from those lower energy (scatter) events.

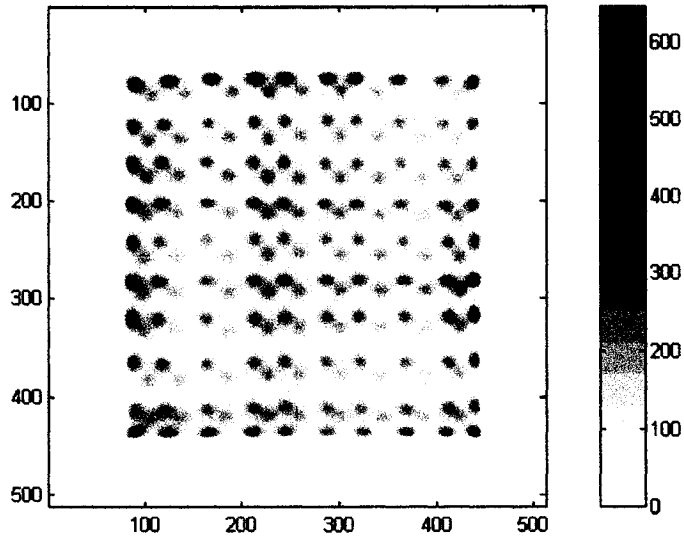

Fig. 6.8. This is an irradiation image from irradiating a BGO crystal with a ^{68}Ge source.

Based on Fig. 6.6 and the position vs. Energy probability function (6.9) and (6.10), we can optimize the gain adjustment. For example, the irradiation image in Fig. 6.8 is within the region of 40 to 216 in X-axis. By looking up at the function graph in Fig. 6.6, we can optimize the gain of X^- and X^+ in such a way that the photopeak region in Ex spectrum is restricted in 300, which is shown as S2 in Fig. 6.7.

6.4 Gain Balanced Adjustment

The DC offset in (X^-, X^+, Y^-, Y^+) can shift the irradiation image off-center; however, we need to be aware that unbalanced X^- and X^+ (Y^- and Y^+) can also result in image shifting. Fig. 6.9 and Fig. 6.10 show the crystal irradiation images resulting from the same experiment condition but only in different gain setting - the gain of X^- in Fig. 6.10 is 1.5 times of that in Fig. 6.9. Due to the unbalanced amplifier gains in the X^- and X^+, the image in Fig. 6.10 shifts to the left in X-axis. This image off-center is more clearly displayed in the image profiles (Fig. 6.11).

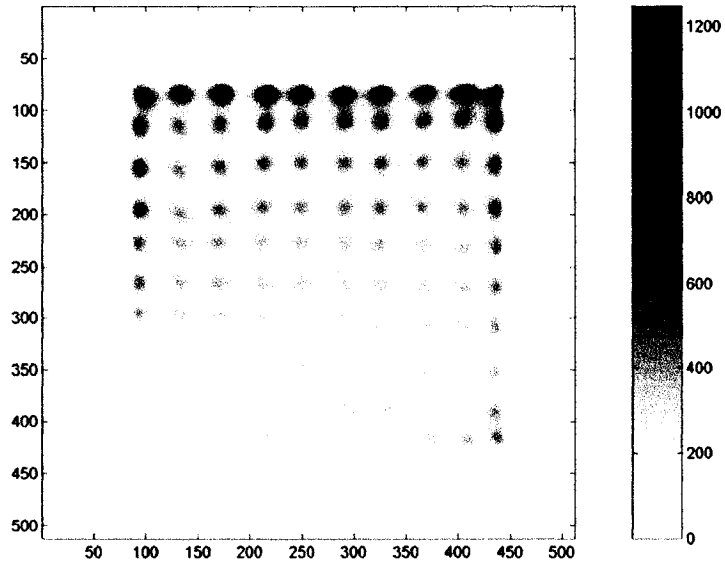

Fig. 6.9. This is a BGO crystal irradiation image with balanced gains.

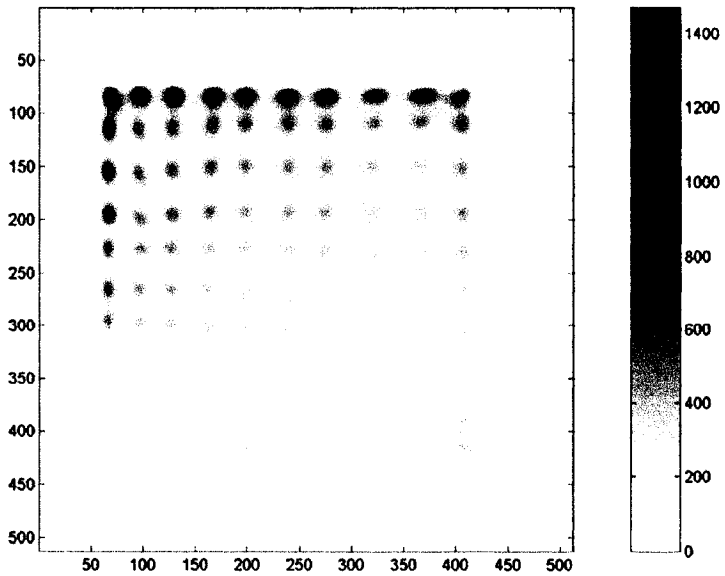

Fig. 6.10. Comparing this irradiation image with Fig. 6.9, the only experiment setup different is that the gain of X^- is 1.5 times of Fig. 6.9.

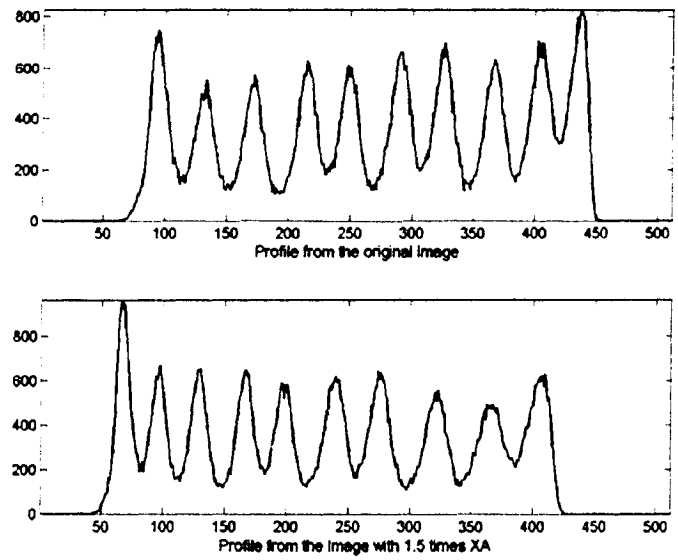

Fig. 6.11. These are the corresponding image profiles of the irradiation images in Fig. 6.9 and Fig. 6.10, respectively.

Supposing we have a balanced X^- and X^+ analog readout circuit. The position BX can be calculated from:

$$BX = 128 \times \left(1 + \frac{X^+ - X^-}{X^+ + X^-}\right) \tag{6.13}$$

In case of unbalanced gains in X^- and X^+, the position UX is:

$$UX = 128 \times \left(1 + \frac{X^+ \times dB - X^- \times dA}{X^+ \times dB + X^- \times dA}\right) \tag{6.14}$$

where dA and dB is the gain factor of X^- and X^+, respectively.

The function of UX vs. BX is shown in Fig. 6.12. As can be seen, the unbalanced gain will cause crystal element to display a non-linearity in the irradiation images. For example, if $dA > 1$, the separations of the crystal "spots" in the image are decreasing where the crystal image is near the lower end of the X-axis. This could make it difficult to identify these peripheral crystal elements.

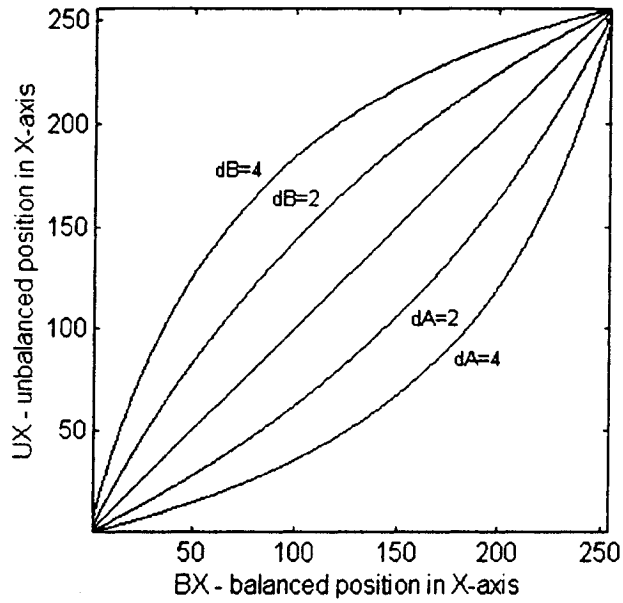

Fig. 6.12. This shows the function of unbalanced UX vs. BX with different gain setting.

6.5 Discussion

In order to achieve higher signal-to-noise ratio, we tend to enlarge the gain of X^-, X^+, Y^-, Y^+ to fully match the ADC dynamic range. We demonstrate that it could cause an energy non-uniformity error if the gains are improperly adjusted. As a result, N bit ADCs could possibly only function as N-1 bit in the position readout circuits. We demonstrate that an 8-bit analog to digital converter (ADC) is probably insufficient in the position recording if a gamma-ray event position is calculated from digitized X^-, X^+, Y^-, Y^+ signals. With many fast 10, 12 bit ADCs available nowadays, we will achieve better results by updating higher bit ADCs.

CHAPTER VII

DETECTOR EVALUATION AND RESULTS

7.1 Image Spectrum and Histogram Analysis

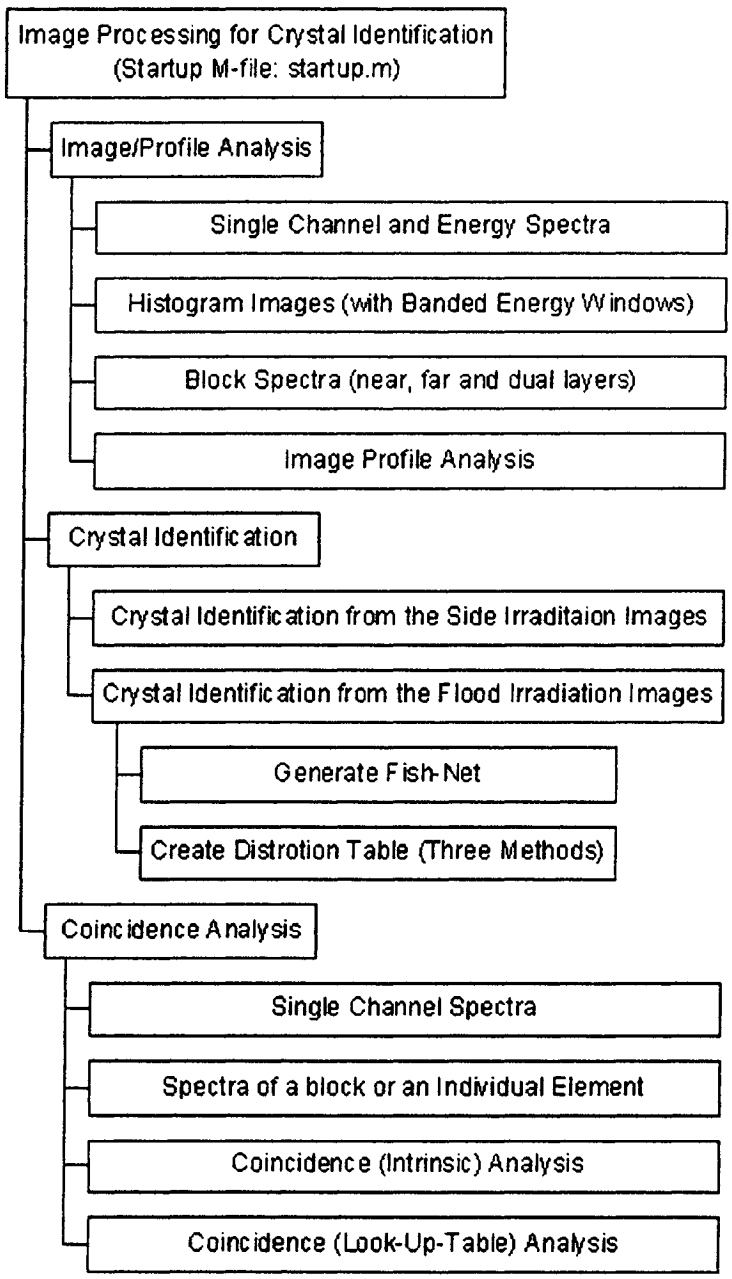

Fig. 7.1. The tree structure of the MATLAB program for spectrum, histogram, and coincidence analysis.

Fig. 7.1 shows the "tree" structure of the "*Imgproc*" software, which was written to analyze PEM-II detector energy spectra, irradiation intensity images (2D histogram), and coincidence images. The detailed description of the source code can be found in Appendix D.

The software was programmed with MATLAB [160], which includes following three main functions.

Spectrum and histogram analysis

This function exhibits and analyzes spectrum of each front-end channel (digitized XA, XB, YC, YD), energy spectrum of crystal block (summed XA, XB, YC, YD), energy spectra of both near and far layer from side-irradiation images, energy spectra from the flood-irradiation images.

The irradiation intensity images (2D histogram) are analyzed with a banded-energy-window technique [128]. The "spline" function from MATLAB Spline toolbox [161] was applied to examine the image profiles.

Crystal identification investigation

We investigated two different crystal identification methods, which include crystal identification from side-irradiation images and from flood-irradiation images. The identification from side-irradiation method is an update version of previously developed software by J. Robar that identifies the crystal elements from the near layer side-irradiation images [128].

Three distortion look-up-table (LUT) generation methods were tested in the irradiation image process. These methods were evaluated from the coincidence experiments. Detailed experiments are illustrated in 7.4.3.

Coincidence image processing

After LUT generation, the spectrum of a single crystal element can be analyzed. Coincidence back-projection images with different LUTs were evaluated in this function. Detailed results are shown in 7.4.

7.2 Crystal Irradiation Experiments

Fig. 7.2 shows a mold for side irradiation experiments. The mold was built with a milling machine in the Machine Workshop of the Physics Department. After wrapping two layers of Teflon tape on the BGO crystal and the R7600-C12 PS-PMT, we can insert the crystal and the PMT into the mold precisely.

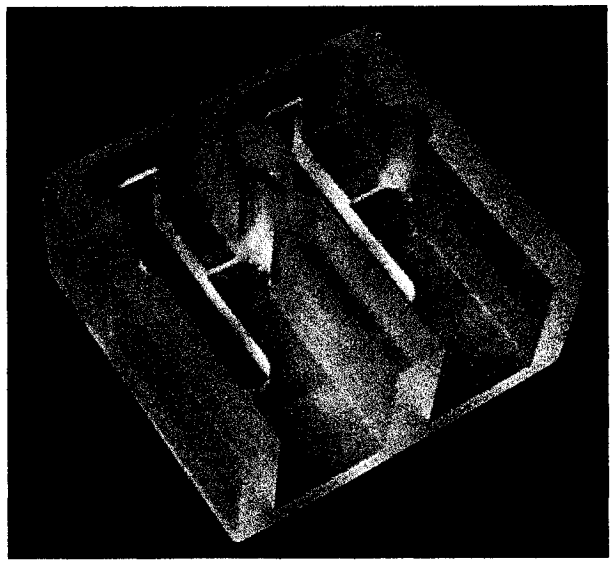

Fig. 7.2. Plastic mold for side-irradiation and flood-irradiation experiments.

7.2.1 Side-Irradiation Spectrum Analysis

The crystal identification images (Fig. 7.3-A) were acquired by irradiating the crystal near layer with a collimated ^{68}Ge source. An intensity profile (Fig. 7.3 - C) along the horizontal spline (Fig. 7.3-A) shows clear separation of the crystal elements. Fig. 7.3-B shows the image of the far layer with the same irradiation setup. Fig. 7.3-D displays the profile along the horizontal spline (Fig. 7.3-B). All crystal elements 10 × 10 in the near layer, and 9 × 9 in the far layer can be identified. The average peak to valley ratio of near layer is 4.3. It is 2.1 for the far layer.

Fig. 7.4 shows the summed energy spectra of crystal block's proximal (near) and distal (far) layers from side-irradiation, as well as the dual layers from flood irradiation with a ^{68}Ge source. The spectra of two crystal elements, one from the proximal layer (circle in Fig. 7.3-A) and the other from the distal layer (in Fig. 7.3-B) are shown in Fig. 7.5. The

relative energy resolution of the proximal layer element (FWHM/Peak) is about 27%. The relative energy resolution of the distal layer element is about 29%.

In order to specify the spectra differences related to the proximal or distal layer in which the photon interaction occurred, the amplifier gains and PMT high voltages setting were kept the same during these experiments.

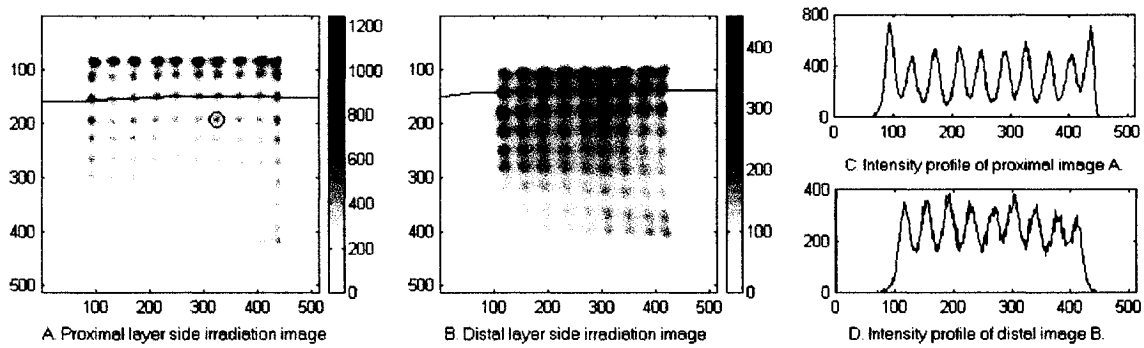

Fig. 7.3. These are BGO crystal side irradiation raw images and corresponding intensity profiles. The side irradiation is entering from the top of the image A and B. The near 2D image (A) shows that 10×10 crystal elements can be clearly identified. The far 2D image (B) shows that 9×9 crystal elements can be identified. The intensity profile (C) is from the horizontal spline in the near image (A). The lower intensity profile (D) is from the horizontal spline in the far image (B).

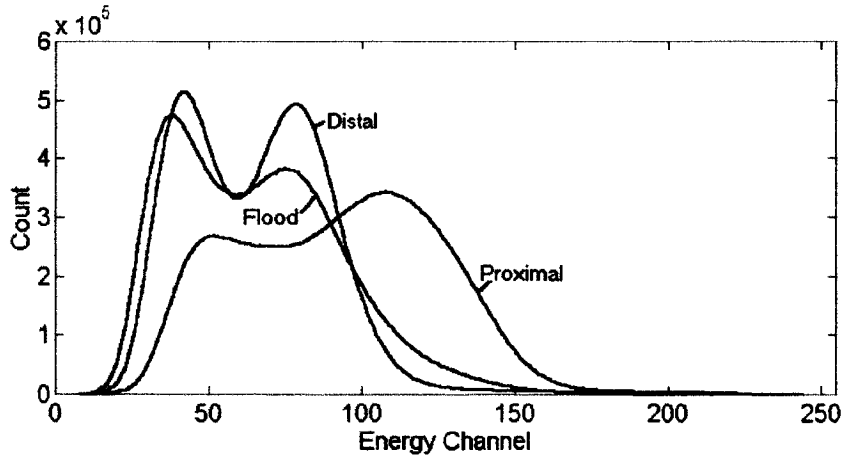

Fig. 7.4. These are the summed energy spectra over the entire near and far layer crystals (side irradiation) and all dual layer crystals (front flood irradiation) with a ^{68}Ge source.

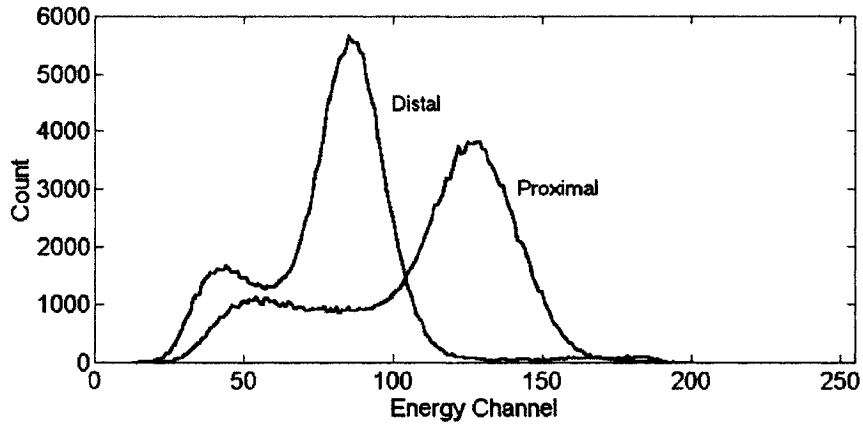

Fig. 7.5. These are the energy spectra resulting from irradiating the proximal and distal layers for the two individual crystal elements with a ^{68}Ge source.

7.2.2 Crystal Performance Evaluation

Side Irradiation Experiments

A side irradiation method was applied to evaluate the performance of position and timing circuits. Fig. 7.6 illustrates the side irradiation setup. A ^{68}Ge or ^{137}Cs source was collimated by two lead bricks to irradiate only the near or far elements of the BGO crystal block for side irradiation experiments.

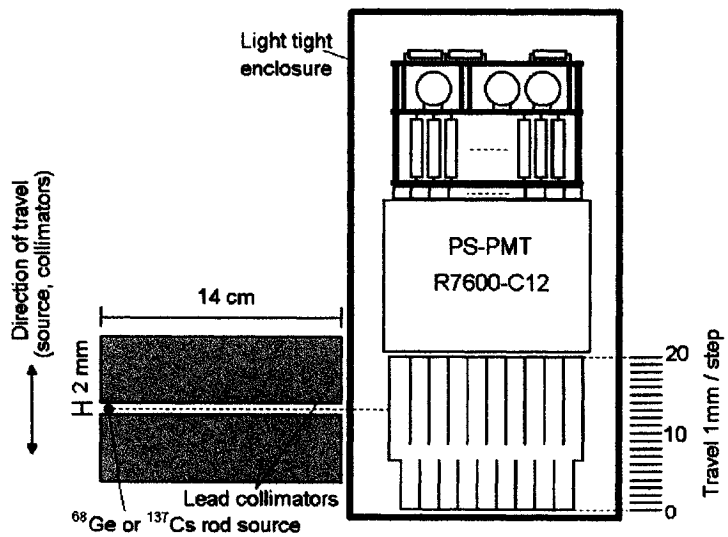

Fig. 7.6. A 68Ge or a 137Cs source was collimated by two lead bricks, mounted on a translation stage, to irradiate along the side of the BGO crystal block for side irradiation experiments.

List mode data with 12 bits digitized (X^-, X^+, Y^-, and Y^+) were acquired to generate 2D images of the crystal arrays and energy spectra for crystal performance evaluation.

Fig. 7.7 shows the side-irradiation intensity images moving from step 0 (0 mm marked in Fig. 7.6) to step 21 (21 mm from the beginning). The images were acquired based on the same total counts during the experiments.

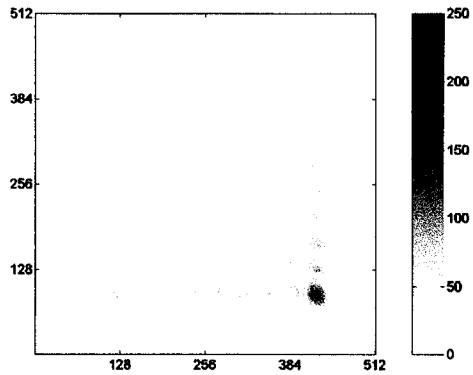

0 mm

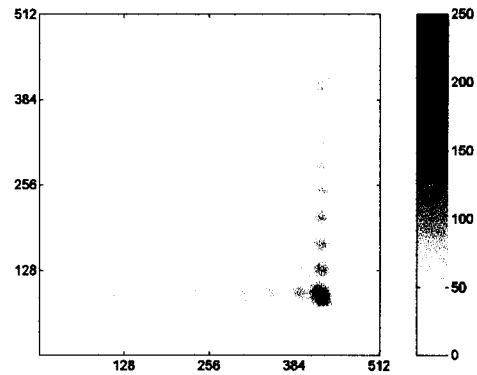

1 mm

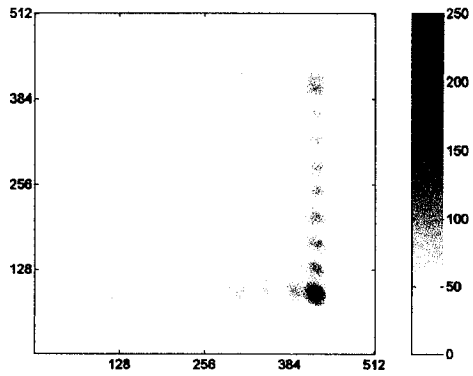

2 mm

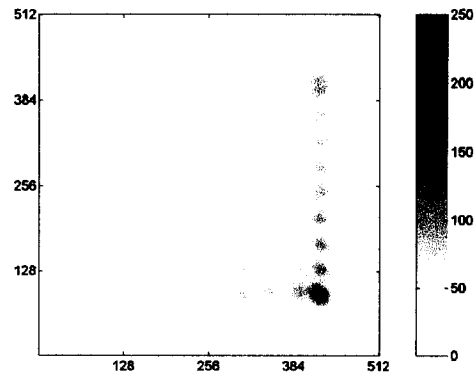

3 mm

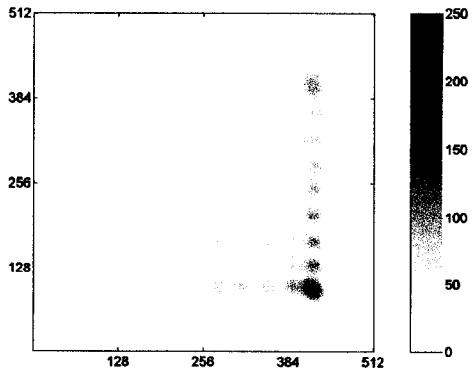

4 mm

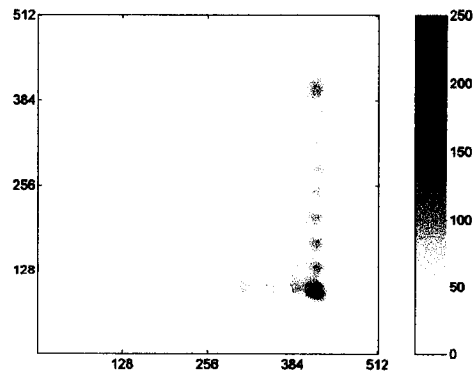

5 mm

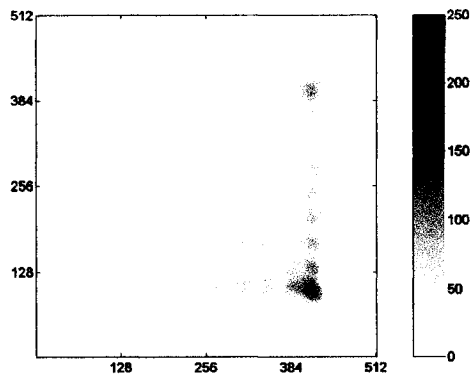

6 mm

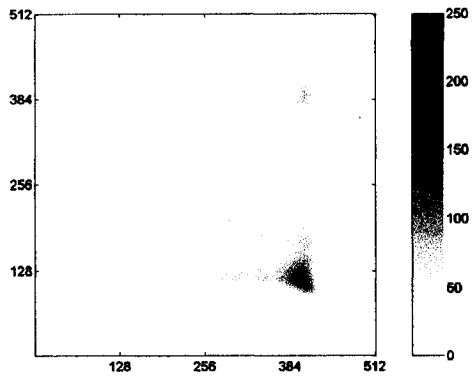

7 mm

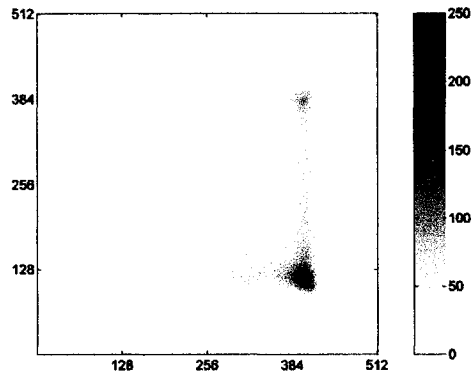

8 mm

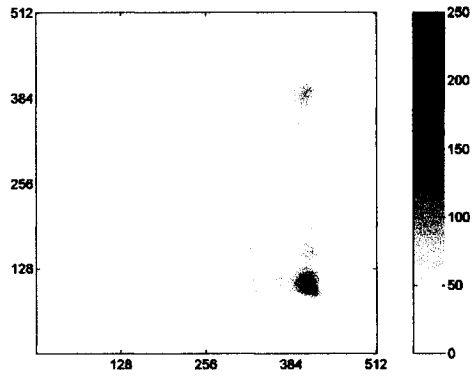

9 mm

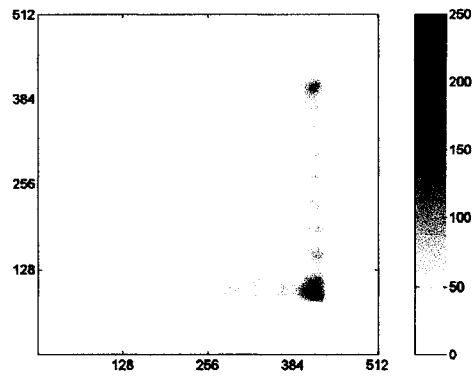

10 mm

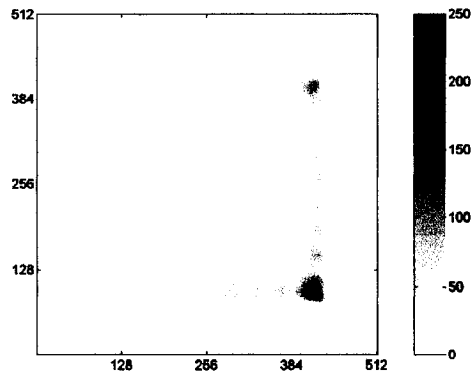

11 mm

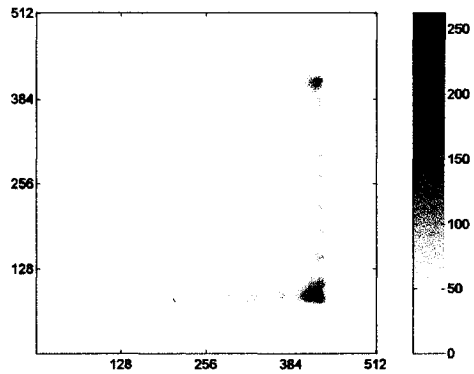

12 mm

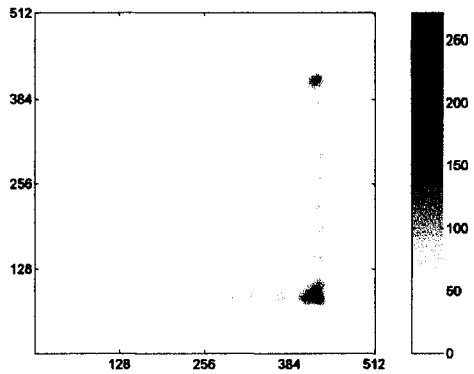

13 mm

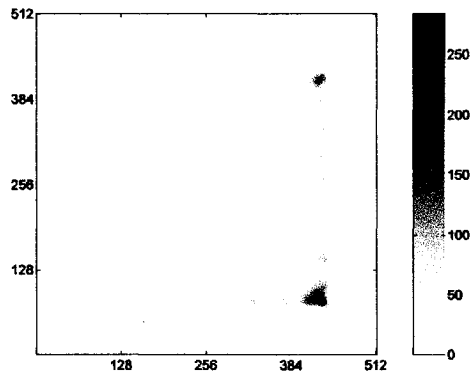

14 mm

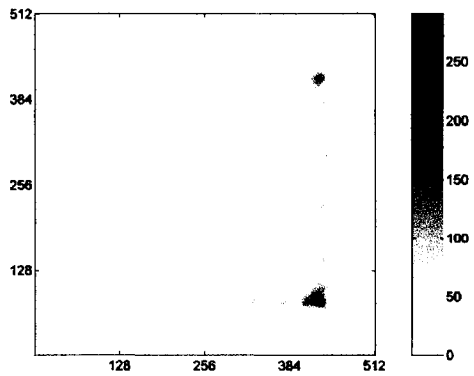

15 mm

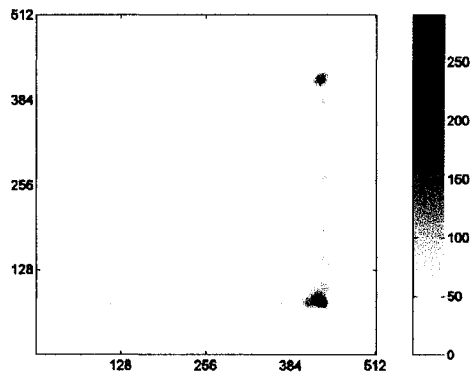

16 mm

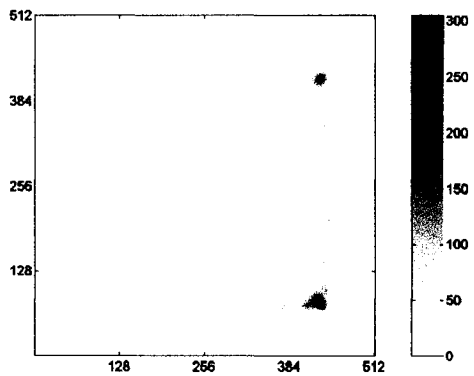

17 mm

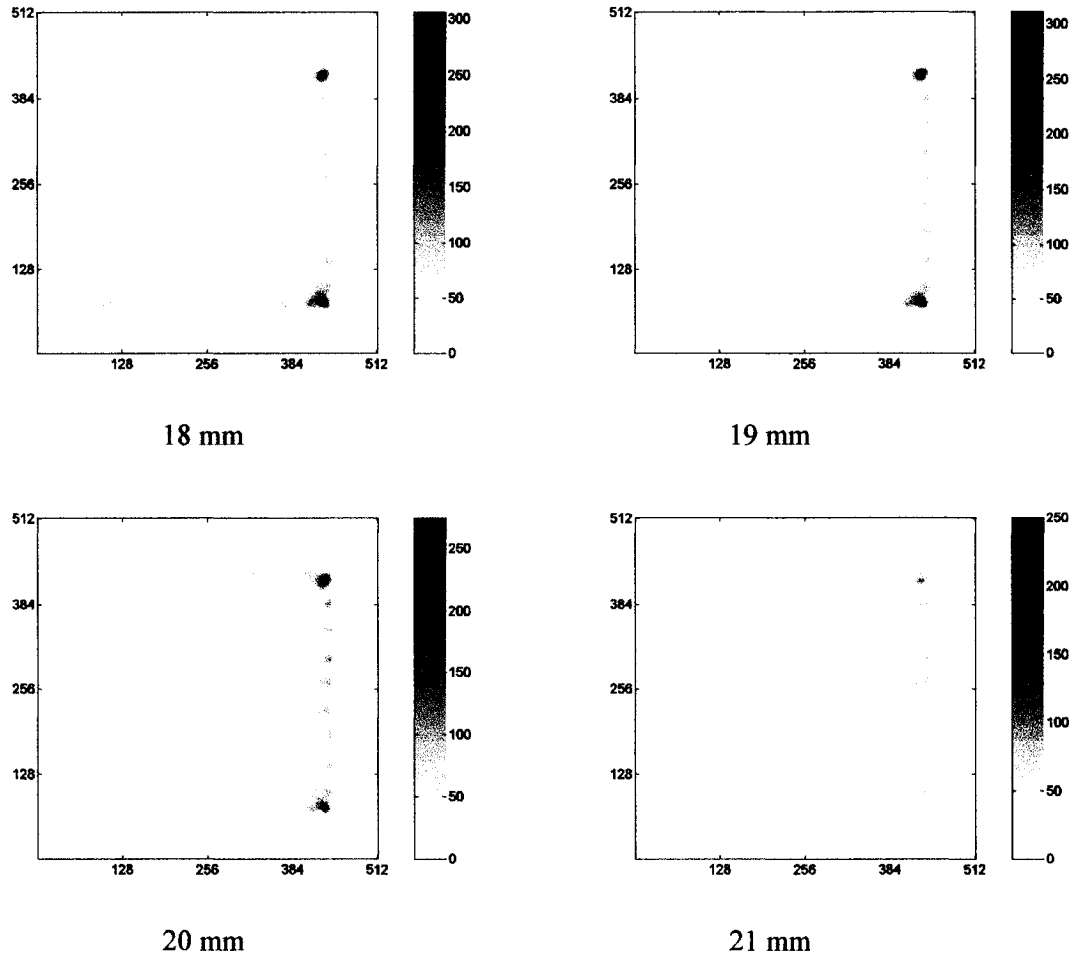

Fig. 7.7. Irradiation images resulting from moving a highly-collimated ^{137}Cs source side irradiating a BGO crystal for crystal performance experiments.

Two artifacts are revealed in the crystal performance evaluation experiments. First, there is an image distortion which is caused by the edge elements of the far layer. The cut crystal block has 10 × 10 elements in the near layer and (1/2 + 9 + 1/2) × (1/2 + 9 + 1/2) elements in the far layer. As can be seen in Fig. 7.7, the edge half-size crystal elements in the far layer could not be identified from the crystal irradiation images; furthermore, these elements were even blurring the image of the edge elements in the near layer. Second, there is an image blurring which is caused by the uncut region connecting the near and far layers. This is shown in the images of "7 mm" and "8 mm" in Fig. 7.7.

We concluded to add two more steps in crystal processing procedures to resolve these two side effects. The first step is to remove all the edge crystal elements of the far layer. This must be done after encapsulating the near layer. The second step is to eliminate the

crystal uncut region. This can be done by cutting the crystal along the uncut-region with a thick diamond saw blade (1-mm thickness). Then we completely eliminated the uncut region and mirror-polished the cut surfaces (specular reflective finish).

Flood Irradiation Experiments

Fig. 7.8 shows an initial result of a crystal identification image from flood irradiation with a ^{68}Ge source. The middle uncut region of the crystal was intact during the experiments.

In this image, the near layer elements can be clearly identified. As shown in Fig. 7.9, the distal elements can be accentuated by applying an energy-banding technique [128]. Because there is a near-far crystal overlap in the flood irradiation images, this will make it difficult to assess the depth of interaction information.

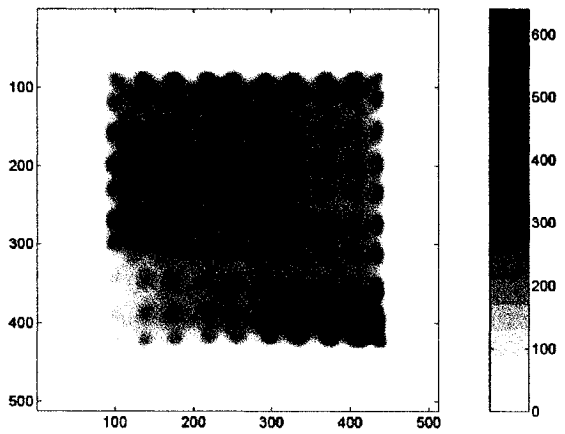

Fig. 7.8. This is the BGO crystal front-flood irradiation image with a ^{68}Ge source. The relative energy threshold (as shown in Fig. 8) is arranged from 62 to 255.

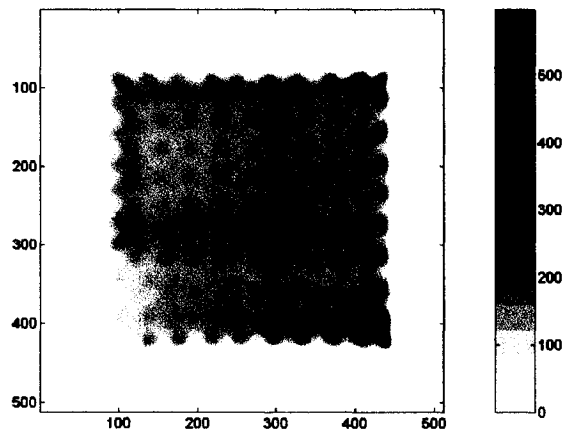

Fig. 7.9. This is the BGO crystal front-flood irradiation image generated from the same list file as Fig. 7.8, but the relative energy threshold is banded from 62 to 94.

The flood irradiation images in Fig. 7.10 and 7.11 were generated from the same BGO crystal. Before the uncut region was removed (Fig. 7.10), the irradiation image had a significant near-far element overlap. After eliminating the interconnecting uncut region (Fig. 7.11), crystal irradiation images clearly shows the crystal elements in the near and far layers, and the image overlaps between the near and far crystal elements were substantially reduced.

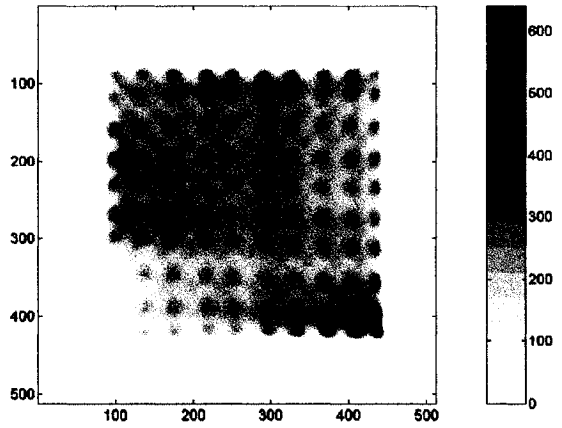

Fig. 7.10 This is a BGO crystal front-flood irradiation image with a ^{68}Ge source. The hardware lower energy threshold is 150 keV.

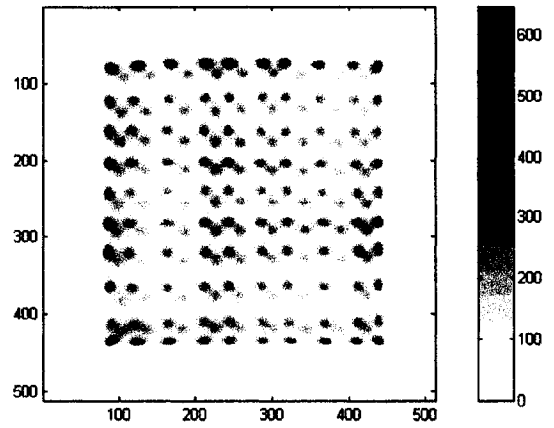

Fig. 7.11. This crystal front-flood irradiation image from a same BGO crystal as in Fig. 7.10, but after removing the uncut region.

7.3 Evaluation Modular Detectors with Dual and Quadra-PMT Schemes

Modular detectors with either dual or quadra-PMTs have been investigated for our PEM-II and animal PET detectors. Timing circuits in the different modular schemes are similar - they are the summing current signal from PMTs last dynode outputs. However, the position readout circuits are different. We designed and tested the front-end electronic circuits for both dual and quadra-PMT schemes in order to determine a suitable pattern for our modular detectors.

7.3.1 Position Readout in the Dual-PMT Scheme

Fig. 7.12 shows the position readout scheme with 1 × 2 PS-PMTs. In the circuit, the small resistors R2 directly connect the crossed anode readout resistor chains of two PMTs in both X and Y directions. The position readout circuit in this scheme is simplified to only four (X^+, X^-, Y^+, Y^-) outputs.

As can be seen from Fig. 7.12, the cross-anode readout resistor chain of PMT-A in X (or Y) direction is serial connected with that of PMT-B. This setup will produce the irradiation image of PMT-B offset with that of PMT-A in both X and Y directions. The

irradiation image with this dual-PMT scheme is shown in Fig. 7.13. The physical location of the crystal elements can be specified by adjusting the image distortion look-up-table.

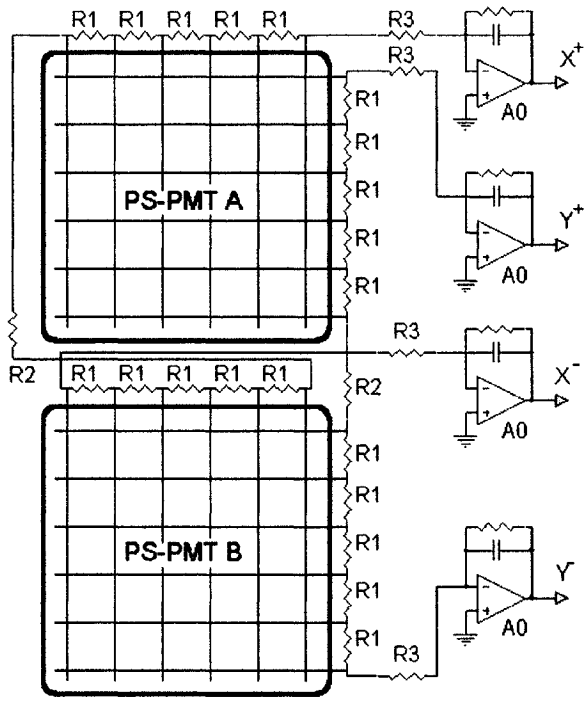

Fig. 7.12. Two PS-PMTs are combined together to build up a group for simplifying the front end analog circuits. All the R1 resistors are 100Ω, R2 are 20Ω and R3 are 70Ω.

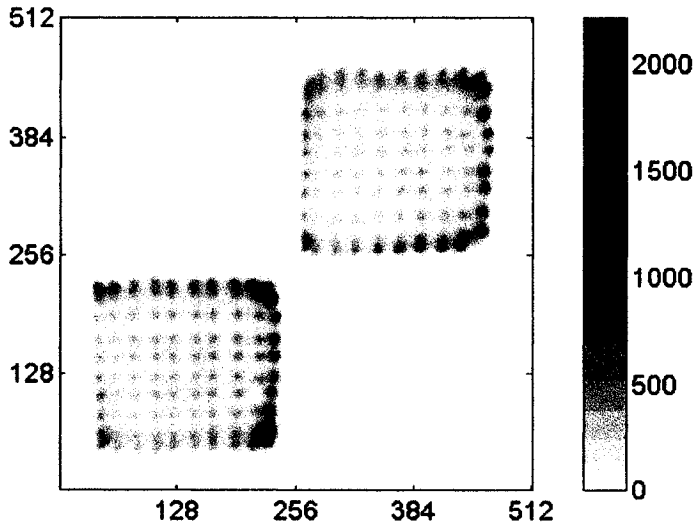

Fig. 7.13. The side-irradiation image from the modular detector with dual-PMT scheme

7.3.2 Position Readout in the Quadra-PMT Scheme

The schematic of the position readout electronic circuits with 2 x 2 PS-PMT scheme is shown in Fig. 7.14. Only the integrator circuits that integrate the current signals from the anode into voltage outputs ($-X_{AB}$, $+X_{AB}$, $-X_{CD}$, $+X_{CD}$, $-Y_{AC}$, $+Y_{AC}$, $-Y_{BD}$, $+Y_{BD}$) are shown in the schematic.

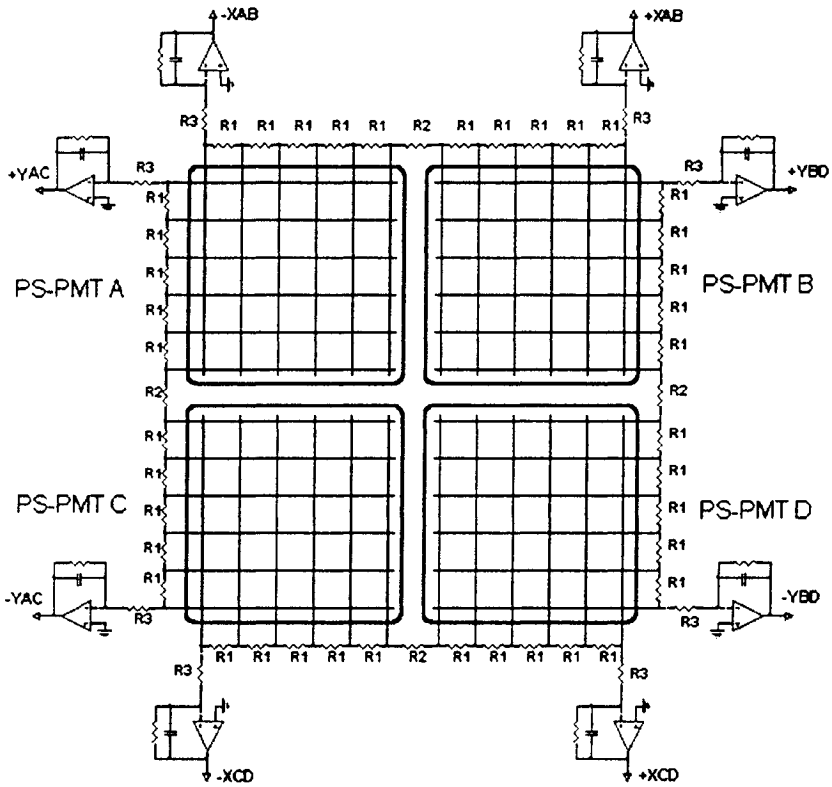

Fig. 7.14. This is the schematic of the modular detector design with 4 x 4 PS-PMT schemes. The resistor values of R1 are 100Ω, R2 are 20Ω and R3 are 70Ω. Only the integrators are shown in the schematic.

One proposal is to sum the integrator outputs so that the final position readouts have only four (X^+, X^-, Y^+, Y^-) outputs. The summing circuits will perform:

$$X^+ = (+X_{AB}) + (+X_{CD}) \tag{7.1}$$

$$X^- = (-X_{AB}) + (-X_{CD}) \tag{7.2}$$

$$Y^+ = (+Y_{AC}) + (+Y_{BD}) \tag{7.3}$$

$$Y^- = (-Y_{AC}) + (-Y_{BD}) \tag{7.4}$$

Fig. 7.15 shows the side-irradiation image with 2 x 2 PMT scheme. Only the near layer crystals were side-irradiated and shown in the image.

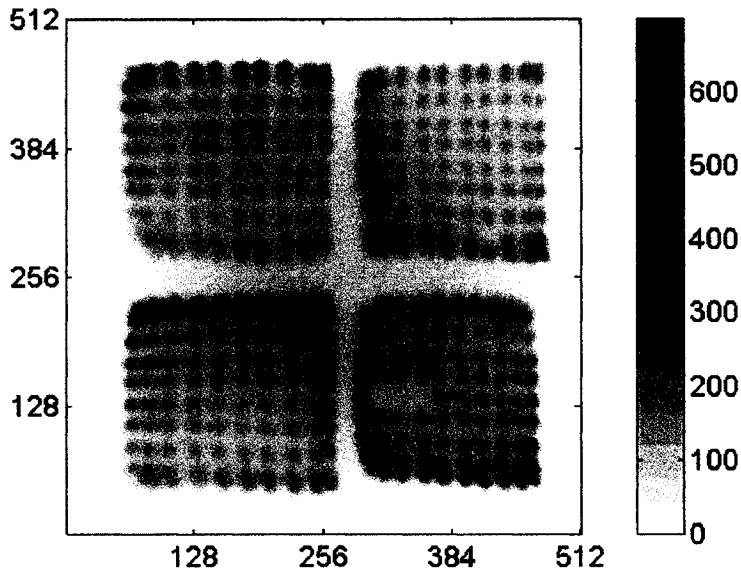

Fig. 7.15. The side irradiation image from a modular detector with quadra PS-PMT schemes. The three elements missing in the right-bottom corner is due to the real broken crystal elements.

Another proposal is that all eight positioning output signals were integrated, then digitized by analog-to-digital converter (ADC) circuits. These circuits are all placed near the detector housing. Only digital signals will be buffered and transfer to main processing board, which could by placed far from the detector gantry.

The following equations were applied to locate the event's PS-PMT:

$$\textit{PS-PMT A}, \quad \text{if } [E(X_{AB})>E(X_{CD})]\&\ [E(Y_{AC})>E(Y_{BD})] \tag{7.5}$$

$$\textit{PS-PMT B}, \quad \text{if } [E(X_{AB})>E(X_{CD})]\&\ [E(Y_{AC})<E(Y_{BD})] \tag{7.6}$$

$$\textit{PS-PMT C}, \quad \text{if } [E(X_{AB})<E(X_{CD})]\&\ [E(Y_{AC})>E(Y_{BD})] \tag{7.7}$$

$$\textit{PS-PMT D}, \quad \text{if } [E(X_{AB})<E(X_{CD})]\&\ [E(Y_{AC})<E(Y_{BD})] \tag{7.8}$$

where $E(X_{AB})$ is the sum result of digitized $(+X_{AB})$ and $(-X_{AB})$; $E(X_{CD})$ is sum of digitized $(+X_{CD})$ and $(-X_{CD})$; $E(Y_{AC})$ is sum of digitized $(+Y_{AC})$ and $(-Y_{AC})$; $E(Y_{BD})$ is sum of digitized $(+Y_{BD})$ and $(-Y_{BD})$.

The summing and comparison calculations could be performed by simply using CPLD in pipeline processing mode, or can be done by software calculations.

7.4 Spatial Resolution Measurements

7.4.1 Distortion Look-Up-Table Generation

A gamma ray interaction is located from a crystal element. The crystal distortion look-up-table (LUT) converts the addresses (X, Y) of the gamma ray event into the array (row, column) of the crystal element.

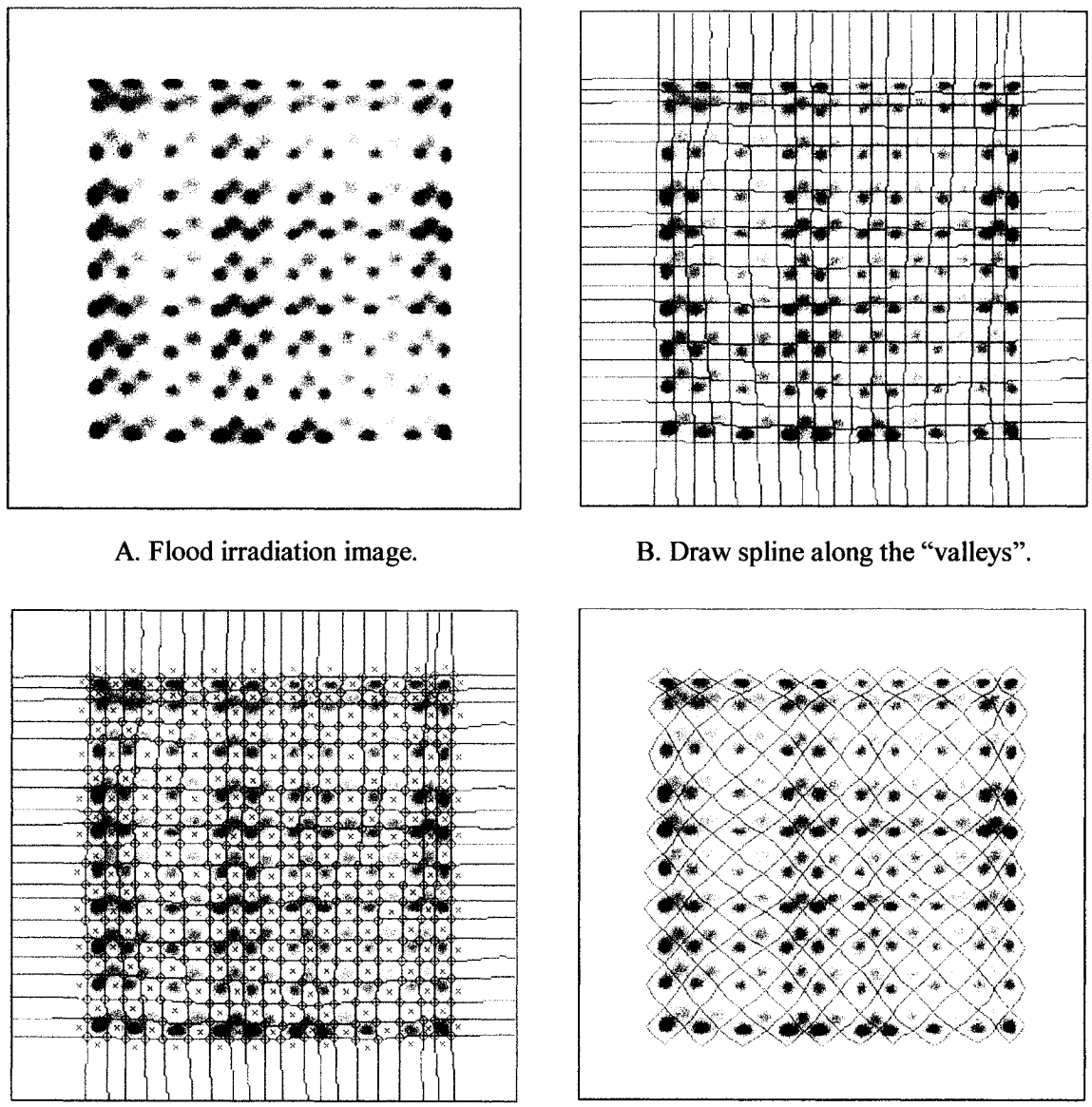

A. Flood irradiation image.

B. Draw spline along the "valleys".

C. Mark cross points in the center of "valleys".

D. Generate look-up-table.

Fig. 7.16. Crystal look-up-table generation.

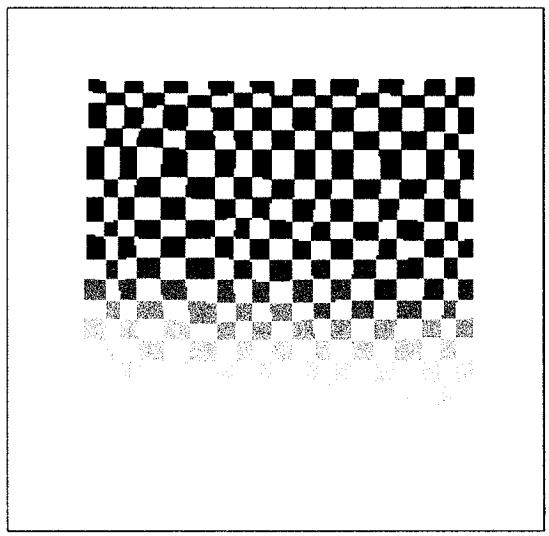

Mode-A. Generate LUT only counts the "peak" regions.

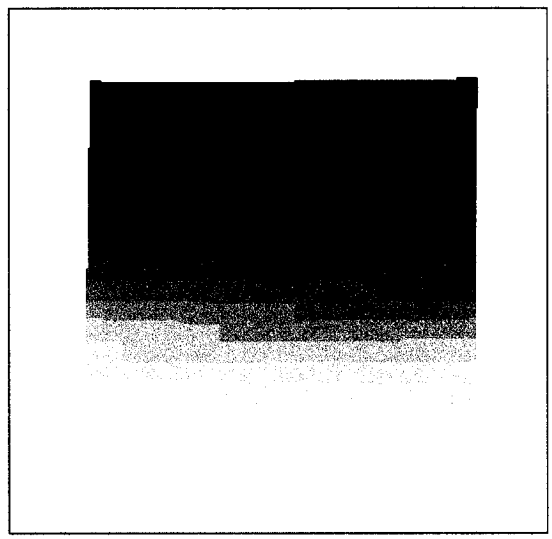

Mode-B. Generate LUT counts both the "peak" and the "valley" regions.

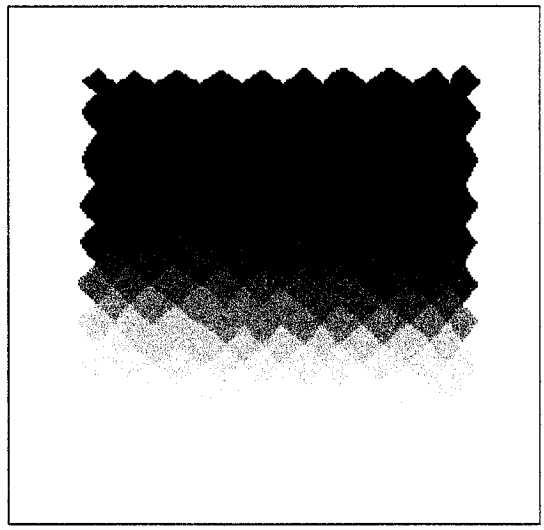

Mode-C. Generate LUT with "fish-net" pattern.

Fig. 7.17. Three modes LUTs for trials - A. LUT only counts the "peak" locations; B. LUT counts the "peaks" and "valleys", but they are assumed in different locations; C. LUT is generated in "fish-net" mode. The gray scale represents the element ID numbers (element 1, element 2, ... etc.). Each region of an crystal element has on gray degree (1, 2, 3, ...).

In Mode-A, the crystal element ID numbers are from 1 (the left-bottom corner crystal element), 2 (next to 1 in the bottom row), 3, ... to 181 (the right-upper corner crystal element). The Mode-A LUT image is scaled from 1(the lightest) to 181 (the darkest). As only the "hot-spots" were selected in the LUT1 methods, the valley regions were assigned as "0".

Similarly, in Mode-B, the crystal element ID numbers are from 1 (the left-bottom element) to 361 (the right-upper element). The Mode-B LUT image is scaled from 1 (the lightest) to 361 (the darkest). In fish-net Mode-C, the crystal element ID numbers are from 1 to 181. The Mode-C LUT image is scaled from 1 to 181.

Three different modes of LUTs have been tested for our new detectors. Fig. 7.16 shows the procedures to generate LUTs. First, we acquire flood-irradiation list mode data and create 2D irradiation intensity image (Fig. 7.16 - A). The crystal elements exhibit as "peak" regions in the image. Then we draw spline along the "valleys" of these "peak" regions (Fig. 7.16 - B) with MATLAB spline function in MATLAB Spline Toolbox [161]. Next, we calculate the central position of the "valleys" ("x" marks in Fig. 7.16 - C) and locate the spline crosses ("o" marks in Fig. 7.16 - C). Finally, we can generate different mode LUTs. Fig. 7.16 - D shows the "fish-net" mode LUT.

Three different modes LUTs are shown in Fig. 7.17. Mode-A only counts the "peak" regions. This method can more accurately locate the crystal elements compared with mode B and C; however, it will be less efficient since the events that located in the "valley" regions will not be counted. Mode A and C locate total (10 × 10) + (9 × 9) elements. Mode B locates (19 × 19) elements - the peaks and valleys in mode B are considered as different elements.

7.4.2 Crystal and PMT Setup for Coincidence Experiments

Coincidence experiments are setup by aligning two prototype detectors facing each other 10 cm apart. Two ^{68}Ge point sources (0.75 mm diameter) are located in the middle of the two detectors, which are 10 mm apart. Fig. 7.18 and 7.19 illustrate the mold that was built with milling machine in the Machine Workshop of the Physics Department.

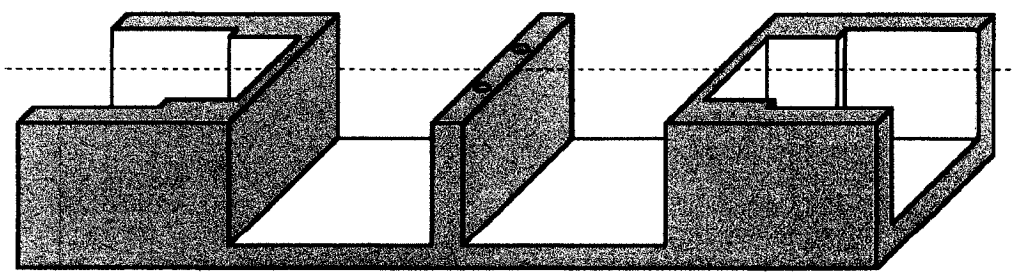

Fig. 7.18. This is the 3D mechanical drawing of the mold built for coincidence experiments.

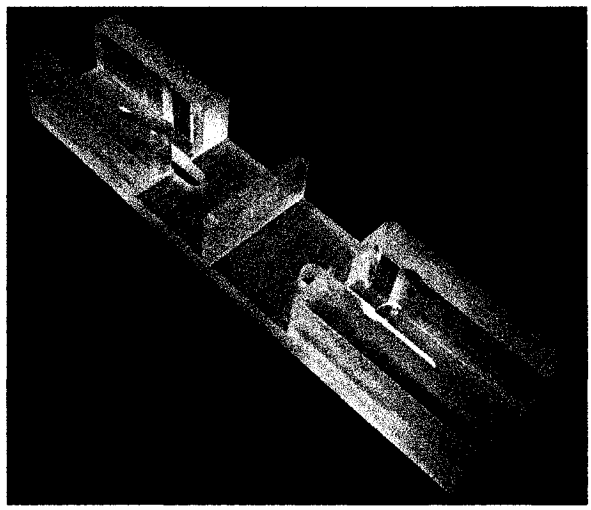

Fig. 7.19. The plastic mold built by milling machine for coincidence experiments.

7.4.3 Spatial Resolution Based on Different Distortion Look-Up-Tables

Fig. 7.20 shows the coincidence image that is generated from back-projecting the irradiation images from two opposite detectors. The coincidence image was created from the 256 × 256 irradiation images, without looking up distortion LUT. The high-voltage of the PS-PMTs was negative 850 volt; lower energy threshold (hardware) was about 150 keV. The 3D-coincidence image displayed in Fig. 7.21. The image profile illustrated in Fig. 7.22, which shows the intrinsic image resolution of full width of half maximum (FWHM) about 1.8 mm.

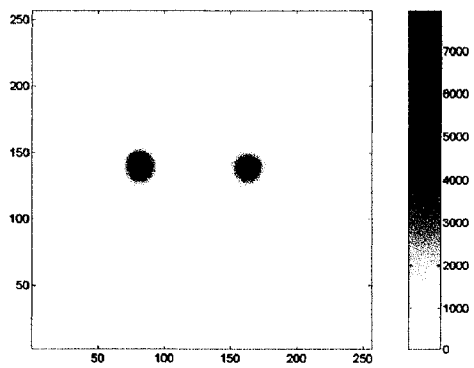

Fig. 7.20. This is image coincidence image resulting from the experiment shown in Fig. 7.17.

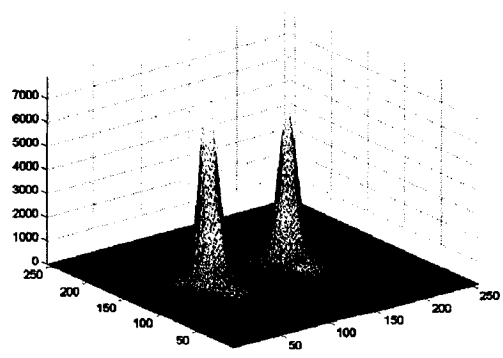

Fig. 7.21. This is 3D display of the coincidence image Fig. 7.18.

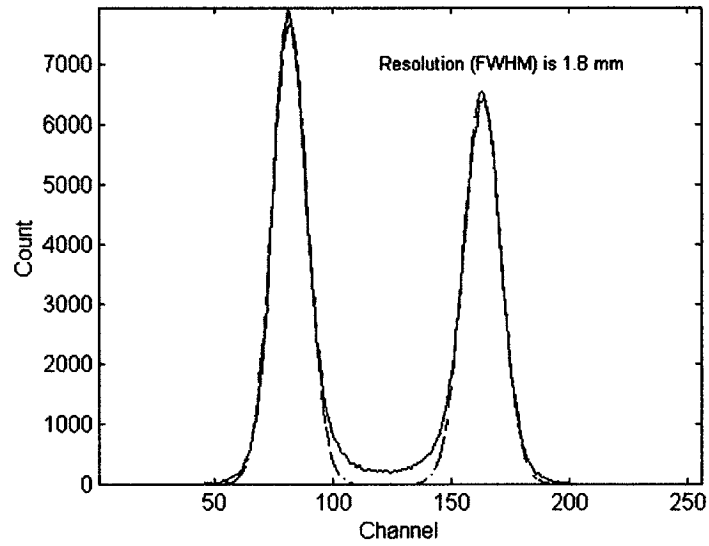

Fig. 7.22. The solid line of the plots is the image (Fig. 7.18) profile. The dash line is the Gaussian fitting result. The full width of half maximum (FWHM) measurement is calculated from the standard deviation of the Gaussian fitting curves.

Fig. 7.23 shows the coincidence image that was created after applying LUT mode-A. Even though an irradiation intensity image has a matrix of 256 × 256 pixels, after looking up distortion table, a gamma-ray event only falls in a matrix of 10 × 10 in the near layer and 9 × 9 in the far layer. So the coincidence image should be created in the image with 19 × 19 bins. The spatial resolution with mode-A LUT is 1.86 mm, which is close to the intrinsic spatial resolution.

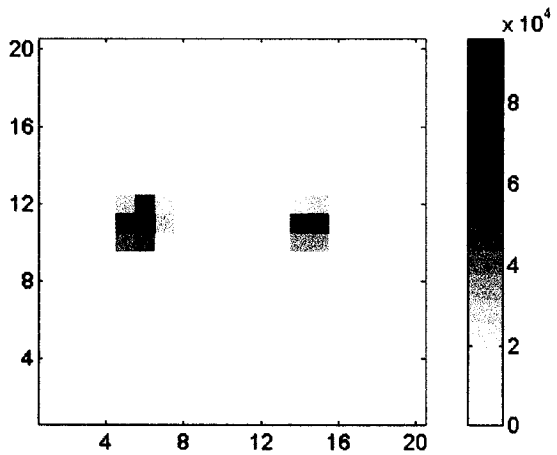

Fig. 7.23. The coincidence image by applying the LUT mode-A.

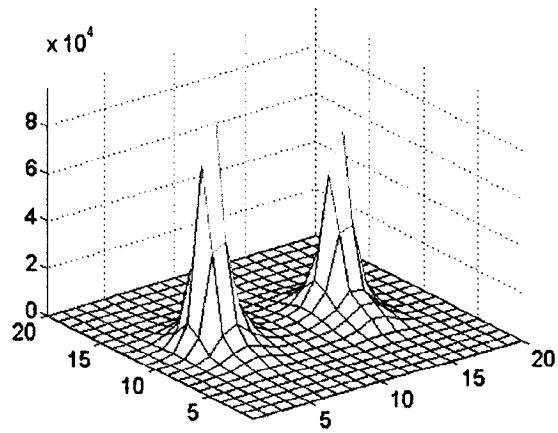

Fig. 7.24. This is 3D display of the coincidence image Fig. 7.23.

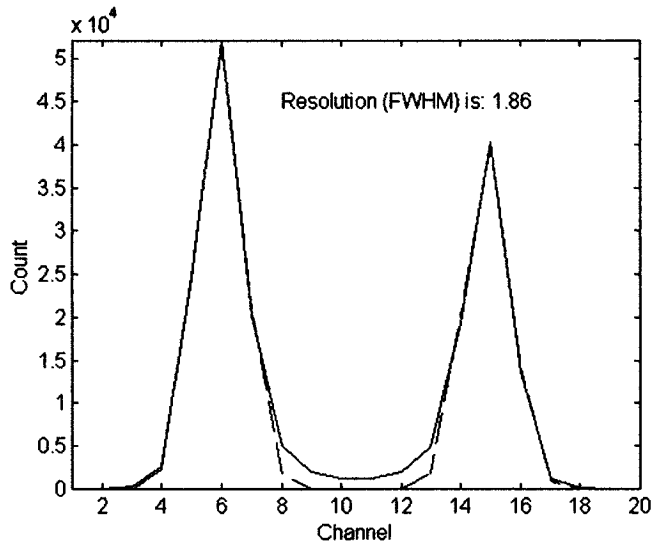

Fig. 7.25. The solid line of the plots is the image (Fig. 7.23) profile. The dash line is the Gaussian fitting result.

The coincidence image by applying the mode-B LUT is displayed in Fig. 7.26. As can be seen in Fig. 7.17, both the "peak" and "valley" regions are counted as "elements". So the coincidence image can be displayed in 38 × 38 bins. Compared with mode-A results (Fig. 7.23 - 7.25), the images are more smooth. The efficiency in mode-B is higher than that in mode-A, but the spatial resolution in mode-B is degraded to 2.04 mm.

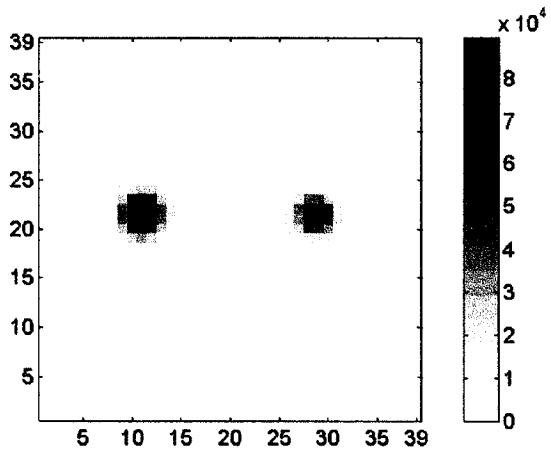

Fig. 7.26. The coincidence image by applying the LUT mode-B.

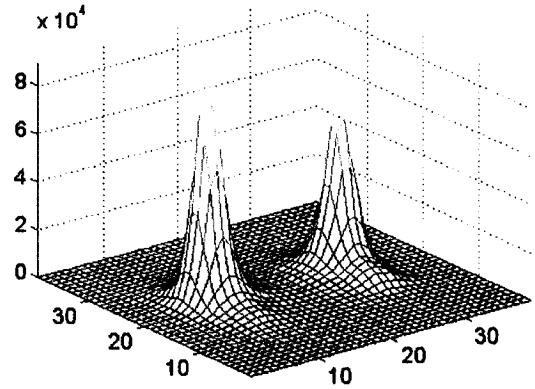

Fig. 7.27. This is 3D display of the coincidence image Fig. 7.26.

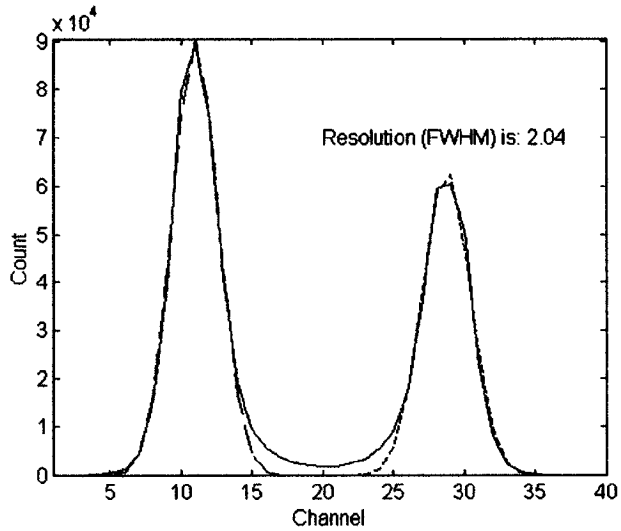

Fig. 7.28. The solid line of the plots is the image (Fig. 7.26) profile. The dash line is the Gaussian fitting result.

Fig. 7.29 shows the coincidence image that is created with "fish-net" LUT method (LUT mode-C). Since the crystal elements of 10 × 10 in the near layer and 9 × 9 in the far layer can be located, the coincidence image is displayed in the 19 × 19 bins. Mode-B and C have same efficiency, both are higher than mode-A. The spatial resolution in mode-C is a little worse than mode-B. However, (10 × 10) + (9 × 9) = 181 elements are located in mode-C, compared with (19 × 19 = 361) elements located by mode-B. Mode-C will be time-efficient in image reconstruction process.

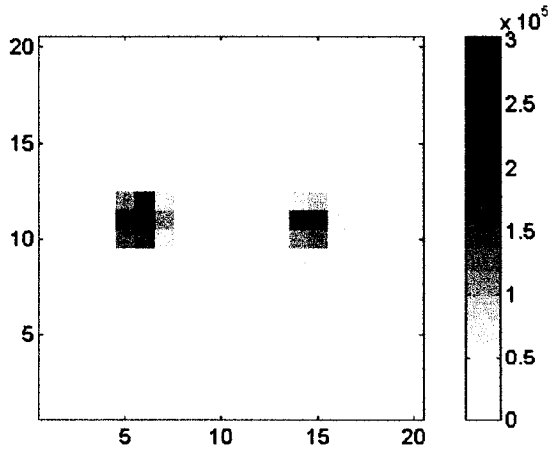

Fig. 7.29. The coincidence image by applying the LUT mode-C.

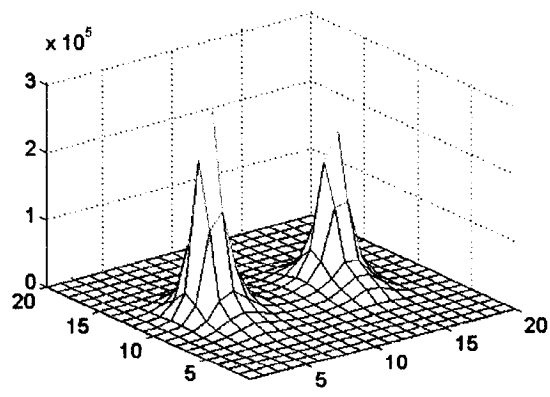

Fig. 7.30. This is 3D display of the coincidence image Fig. 7.29.

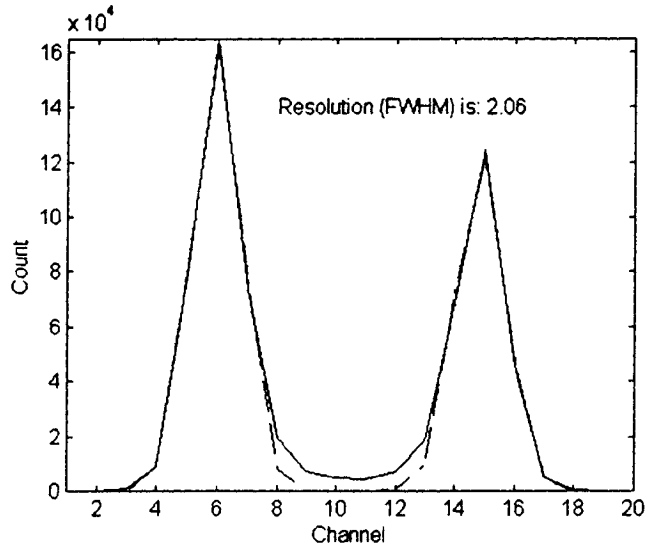

Fig. 7.31. The solid line of the plots is the image (Fig. 7.29) profile. The dash line is the Gaussian fitting result.

7.4.4 Block Effect due to the Distortion Image Segmentation

TABLE 7.1. COMPARISON OF METHODS OF CRYSTAL ELEMENTS SEGMENTATION

Method	Numbers of Segment [#1]	Spatial Resolution [#2]	Block Efficiency [#3]
Intrinsic	256 × 256 = 65536	1.80 mm	76.6 %
LUT1: Rectangular Region: Only Peaks (Hot Spots)	10 × 10 + 9 × 9 = 181	1.86 mm	21.8 %
LUT2: Rectangular Region: Peaks and Valleys	19 × 19 = 361	2.04 mm	76.6 %
LUT3: Fish-Net Region	10 × 10 + 9 × 9 = 181	2.06 mm	76.6 %

[#1] Numbers of the crystal segments in each detector are based on three different look-up-tables.
[#2] Spatial resolutions are measured from Guassian fitting results.
[#3] Block Efficiency = (counts chosen for coincidence) / (block total collected counts). The experimental hardware low-energy threshold was 150 keV. The digital data range of each channel was from 0 to 255. The total energy range was from 0 to 1023. The software low-energy threshold was 200 (about 300 keV); the software high-energy threshold was 1023.

Table 7.1 summarizes the spatial resolutions and block efficiencies based on different distortion look-up-tables. As can be seen, the intrinsic resolution is about 1.8 mm with efficiency of 76.6 %. After applying LUT1 segmentation method, the resolution of the coincidence detector pairs is close to the intrinsic resolution, but the detecting efficiency is decreased dramatically. This efficiency degradation is caused by rejecting the coincidence valley-valley and valley-peak pairs from the two opposite detectors. The spatial resolutions in LUT2 and LUT3 methods are almost the same; they also have the same efficiency. However, the positions of the fishnet segments are corresponding to the real locations of the crystal elements. This method also gives a clear and accurate crystal near-far layer depth-of-interaction information.

By applying the fish-net segmentation method, the spatial resolution is degraded about 14.4% compared with the intrinsic resolution. This degradation is mainly due to the block effect from the fish-net segmentation.

Based on (1.7), the spatial resolution is affected by the block effect - the uncertainty in determining the event location by using the multiple element/PMT decoding and the electronics decoding. In our design, the far layer crystal elements are decoded from reading the corresponding near layer elements. We also use position readout electronic circuit to decode the event position on PMT windows. According (1.7), we have:

$$\Gamma_{INSTR} = \sqrt{\left(\frac{d}{2}\right)^2 + (0.0022D^2) + s^2 + b_{INSTR}{}^2} \tag{7.9}$$

$$\Gamma_{LUT3} = \sqrt{\left(\frac{d}{2}\right)^2 + (0.0022D^2) + s^2 + b_{FISHNET}{}^2} \tag{7.10}$$

Here, d = 2.1 mm, which is the width of the crystal element. D = 100 mm, which is the detector separation. Γ_{INSTR} is the intrinsic resolution; b_{INSTR} is the block effect due to the near-far layer decoding and the electronics decoding. $\Gamma_{FISHNET}$ is the resolution resulting from applying the fishnet (LUT3) segmentation method; $b_{FISHNET}$ is the block effect due to the near-far layer decoding, electronics decoding, and the fish-net segmentation.

From Table 7.1, we have:

$$\Gamma_{INSTR} = 1.80\,\text{mm}, \quad \Gamma_{FISHNET} = 2.06\,\text{mm} \tag{7.11}$$

So:

$$b_{FISHNET}{}^2 = b_{INSTR}{}^2 + 1.0 \tag{7.12}$$

As:

$$b_{FISHNET}{}^2 = b_{INSTR}{}^2 + b_{SEGMENT}{}^2 \tag{7.13}$$

where $b_{SEGMENT}$ is the block effect due to the fish-net segmentation.

So we have:

$$b_{SEGMENT} = 1.0\,\text{mm} \tag{7.14}$$

In conclusion, applying the distortion look-up-table to segment crystal elements will degrade the spatial resolution. From (7.14), the segmentation of assigning one segment to one crystal element will degrade the spatial resolution about 1.0 mm.

7.5 Intrinsic Timing Resolution Measurements

Timing resolution of the PEM-II system was measured by general fast-slow coincidence technique. The experimental setup is as same as described in 3.2.2. Fig. 7.32 is the measured PEM system timing resolution. By applying the new timing amplifier circuit, the system timing resolution is about 10.3 ns.

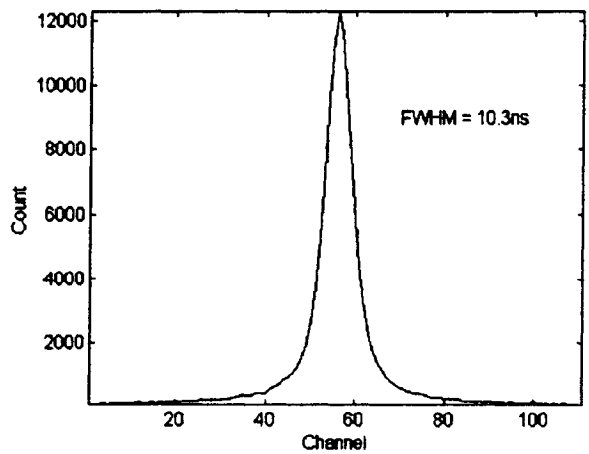

Fig. 7.32. This is timing resolution results. The data channel of the Multichannel Analyzer is calibrated as 1.47 ns per channel.

7.6 Project Overview and the Significance of the Results

7.6.1 Project Summary

Current challenges in developing dedicated positron emission tomography systems for metabolic breast mammography and small animal are to achieve high spatial resolution and high efficiency. In nowadays technology, less than 2.0-mm spatial resolution is mandatory in developing a new PEM and animal PET instrument. Meanwhile, high efficiency is also essential in the system overall performance.

In this project, we designed and developed prototype detectors by using position-sensitive photomultiplier tubes and pixelated bismuth germanate (BGO) crystals with depth encoding scheme to detect and localize gamma rays. The following methods were applied in BGO crystal processes.

1. Crystal cutting - We cut each crystal block with diamond saw into small elements of 2.1 mm x 2.1 mm (2.2 mm pitch) on two opposite faces. The elements on one face of the block offset by half the crystal pitch from those on the opposite face in both X and Y dimensions. The depths of two layers were 11.5 mm and 6.5 mm, respectively. The middle solid space between the two layers was 2 mm. With this crystal structure, one bit of depth-of-interaction can be located by identifying the layer in which gamma ray occurs.
2. Crystal polishing - After cutting process, the cut surfaces of the crystal elements become very rough. These rough surfaces will degrade the crystal light collection. We used acid etching method to chemically polish the cut surfaces.
3. Crystal encapsulating - After cutting and acid polishing processes, the crystal blocks become extremely fragile. We chose to encapsulate epoxy-compound mixture to coat the crystal elements. The epoxy-compound is opaque and high reflective. It will isolate the light photon transmitting to nearby elements, and also highly recover the light photon by the white-epoxy reflection.
4. Crystal block separating - By evaluating the crystal irradiation images, we found that the edge elements of the crystal far layer cannot be identified; these elements can further cause image distortion. So these edge elements were removed after encapsulating the crystal near layer. We also found that the middle uncut region which connects the block near and far layers causes image blurring - the far layer

crystal elements cannot be clearly identified, and there is significant near-far layer overlap in the flood irradiation images. We decided to eliminate this uncut region - the pseudo discrete crystal blocks were cut along the middle solid space into two discrete segments.

5. Crystal coupling - After eliminating the crystal uncut region, we mechanically polished the cut surfaces, and glued them together. Then the finished two-layer discrete crystal blocks were optically coupled to the PS-PMT windows.

The electronic circuits we designed and developed to readout the signal from PS-PMTs includes high-voltage dividers, anode resistor chains, position readout circuits, and last-dynode timing circuits. We investigated a method of combining four PS-PMTs with simple X^+, X^-, Y^+, Y^- outputs to simplify the position recording.

In order to optimize the electronics performance, we theoretically analyzed the position readout circuits. We first discussed the signal-to-noise ratios in different position readout schemes. Then we examined the truncation and round-off errors by applying the Root-Sum-Square analysis and the uniform distribution simulation methods. We gave the criteria on gain adjustment, and also inspected gain balanced adjustment issue.

The detectors were constructed in the structure of arrays (two in the system) - modules (four in each array) - units (four in each module). The basic unit with one crystal and one PS-PMT was formed as field replaceable. Each module has its own position readout and timing trigger circuits. One module from a detector array can have coincidence with any module in the opposite detector array; the coincidences from different module pairs can be processed simultaneously.

The list-mode data were acquired and analyzed with C and MATLAB. The coincidence data were examined with three different distortion look-up-tables. Our new prototype detectors have 1.8-mm intrinsic spatial resolutions. The timing resolution is about 10.3 ns. The proposed detector has a field-of-view of 88 mm x 88 mm.

7.6.2 Significance of the Results

The crystal segmentation along the middle uncut region was firstly suggested by Dr. Thompson. It turned out to be a significant improvement in the crystal identification.

Previously, the crystal identification was based on side-irradiation distortion images (Fig. 7.3). I was questioned by researches during the IEEE conference and criticized by paper reviewers on obtaining the distortion look-up-table based on the side-irradiation images. When I presented the flood irradiation result (Fig 4.7) in the later IEEE conference, the far layer of the crystal elements cannot be clearly identified due to the image blurring caused by the middle uncut region. The dual-layer crystal structure was questioned whether it is working, even though we suggested the result could be improved if we eliminate the uncut region. One critique from the paper reviewer was that it would not improve but degrade the flood irradiation image if we eliminate that region, because the intact region actually facilitates the light photon transferring from the far layer, via the near layer, to the PMT window. This is based on that the index-of-refraction (IOR) of BGO is about 2.15, but the IOR of the optical coupling is about 1.47. So a significant amount of the light photons generated from the far layer will be bounced back without transmitting to the near layer. We agreed that the light bounced back could be a problem. It was unclear during that time that whether we should eliminate the uncut region. So I spent time in investigating mathematical methods to identify two-layer elements from image like Fig. 4.7. Overall results were not very satisfactory even though the technique like using banded energy window can improve identifying the far layer elements.

It happened that we had two broken crystal segments. The segments were broke from a crystal block exactly along the uncut region during the cutting process. We eliminated the uncut region by using sand papers, polished the cut surfaces, and glue the two segments back with optical coupling. The flood irradiation image with this crystal block (Fig. 7.11) shows a remarkable improvement. After these experiments, we cut several crystal blocks with a relatively thick diamond saw blade to eliminate the middle uncut region. The irradiation images from these segmented crystals exhibited the results that the near-far layer crystal elements can be clearly identified.

Crystal processing is one of the crucial procedures in PET detector development. In chapter II, we presented some dedicated detector designs for small animal and metabolic breast imaging. Most of these designs, such as MicroPET [32], MicroPET II [66], MicroPET P4 [65], and Sherbrooke APD PET [122], constructed crystal block by gluing

individual crystal elements to form a large, discrete crystal array. The crystal block of these systems commonly has only one layer.

In small animal PET and PEM study, the detecting diameter is relatively small compared with commercial whole body PET scanner. In order to achieve high spatial resolution, the crystal element normally has small elongation, like 10-mm. With only one layer crystal design, the system efficiency will be limited. In crystal large elongation design, depth-of-interaction information is mandatory in order to obtain high resolution. Our crystal block has two layer elements. The depth of the whole crystal block is 20-mm. As the far and near layer of the crystal elements have half pitch offset, we can identify the two layer element according to their geometry. So we can obtain one bit of depth-of-interaction information. Since each crystal layer has relatively short elongation, we can also achieve high spatial resolution. Overall, the system has high resolution and high efficiency performances.

Due to the processing difficulty, crystal with small dimensions and polished surfaces are relatively expensive. Constructing crystal block from individual elements is also time consuming. In our design, we pixelated the crystal by cutting a relatively large block into a dual-layer pseudo-discrete pattern. After acid etching and epoxy encapsulating, we cut the crystal into two separated layers. By polishing and gluing them together, we obtain a discrete dual-layer crystal array. This process turns out to be a time-efficient and cost-effective crystal processing procedure.

Avalanche photodiodes (APDs) instead of PMTs have been employed in some small animal PET scanners. Like Sherbrooke APD PET, the technique of each small discrete crystal coupling to each APD element was used to achieve high spatial resolution. Due to coupling ratio between crystals and their readout is 1:1, the block effect is zero. In these designs, complex front-end circuits and parallel signal processing electronics were needed to read out signals from each individual unit. One disadvantage of using APD is that it has very a low gain ($\sim 10^2$) compared with a high PMT gain ($\sim 10^6$). A high-gain preamplifier circuit is needed to read out signal from an APD. So the signal-to-noise ratio in the front-end electronics could be an issue. Compared with PMT, the gain of APD is very temperature sensitive. The whole APD detectors should be in the precise

temperature controlled environment. Also at present, APDs are relatively expensive and fewer products available compared with PMTs.

As described in the chapter II, some groups [80][85][87] have investigated and developed the multi-layer crystal pattern with phoswich design in their PET detectors. In these designs, a "delayed-charge-integration" (DCI) technique in the position electronics is applied to identify crystal layers. In our design, the different layer can be identified from one distortion look-up-table as the near and far layers are geometric offset. The position readout electronics is relatively simple compared with the DCI design.

By using BGO scintillation crystal, we achieved a spatial resolution about 1.8 mm. In the latest IEEE medical imaging conference, our presentation demonstrated a very advanced result in BGO applications. Some systems, like MicroPET P4, reached near 1.0-mm spatial resolution by using 1 mm × 1 mm × 10 mm individual LSO crystals. This indicates we will achieve both high spatial resolution and high efficiency by using small dimension, dual layer LSO crystal in the future development.

7.7 Original Contribution and Future Work

Positron emission tomography development is a comprehensive field. My Ph.D. project is supervised by Dr. C. J. Thompson, cooperated with many collegers in the Research Computing Laboratory (RCL) of the Montreal Neurological Institute (MNI), and with help from many friends in the industries and academia across Canada and abroad. The Ph.D. project is based on the previous knowledge of PEM-I and ANIPET system developed by Dr. Thompson in MNI. Many works in my project were based on the previous theoretical and experimental results investigated in the Dr. Thompson's lab. Many fundamental concepts in PET design, like crystal dual-layer structure, crystal cutting process, crystal acid etching solution and process, digital processing electronics, data readout and processing software, were all well investigated and developed by Dr. Thompson et al. in the RCL of MNI.

My contributions in the project include following several aspects.

1. In electronics development:

A method of combining four PS-PMTs with simple four X^+, X^-, Y^+, Y^- outputs was developed. This method was published in the IEEE Transaction on Nuclear Science (IEEE-TNS). The position readout and timing trigger circuits were designed and developed for the study.

2. In theoretical analysis:

A guideline on optimizing gain adjustment to the front-end position readout circuit was investigated and will be published in IEEE-TNS (paper was accepted). The truncation and round-off errors in the irradiation image processes were examined by applying the Root-Sum-Square analysis and the Uniformity Distribution methods. Gain balanced adjustment issue in the X^+, X^-, Y^+, Y^- analog signal channels were also investigated.

3. In scintillation crystal processing:

Crystal cutting process was improved after consulting Mr. Eddie Campo in the Workshop of the Physics Department. Several polishing processes were applied to mechanical polishing the segment cut surfaces. An effort was taken in understanding epoxy chemical properties and crystal encapsulating process. The ratio of the epoxy compound with white paste, the application of crystal release agent were investigated and tested in the crystal encapsulating process. Many experiments had been done regarding the uncut region elimination, crystal side-irradiation and flood irradiation. The irradiation image demonstrates that the dual-layer BGO crystal elements (with 2.2-mm pitch) can be clearly identified. The intrinsic resolution of the system is about 1.8 mm. These advanced results in BGO crystal applications were presented in the IEEE conference and published in IEEE-TNS.

4. In imaging software processing:

A software "ImgProc.m" on irradiation image spectrum and histogram analysis, crystal identification process, and coincidence image process was programmed with MATLAB. Three different of distortion look-up-tables were examined. As a result, block effect due to the crystal segmentation was discussed.

To construct a prototype PEM-II system for clinical trials remains in future development. The front-end electronic circuits need to be tested and verified in the system. A large amount related software need to be developed for data acquisition and image reconstruction.

It is crucial to extend the sensitive areas of PET detectors to their periphery in order to overcome the difficulty in imaging near the patient's chest wall. The new PS-PMT R7600-C12 has narrower peripheral dead region compared with PS-PMT R3900 which was used for PEM-I detector. The mechanical design for PEM-II detector enclosure should ensure the detector having small peripheral dead region. As the PMT envelope is in high voltage potential (negative 800 volts), safety issue in PMT packaging and operating should be taken in great concern.

In Chapter VI, the position readout circuits are theoretically analyzed in order to optimize the performance of the front-end electronics. The truncation and round-off errors were discussed in the irradiation image process. This error analysis was not complete. It needs further work in mathematical modeling and software simulating to fully generalize and investigate on the noise issues.

Block effect is the uncertainty in determining the event location caused by using PMTs decoding multiple crystal elements and using electronics decoding the position output from PMTs. Even though some PET systems use single crystal coupled to single APD element and combined with single electronics readout to eliminate the block effect, the overall designs are very complex. So the majority of the detector designs still use decoding technique. In Chapter VII-7.4.4, we briefly discussed the block effect issue. Only the block effect due to the distortion image segmentation was discussed. The more detailed block effect remains in the future for further investigation.

APPENDIX

A. BGO Crystal Cutting Record (Original)

Crystal ID: C010726-02
Date: Jul 26-27, 2001
Operator: Nan Zhang

I. 11.5mm Depth Cuts, Direction One

Cut Steps	Position (mm)	Dial Rot Counts	Fine Dial Number	Blades Total	Blades Order	Comments
Set Home	0.2	0	2.0 White			
1st Cut	2.34	2	5.4 White	3	#8-#6-#7	
2nd Cut	8.64	6	8.4 White	3	#8-#6-#7	
3rd Cut	14.94	7	1.4 Red	3	#8-#6-#7	

Blades: #8: B010726-08, #6: B010726-06, #7: B010726-07

II. 11.5mm Depth Cuts, Direction Two

Cut Steps	Position (mm)	Dial Rot Counts	Fine Dial Number	Blades Number	Blades Order	Comments
Set Home	0.2	0	2.0 White			
1st Cut	2.34	2	5.4 White	3	#1-#4-#3	
2nd Cut	8.64	6	8.4 White	3	#1-#4-#3	
3rd Cut	14.94	7	1.4 Red	3	#1-#4-#3	

Blades: #1: B010724-01, #4: B010724-04, #3: B010724-03

III. 7.5mm Depth Cuts, Direction One

Cut Steps	Position (mm)	Dial Rot Counts	Fine Dial Number	Blades Number	Blades Order	Comments
Set Home	0.2	0	2.0 White			
1st Cut	1.30	1	5.0 Red	3	#8-#2-#7	
2nd Cut	7.60	6	8.0 Red	3	#8-#2-#7	
3rd Cut	13.90	7	1.0 White	3	#8-#2-#7	
4th Cut	20.20	6	4.0 White	1	#8	

Blades: #8: B010726-08, #2: B010724-02, #7: B010726-07

IV. 7.5mm Depth Cuts, Direction Two

Cut Steps	Position (mm)	Dial Rot Counts	Fine Dial Number	Blades Number	Blades Order	Comments
Set Home	0.2	0	2.0 White			
1st Cut	1.30	1	5.0 Red	3	#8-#2-#7	
2nd Cut	7.60	6	8.0 Red	3	#8-#2-#7	
3rd Cut	13.90	7	1.0 White	3	#8-#2-#7	
4th Cut	20.20	6	4.0 White	1	#7	

Blades: #8: B010726-08, #2: B010724-02, #7: B010726-07

B. The Encapsulating Record of Mixing Epoxy EPO-TEK 301-2 with White Paste REN DW-0131 (Original)

Balance Instruments:

Lab Balance: Sartorius AG, type: AC 210S, Readability of 0.001 g.

1. Epoxy EPO-TEK 301-2 two compounds mixture:
   Mix ratio of Part A and Part B: **100:35 Parts by Weight**

EPO-TEK 301-2 Mixture Record

	Weight Balance Read	Mixed Ratio
Epoxy Part A:	4.4821	100
Epoxy Part B:	1.5779	35.20

Experiment Mix Ratio of Part A and Part B is: 100 : 35.20

2. Epoxy and white paste mixture:
   Mix ratio of epoxy two parts components with white paste: **100:200 Parts by weight**

Mixture Record of White Paste REN DW-0131 with EPO-TEK 301-2

	Weight Balance Read	Mixed Ratio
Epoxy:	1.8539	100
Paste:	3.7164	200.46

3. Vacuum removing air bubbles processing

Degas epoxy and white pigment mixture for 30 minutes in a vacuum chamber.
Release the vacuum two times to break small air bubbles which formed on the surface. Redo the degassing process each time for 10 minutes.
Move out the epoxy and pigment mixture from vacuum chamber. Stand for another 10 minutes to allow tiny unreleased air bubbles to dissolve into the solution.

Nan Zhang
Jan 25, 2002

C. Printed Circuit Broads of PMT Socket, Position Integrator, Fast Timing Readout, and Main Amplifier Buffer Circuits

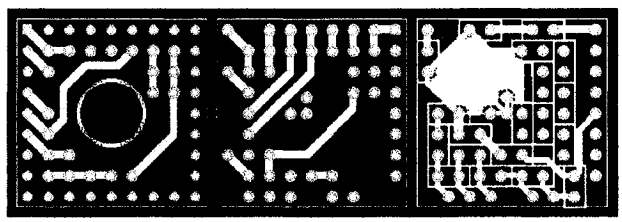

Top layer of the PMT socket

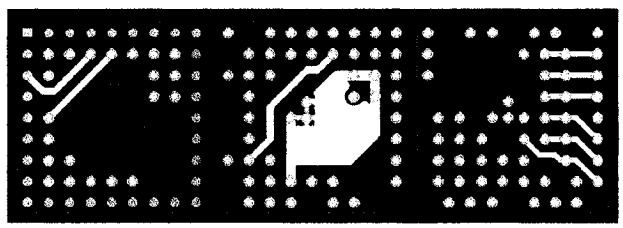

Bottom layer of the PMT socket

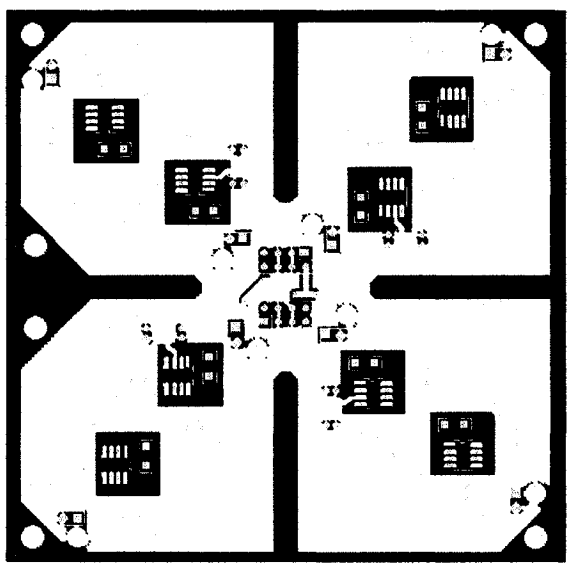

Top layer of the position readout circuit

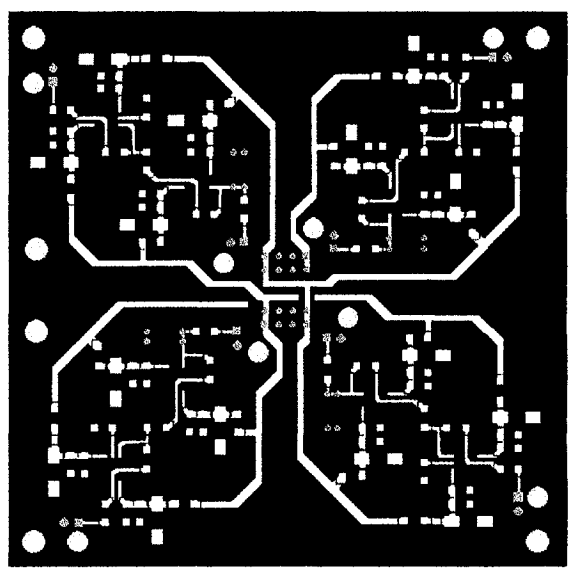

Bottom layer of the position readout circuit

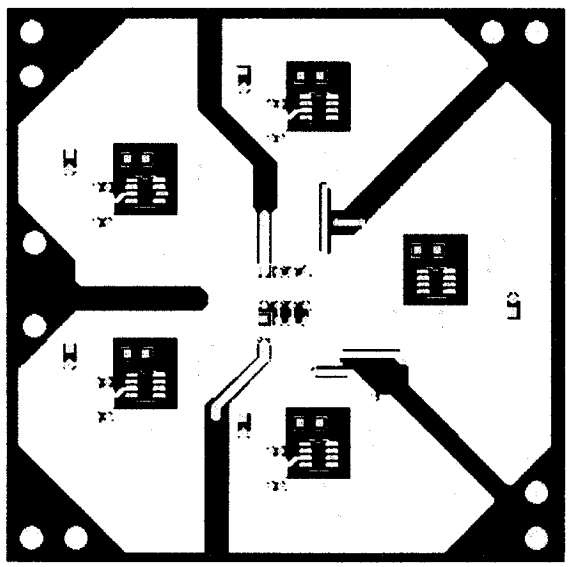

Top layer of the fast timing circuit

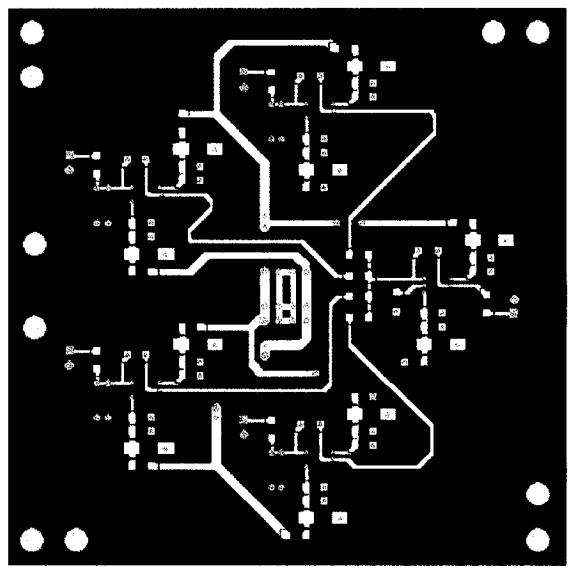

Bottom layer of the fast timing circuit

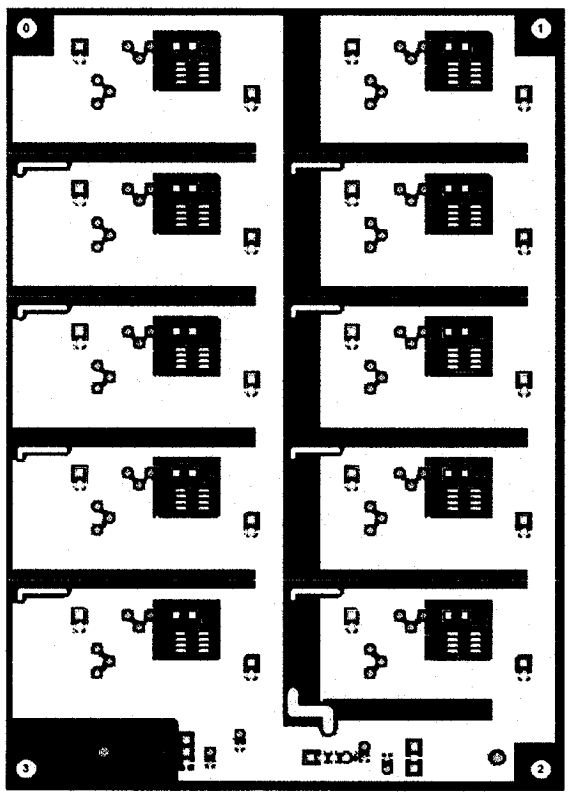

Top layer of the main buffer circuit

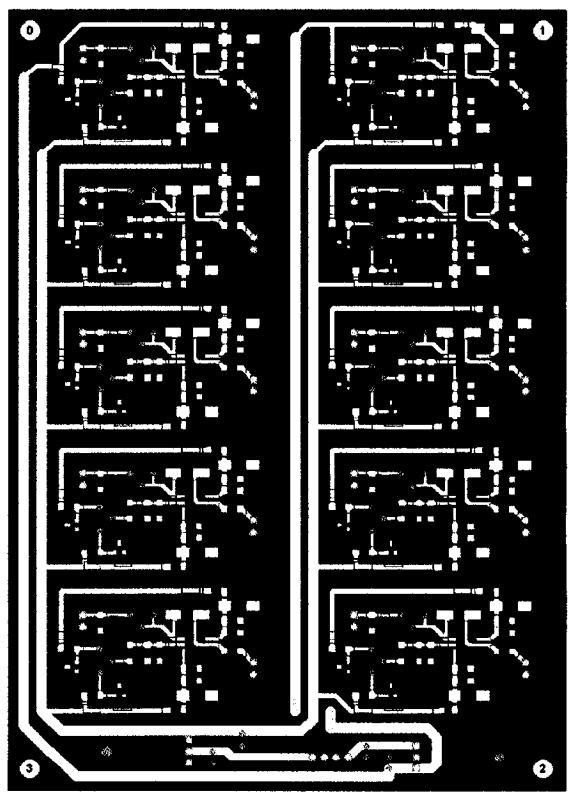

Bottom layer of the main buffer circuit.

D. Crystal Identification Image Processing

M-file Structure

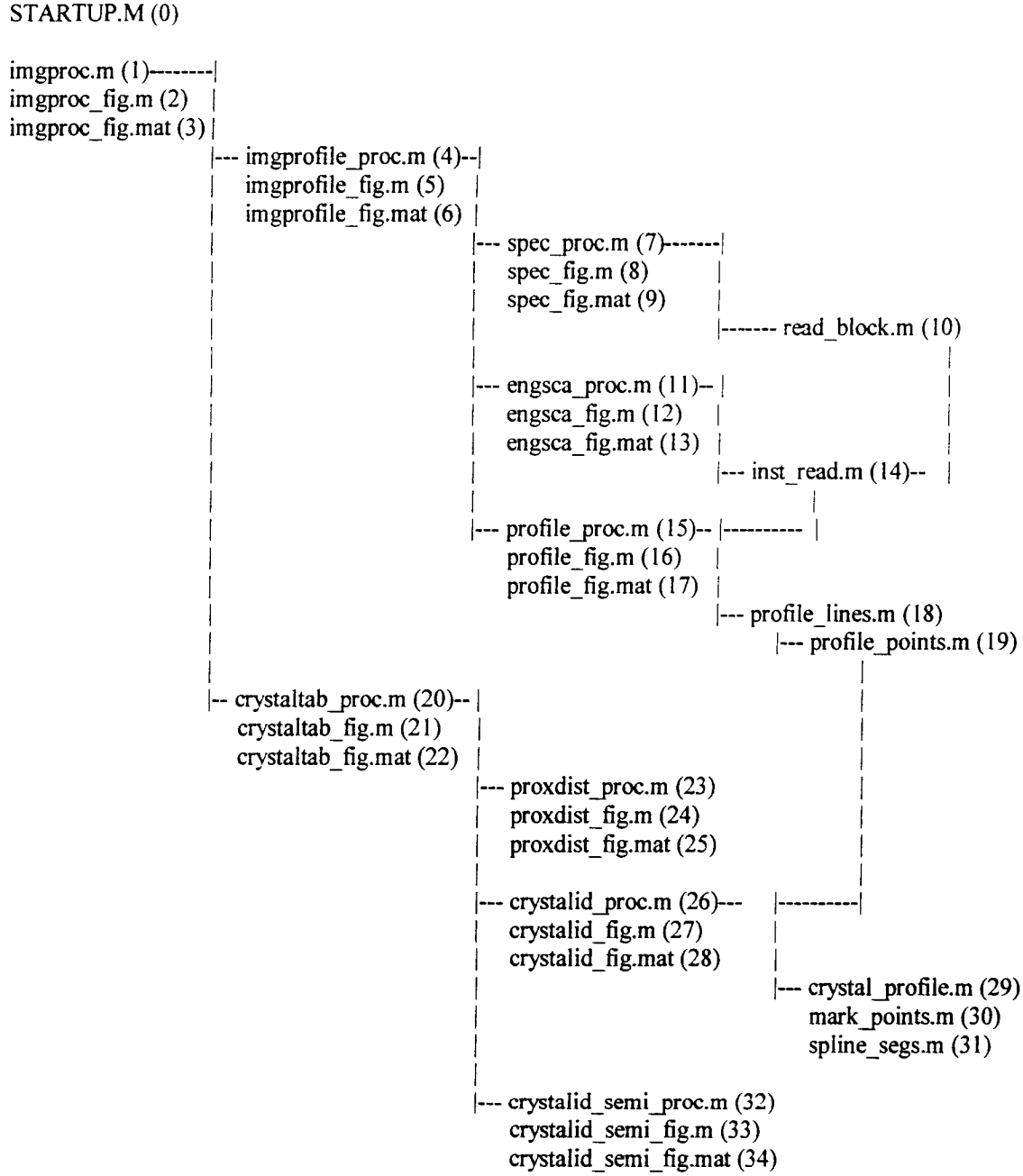

M-file Global Variable

STARTUP.M (0)

imgproc.m (1)

```
  global RESADC
  global HEADOFFSET
  global BLOCK_SIZE
  global REC_BYTE REC_CH
  global LowEngGate
  global SPECXYSIZE SPECENGSIZE SPECBIN
  global INSTSIZE INSTSCALE
```

imgproc_fig.m (2)
imgproc_fig.mat (3)

imgprofile_proc.m (4)

```
  global SpecListMat
  global EngScaSel
  global ProfileSel
```

imgprofile_fig.m (5)
imgprofile_fig.mat (6)

spec_proc.m (7)

```
  global LowEngGate
  global SpecListMat
  global SaveXY SaveEng
```

spec_fig.m (8)
spec_fig.mat (9)

read_block.m (10)

```
  global RESADC
  global BLOCK_SIZE REC_CH
```

engsca_proc.m (11)

```
  global LowEngGate
  global EngScaSel
  global SaveSca1 SaveSca2 SaveSca3 SaveSca4 SaveSca5
SaveSca6
```

engsca_fig.m (12)
engsca_fig.mat (13)

inst_read.m (14)

```
   global BLOCK_SIZE
   global HEADOFFSET
   global REC_BYTE
   global INSTSIZE INSTSCALE
```

profile_proc.m (15)

```
   global LowEngGate
   global SPECENGSIZE
   global INSTSIZE
   global ProfileSel
   global ImgProf XRowMat YRowMat XColMat YcolMat
   global RowLineHdl ColLineHdl
```

profile_fig.m (16)
profile_fig.mat (17)

profile_lines.m (18)

```
   global INSTSIZE
   global ProfileSel
   global ImgProf XRowMat YRowMat XColMat YcolMat
   global RowLineHdl ColLineHdl
```

profile_points.m (19)

```
   global INSTSIZE
```

crystaltab_proc.m (20)

```
   global INSTSIZE
   global ProxDistSel
   global CrystIDSel
   global CIDSemiSel
   global SumProx SumDist
```

crystaltab_fig.m (21)
crystaltab_fig.mat (22)

proxdist_proc.m (23)

```
   global INSTSIZE
   global ProxDistSel ProxDistMark
   global SideImg1 SideImg2 SideImg3 SideImg4 SumProx SumDist
   global ImgProf
```

proxdist_fig.m (24)
proxdist_fig.mat (25)

crystalid_proc.m (26)

```
   global INSTSIZE
   global CrystIDSel
```

```
   global SumProx SumDist
   global ProfileHdl
   global XCrossMark YcrossMark
   global HdlMarkProx HdlMarkDist
   global XFishNet YFishNet NetCrossX NetCrossY
   global HdlNetProx HdlNetDist
```

crystalid_fig.m (27)
crystalid_fig.mat (28)

crystal_profile.m (29)

```
   global INSTSIZE
   global SumProx
   global ProfileHdl
```

mark_points.m (30)

```
   global INSTSIZE
```

spline_segs.m (31)

```
   global XCrossMark YcrossMark
   global HdlMarkProx HdlMarkDist
   global XFishNet YFishNet NetCrossX NetCrossY
   global HdlNetProx HdlNetDist
```

crystalid_semi_proc.m (32)

```
   global CIDSemiSel
   global INSTSIZE
   global SumProx SumDist
   global XProxLine YproxLine
   global HdlProxLineProx HdlProxLineDist
   global XDistLine YdistLine
   global HdlDistLineProx HdlDistLineDist
   global XFishNet YFishNet NetCrossX NetCrossY
   global HdlNetProx HdlNetDist
```

crystalid_semi_fig.m (33)
crystalid_semi_fig.mat (34)

Array structure

- **Very confusing MATLAB coordinate system**

Locations in an image are expressed in two different coordinate systems in MATLAB software. One is "the pixel coordinate system"; another is "the spatial coordinate system".

In the pixel coordinate system, image is treated as a grid of discrete elements, orders from top to bottom and left to right. For pixel coordinates, the first component *r* (the row) increases downward, while the second component *c* (the column) increases to the right. Pixel coordinates are integer values and range between 1 and the length of the row or column.

The really confusing difference is largely a matter of convention: the order of the horizontal and vertical components is reversed in the notation for these two systems. Pixel coordinates are expressed as (*r, c*), while spatial coordinates are expressed as (*x. y*).

- **Cross mark locations and their display handles - *XCrossMark, YCrossMark, HdlMarkProx, HdlMarkProx***

They are all combined by 20 column vectors. Each vector has 11 scalars which represents 11 cross points. The vector structure of row cross points (from row profile lines) is kept the same as that of column cross points (from column profile lines).

XCrossMark(:, 1:10) represents row cross points (from row profile lines).

XCrossMark(:, 11:20) represents column cross points (from column profile lines).

The initial values of these arrays are:

XCrossMark = zeros(11, 20);
YCrossMark = zeros(11, 20);

HdlMarkProx = zeros(11, 20);
HdlMarkDist = zeros(11, 20);

- **Fish-Net lines - *XFishNet, YFishNet***

Total 20 fish-net lines (row direction) form the crystal identification look up table. Each fish-net has 12 (2 * *INSTSIZE*) elements. So *XFishNet*, *YFishNet* have 20 vectors, which represents 20 fish-net lines.

The Initial values of *XFishNet*, *YFishNet* are:

XFishNet = zeros(20, 2 * *INSTSIZE*);
YFishNet = zeros(20, 2 * *INSTSIZE*);

- **Fish-Net display handles – *HdlNetProx, HdlNetDist***

Each fish-net is combined with 20 line segments handles. For fish-net line number *#num*, *HdlNetProx*(*#num*, 1:20) represents 20 continues line handles which generated by MATLAB "line" function.

The initial values are:

HdlNetProx = zeros(20, 20);
HdlNetDist = zeros(20, 20);

- **Fish-Net "net cross points" – *NetCrossX, NetCrossY***

Each line in fish-net has 21 points which are jointed with other lines. Or we can say each line is combined with 20 line segments, so still we have total 21 cross points. The locations of these cross points are represented as *NetCrossX, NetCrossY*. For line number *#num*, vector *NetCrossX*(*#num*, 1:21) records 21 X coordinates of cross points. NetCrossY(*#num*, 1:21) records 21 Y coordinated of cross points.

The initial value are:

NetCrossX = zeros(20, 21);
NetCrossY = zeros(20, 21);

- **Proximal layer picked splines - *XProxLine, YProxLine***

The proximal/distal layers display handles : *HdlProxLineProx HdlProxLineDist*

The Distal layer picked splines – *XDistLine, YDistLine*

The proximal/distal layers display handles: *HdlDistLineProx HdlDistLineDist*

The proximal/distal layer picked splines will display in the both proximal and distal layers. The display positions are same, but they have different display handles.

There are 11 row and 11 column lines from proximal image. There are 10 row and 10 column lines for distal image. Each line corresponds the valley of the crystal elements. Each spline has 2**INSTSIZE* elements with one display handle in the proximal layer and one display handle in the distal layer.

The initial values are:

XProxLine = zeros(22, 2**INSTSIZE*);
YProxLine = zeros(22, 2**INSTSIZE*);

HdlProxLineProx = zeros(1, 22);
HdlProxLineDist = zeros(1, 22);

XDistLine = zeros(20, 2**INSTSIZE*);
YDistLine = zeros(20, 2**INSTSIZE*);

HdlDistLineProx = zeros(1, 20);
HdlDistLineDist = zeros(1, 20);

REFERENCES

[1] J. A. Sorensen, M. E. Phelps, *Physics in nuclear medicine*. Second edition, Grune & Stratton, 1987, pp. 31, 33, 143-151, 178, 434.

[2] SNM, *What is nuclear medicine? What is PET?* Society of nuclear medicine, 1850 Samuel Morse Dr. Reston, VA 20190 U.S.A., www.snm.org, Jul. 2002.

[3] M. E. Phelps, J. C. Mazziotta, H. R. Schelbert, Positron emission tomography and autoradiography: principles and applications for the brain and heart, New York: Raven Press, 1986, pp. 210, 237, 240, 393.

[4] R. Nutt, "The history of positron emission tomography," *Mol. Imag. Biol.*, vol. 4, num. 1, pp. 11-26, Jan. 2002.

[5] P.-J. Toussaint, Improved strategies for the evaluation of cerebral bloodflow and cerebrovascular reserve capacity using dynamic positron emission tomography. Ph.D. Thesis. Neurology and Neurosurgery, McGill University, 1999, pp. 10.

[6] M. Dahlbom, *Nuclear medicine instrumentation, lecture note,* Division of Nuclear Medicine, Department of Molecular and Medical Pharmacology, UCLA school of Medicine, 2001.

[7] D. R. Carter, *Photomultiplier handbook*, Burle Industries, Inc., Tube Products Division, 1000 New Holland Ave., Lancaster, PA 17601, U.S.A., Oct. 1989, pp. 3, 40, 94, 136.

[8] Philips Photonics, *Photomultiplier tubes - principles & applications*, Philips Photonics, 100 Providence Pike, Slaterville, RI 02876, U.S.A., 1994, pp. 1-24, 6-24, 6-30.

[9] W. W. Moses and S. E. Derenzo, "Empirical observation of resolution degradation in positron emission tomography utilizing block detectors," *J. Nucl. Med.*, vol. 34, pp. 101p, 1993.

[10] S. E. Derenzo, "Precision measurement of the annihilation point spread distributions for medically important positron emitters," Proceeding of the 5th International Conference on Positron Annihilation, pp. 819-823, 1979.

[11] Z. H. Cho, "Positron ranges obtained from biomedical important positron emitting radionuclides," *J. Nucl. Med.*, vol. 16, pp. 1174-1176, 1975.

[12] S. E. Derenzo, SPIE, vol. 671, Physics and Engineering of Computerized Multidimensional Imaging and Processing, pp. 232-243, 1986.

[13] M. Deutch, "Annihilation of positrons," *Progress in Nuclear Physics*, vol. 3, pp. 131-158, 1953.

[14] S. de Benedetti, C. E. Cowan, W. R. Konneker, "On the angualr distribution of two-photon annihilation radiation," *Phys. Rev.* vol. 77, pp. 205-212, 1950.

[15] C. Grupen, "Tutorials - interaction of charged particles: scintillation in materials," The Detector Physics and Applications Center, University of Siegen, Postfach, D-57068 Siegen.

[16] M. E. Phelps, J. C. Mazziotta, H. R. Schelbert, Positron emission tomography and autoradiography : principles and applications for the brain and heart, New York : Raven Press, 1986

[17] E. J. Hoffman, "Examination of the role of detection systems in quantitation and image quality in PET," *IEEE Trans. Nucl. Sci.*, vol. 33, no. 1, pp. 420-424, 1986.

[18] H. Ishibashi, K. Shimizu, K. Susa, "Cerium doped GSO scintillator and its applications to position sensitive detectors," *IEEE Trans. Nucl. Sci.*, vol. 36, no. 1, pp. 170-172, 1989.

[19] Hamamatsu, *Photomultiplier tubes and assemblies for scintillation counting & high energy physics,* Hamamatsu Photonics K.K., Electron Tube Center, 314-5, Shimokanzo, Toyooka-village, Iwata-gun, Shizuoka-ken, 438-0193, Japan, May, 1998, pp. 12-13.

[20] Hamamatsu, *Photomultiplier tubes*, Hamamatsu Photonics K.K., Electron Tube Center, 314-5, Shimokanzo, Toyooka-village, Iwata-gun, Shizuoka-ken, 438-0193, Japan, Oct. 1998, pp. 5.

[21] Anger H., "Scintillation Camera," *Rev. Sci. Inst.*, Vol 29, no.1, 1958.

[22] C. J. Thompson, K. Murthy, Y. Picard, I. N. Weinberg, and R. Mako, "Positron emission mammography (PEM): A promising technique for detecting breast cancer," *IEEE Trans. Nucl. Sci.*, vol.42, pp.1012-1017, Aug. 1995.

[23] C. J. Thompson, P. Sciascia, K. Murthy, S. Kecani, L. Nikinnen, E. Campo, J.-F.Corbett, Y. Bercier, M. Diksic, P. Cumming "ANIPET: a versatile PET scanner for imaging small animals," *IEEE Nucl. Sci. Symp. Conference Record,* vol. 2, pp. 1264-1267, 1998.

[24] Y. Picard, C. J. Thompson, "Motion correction of PET images using multiple acquisition frames," *IEEE Trans. Nucl. Sci.*, vol. 16, pp. 137-144, April 1997.

[25] Y. Picard, C. J. Thompson, "Determination of the centroid of interaction of crystals in block detectors for PET," *IEEE Trans. Nucl. Sci.*, vol. 41, pp. 1464-1468, Aug. 1994.

[26] K. Murthy, C. J. Thompson, C. Liu-Hinz, D. Jolly, "A study of the light output and energy resolution of small BGO crystals," *IEEE Nucl. Sci. Symp. Conference Record*, vol. 3, pp. 1352-1356, 1995.

[27] K. Murthy, D. Jolly, M. Aznar, C. J. Thompson, P. Sciascia, A. Loutfi, R. Lisbona, J. H. Gagnon, "Quantification in positron emission mammography (PEM) with planar detectors: contrast resolution measurements using a custom breast phantom and novel spherical hot-spots," *IEEE Trans. Nucl. Sci.*, vol. 46, pp. 2192 -2196, Dec. 1999.

[28] K. Murthy, C. J. Thompson, I. N. Weinberg, F. M. Mako, "Measurement of the coincidence response of very thin BGO crystals," *IEEE Trans. Nucl. Sci.*, vol. 41, pp. 1430-1435, Aug. 1994.

[29] N. Zhang, C. J. Thompson, C. L. Thompson, K. Q. Nguyen, "Improving the performance of small planar detectors for dedicated PET instruments," *IEEE Trans. Nucl. Sci.*, vol. 49, pp. 111-115, Feb. 2002.

[30] N. Zhang, C. J. Thompson, D. Togane, F. Cayouette, K. Q. Nguyen, M.-L. Camborde, "Design of front-end electronic circuits for dedicated PET detectors," *IEEE Nucl. Sci. Symp. Conference Record*, vol. 4, pp. 1984-1987, Nov. 2002.

[31] Photonis, (former Philips Photonics), Avenue Roger Roncier, Z.I. Beauregard, B.P. 520, 19106 BRIVE Cedex, France. URL: www.photonis.com

[32] S. R. Cherry, Y. Shao, R. W. Silverman, K. Meadors, S. Siegel, A. Chatziioannou, J. W. Young, W. Jones, J. C. Moyers, D. Newport, A. Boutefnouchet, T. H. Farquhar, M. Andreaco, M. J. Paulus, D. M. Binkley, R. Nutt, M. E. Phelps, "MicroPET: a high resolution PET scanner for imaging small animals," *IEEE Trans. Nucl. Sci.*, vol. 44, pp. 1161-1166, Jun. 1997.

[33] W. H. Sweet, "The use of nuclear disintegration in diagnosis and treatment of brain tumors," *N. Engl. J. Med.* 245:875-878, 1951.

[34] Y. L. Yamamoto, C. J. Thompson, M. Diksic, E. Meyer, and W. H. Feindel, "Positron emission tomography," *Radiat. Phys. Chem.*, vol. 24. No. 3/4, pp. 385-403, 1984.

[35] M. J. Weber, R. R. Monchamp, "Luminescence of $Bi_4Ge_3O_{12}$ spectral and decay properties," *J. Appl. Phys.* vol. 44, pp. 5495-5499, 1973.

[36] O. H. Nester, C. Y. Huang, "Bismuth germanate: a high-z gamma-ray and charged particle detector," *IEEE Trans. Nucl. Sci.*, NS-22:68, 1975.

[37] M. Dahlbom, M. A. Mandelkem, E. J. Hoffman, "Hybrid HgI2-GSO detector for PET," *IEEE Trans Nucl Sci* 32: 533-537, 1985.

[38] L. Eriksson, C. Bohm, M. Kesselberg, "A four ring positron camera system for emission tomography of the brain," *IEEE Trans Nucl Sci* 29: 539-543, 1985.

[39] S. Surti, J. S. Karp, R. Freifelder, F. Liu, "Optimizing the performance of a PET detector using discrete GSO crystals on a continuous lightguide," *IEEE Trans. Nucl. Sci.*, vol. 47, pp. 1030 -1036, Jun. 2000.

[40] C. L. Melcher, Lutetium orthosilicate single crystal scintillator detector. U.S. Patent 4,598,080, Sep. 18, 1990

[41] C. L. Melcher, Lutetium orthosilicate single crystal scintillator detector, U. S. Patent 5,025, 151, Jun. 19, 1991.

[42] M. Moszynski, M. Kapusta, D. Wolski, M. Szawlowski, W. Klamra, "Energy resolution of scintillation detectors readout with large area avalanche photodiodes and photomultipliers," *IEEE Trans. Nucl. Sci.*, vol. 45, pp. 472-477, Jun. 1998.

[43] M. E. Casey, and R. Nutt, "A multicrystal two dimensional BGO detectors system for positron emission tomography," *IEEE Trans. Nucl. Sci.*, vol. NS-33, pp. 460-463, 1986.

[44] M. E. Casey, R. Nutt, T. D. Gouglass, *Two-dimensional photon counting position encoder system and process.* U.S. Patents, 4,743,764 & 7,749,863, May 10, 1988.

[45] S. R. Cherry, M. P.Tornai, C. S. Levin, S. Siegel, and E. J. Hoffman, "A comparison of PET detector modules employing rectangular and round photomultiplier tubes," *IEEE Trans. Nucl. Sci.*, vol. 42, pp. 1064 –1068, Aug. 1995.

[46] CPS Innovation, 810 Innovation Drive, Knoxville, TN 37932 U.S.A.

[47] M. L. Eriksson, C. Bohm, S. Kesselberg, S. Holte, M. Bergatrom, and J. Litton, "Design studies of two possible detector block for high resolution positron emission tomography of the brain," *IEEE Trans. Nucl. Sci.*, vol. 34, pp. 344-347, Feb. 1987.

[48] S. Koke, Eriksson, J. E. Larsson, T. Ericson, H. Stjernberg, and P. Hansen, "A preliminary evaluation of a positron camera system using weighted decoding of individual crystals," *IEEE Trans. Nucl. Sci.*, vol. 35, pp. 730-734, Feb. 1988.

[49] M. Dahlbom, and E. J. Hoffman, "An evaluation of a two-dimensional array detector for high resolution PET," *IEEE Trans. Med. Imaging,* vol. 7, pp. 264 - 272, Dec. 1988.

[50] F. Daghighian, E. J. Hoffman, and S. C. Huang, "Quality control in PET systems employing 2-D modular detectors," *IEEE Trans. Nucl. Sci.*, vol. 36. Pp. 1034-1037, Feb. 1989.

[51] W. M. Digby, M. Dahlbom, and E. J. Hoffman, "Detector, shielding and geometric design factors for a high-resolution PET," *IEEE Trans. Nucl. Sci.*, vol. 37, pp. 664-670, Apr. 1990.

[52] J. G. Rogers, A. J. Taylor, M. F. Rahimi, R. Nutt, M. Andreaco, and C. W. Williams, "An impoved multicystal 2-D BGO detector for PET," *IEEE Trans. Nucl. Sci.*, vol. 1063-1068, Aug. 1992.

[53] H. Anger, "Scintillation Camera," *Rev. Sci. Inst.*, vol. 29, no.1, pp. 27-33, 1958.

[54] W.-H. Wong, "Positron camera detector design with cross-coupled scintillators and quadrant sharing photomultipliers," *IEEE Trans. Nucl. Sci.*, vol. 40, pp. 962-966, Aug. 1993.

[55] W.-H. Wong, J. Uribe, K. Hicks, and M. Zambelli, " A 2-dimensional detector decoding study on BGO arrays with quadrant sharing photomultipliers," *IEEE Trans. Nucl. Sci.*, vol. 41, pp. 1453-1457, Aug. 1994.

[56] The University of Texas, M. D. Anderson Cancer Center, 1100 Holcombe Boulevard, Houston, TX 77030, U.S.A.

[57] W.-H. Wong, G. Hu, N. Zhang, J. Uribe, J. Wang, H. Li, W. Lu, H. Baghaei, S. Yokoyama, "Front end electronics for a variable field PET camera using the PMT-quadrant-sharing detector array design," *IEEE Trans. Nucl. Sci.*, vol. 44, pp. 1291-1296, Jun. 1997.

[58] H. Li, W.-H. Wong, N. Zhang, J. Wang, J. Uribe, H. Baghaei, and S. Yokoyama, "Electronics for a prototype variable field of view PET camera using the PMT-quadrant-sharing detector array," *IEEE Trans. Nucl. Sci.*, vol. 46, pp. 546-550, Jun. 1999.

[59] Hamamatsu Photonics K.K., Electron Tube Center, 314-5, Shimokanzo, Toyooka-village, Iwata-gun, Shizuoka-ken, 438-0193, Japan.

[60] Burle Industries, Inc., Tube Products Division, 1000 New Holland Ave., Lancaster, PA 17601, U.S.A.

[61] G. Germano and E. J. Hoffman, "A study of data loss and mispositioning due to pileup in 2-D detectors in PET," *IEEE Trans. Nucl. Sci.*, vol. 37, pp. 671-675, Apr. 1990.

[62] G. Germano and E. J. Hoffman, "Investigation of count rate and deadtime characteristics of a high resolution PET system," *J. Comput. Assist. tomogr.*, vol. 12, pp. 836-346, 1988.

[63] H. Kume, S. Muramatsu, M. Iida, "Position sensitive photomultiplier tubes for scintillation imaging," *IEEE Trans. Nucl. Sci.*, vol. 33, pp. 359-363, Feb. 1986.

[64] S. R. Cherry, Y. Shao, S. Siegel, R. W. Silverman, E. Mumcuoglu, K. Meadors, and M. E. Phelps, "Optical fiber readout of scintillator arrays using a multi-channel PMT: a high resolution PET detector for animal imaging," *IEEE Trans. Nucl. Sci.*, vol. 43, pp. 1932-1937, Jun. 1996.

[65] Y. C. Tai, A. Chatziioannou, S. Siegel, J. Young, D. Newport, R. N. Goble, S. R. Cherry, R. E. Nutt, "Preliminary evaluation of the microPET P4: a PET system dedicated to small animal imaging," *IEEE Nucl. Sci. Symp. Conference Record*, vol. 3, pp. 21/51, 2000.

[66] A. Chatziioannou, Y. Tai, Y. Shao, N. Doshi, B. Silverman, K. Meadors, and S. R. Cherry, "Coincidence measurements on detectors for microPET II: a 1 mm/sup 3/ resolution PET scanner for small animal imaging," *IEEE Nucl. Sci. Symp. Conference Record*, vol. 3, pp. 21/1, 2000.

[67] C. M. Ankenbrandt, and E. M. Lent, "Increasing the light collection efficiency of scintillation counters," *The Rev. Sci. Instr.*, vol. 34, pp. 647-651, Jun. 1963.

[68] M. Cocchi, and A. Rota, "Light collection on a photocathode from a cylindrical scintillator," *Nucl. Instr. Meth.* vol. 46, pp. 136-140, 1967.

[69] X. Yao, "A study of light collection efficiency in scintillation detectors," *Nucl. Instr. Meth. Phys. Res.* Vol. 228, pp. 101-104, 1984.

[70] Cherry, Y. Shao, M. P. Tornai, S. Siegel, A. R. Ricci, and M. E. Phelps, "Collection of scintillation light from small BGO crystals," *IEEE Trans. Nucl. Sci.*, vol. 42 pp. 1058 -1063, Aug. 1995.

[71] G. Combey, and R. Meunier, "Test of a new 64 channel PMT for imaging," *Nucl. Inst. Meth.*, vol. A268, pp. 246-260, 1988.

[72] S. Siegel, R. W. Silverman, Y. Shao, and S. R. Cherry, "Simple charge division readouts for imaging scintillator arrays using a multi-channel PMT," *IEEE Trans. Nucl. Sci.*, vol. 43, pp. 1634 -1641, Jun. 1996.

[73] K. Q. Nguyen, C. J. Thompson, S. Kecani, L. Nikinnen, A. Ben el Fassi, A. Reader, N. Zhang, and M. Diksic, "Operational and performance report on ANIPET, a versatile PET scanner for laboratory animals," *IEEE Nucl. Sci. Symp. Conference Record*, vol. 3, pp. 21/60 -21/64, 2000.

[74] K. Murthy, D. Jolly, M. Aznar, C. J. Thompson, P. Sciascia, A. Loutfi, R. Lisbona, and J. H. Gagnon, "Quantification in positron emission mammography (PEM) with planar detectors: contrast resolution measurements using a custom breast phantom and novel spherical hot-spots," *IEEE Trans. Nucl. Sci.*, vol. 46, pp. 2192-2196, Dec. 1999.

[75] R. L. Clancy, C. J. Thompson, J. L. Robar, and A. M. Bergman, "A simple technique to increase the linearity and field-of-view in position sensitive photomultiplier tubes," *IEEE Trans. Nucl. Sci.*, vol. 44, pp. 494 -498, Jun. 1997.

[76] A. M. Bergman, C. J. Thompson, K. Murthy, J. L. Robar, and R. L. Clancy, "Co-registration of Positron Emission Mammography (PEM) images and X-ray," *IEEE Trans. Nucl. Sci.*, vol. 3, pp. 1812-1816, 1996.

[77] C. J. Thompson, K. Murthy, R. L. Clancy, J. L. Robar, A. Bergman, R. Lisbona, A. Loutfi, J. H. Gagnon, I. N. Weinberg, and R. Mako, "Imaging performance of PEM-1: a high resolution system for positron emission mammography," *IEEE Nucl. Sci. Symp. Conference Record*, vol. 2, pp. 1074-1078, 1995.

[78] J. L. Robar, C. J. Thompson, K. Murthy, R. L. Clancy, and A. M. Bergman, "Correction of spatial distortion, gain nonuniformity and efficiency variation in detectors for positron emission mammography," *IEEE Nucl. Sci. Symp. Conference Record*, vol. 2, pp. 1206-1210, 1996.

[79] K. Murthy, M. Aznar, A. M. Bergman, C. J. Thompson, J. L. Robar, R. Lisbona, A. Loutfi, and J. H. Gagnon, "Positron emission mammographic instrument: initial results," *Radiology*, vol. 215, pp. 280-285, 2000.

[80] T. Yamashita, M. Watanabe, K. Shimizu, H. Uchida, "High resolution block detectors for PET," *c* 37, pp. 589-593, Apr. 1990.

[81] National Semiconductor Catalog: "CLC401 - Fast setting, wideband high-gain monolithic Op amp," 1999.

[82] S. Siegel, J. J. Vaquero, L. Aloj, J. Seidel, E. Jagoda, W. R. Gandler, W. C. Eckelman, and M. V. Green, "Initial results from a PET/Planar small animal imaging system," *IEEE Trans. Nucl. Sci.*, vol. 46, pp. 571-575, Jun. 1999.

[83] M. Watanabe, T. Omura, H. Kyushima, Y. Hasegawa, and T. Yamashita, "A compact position-sensitive detector for PET," *IEEE Trans. Nucl. Sci.*, vol. 42, pp. 1090-1094, Aug. 1995.

[84] N. K. Doshi, R. W. Silverman, Y. Shao, and S. R. Cherry, "maxPET, a dedicated mammary and axillary region PET imaging system for breast cancer," *IEEE Trans. Nucl. Sci.*, vol. 48, pp. 811-815, Jun. 2001.

[85] J. Seidel, J. J. Vaquero, S. Siegel, W. R. Gandler, and M. V. Green, "Depth identification accuracy of a three layer phoswich PET detector module," *IEEE Trans. Nucl. Sci.*, vol. 46, pp. 485-490, Jun. 1999.

[86] J. Seidel, J. J. Vaquero, F. Barbosa, I. J. Lee, C. Cuevas, and M. V. Green, "Scintillator identification and performance characteristics of LSO and GSO PSPMT detector modules combined through common X and Y resistive dividers," *IEEE Trans. Nucl. Sci.*, vol. 47, pp. 1640-1645, Aug. 2000.

[87] J. J. Vaquero, J. Seidel, S. Siegel, W. R. Gandler, "Performance characteristics of a compact position-sensitive LSO detector module," *IEEE Trans. Nucl. Sci.*, vol. 17, pp. 967-978. Dec. 1998.

[88] M. Desco, M. V. Green, C. A. Johnson, J. Pascau, J. Seidel, and J. J. Vaquero, "Towards high performance small animal positron emission tomography", *2002 IEEE International Symposium on Biomedical Imaging*, 2002, pp. 369 -372.

[89] S. Nagai, M. Watanabe, H. Shimoi, H. Liu, and Y. Yoshizawa, "A new compact position-sensitive PMT for scintillation detectors," *IEEE Trans. Nucl. Sci.*, vol. 46, pp. 354-358, Jun. 1999.

[90] J. S. Karp, M. E. Daube-Witherspoon, "Depth-of-interaction determination in NaI(Tl) and BGO scintillation crystals using a temperature gradient," *IEEE Trans. Nucl. Sci.*, vol. 260, pp. 509-517, Oct. 1987.

[91] W. W. Moses, S. E. Derenzo, C. L. Melcher, R. A. Manente, " A room temperature LSO/PIN photodiode PET detector module that measures depth of interaction," *IEEE Trans. Nucl. Sci.*, vol. 42, pp. 1085-1089, Aug. 1995.

[92] C. Moisan, G. Tsang, J. G. Rogers, E. M. Hoskinson, "Performance studes of a depth encoding multicrystal detector for PET," *IEEE Trans. Nucl. Sci.*, vol. 43, pp. 1926-1931, Jun. 1996.

[93] A. Saoudi, d. Rouleau, R. Lecomte, M. Andreaco, M. Casey, R. Nutt, H. Dautet, "Performance studies of depth encoding multicrystal detectors using avalanche photodiodes," *J. Nucl. Med.*, vol. 39, pp. 92P, May 1998.

[94] L. R. Macdonald, M. Dahlbom, "Depth of interaction for PET using segmented crystals," *IEEE Trans. Nucl. Sci.*, vol. 45, pp. 2144-2148, Aug. 1998.

[95] R. S. Miyaoka, T. K. Lewellen, H. Yu, and D. L. MacDaniel, "Design of a depth of interaction (DOI) PET detector module," *IEEE Trans. Nucl. Sci.*, vol. 45, pp. 1069-1073, Jun. 1998.

[96] S. Yamamoto, and H. Ishibashi, "A GSO depth of interaction detector for PET," *IEEE Trans. Nucl. Sci.*, vol. 45, pp. 1078-1082, Jun. 1998.

[97] H. Murayama, H. Ishibashi, H. Uchida, T. Omura, and T. Yamashita, "Depth encoding multicrystal detectors for PET," *IEEE Trans. Nucl. Sci.*, vol. 45, pp. 1152-1157, Jun. 1998.

[98] M. Dahlbom, L. R. MacDonald, L. Erikson, M. Paulus, M. Andreaco, M. E. Casey, and C. Moyers, "Performance of a YSO/LSO phoswich detector for use in a PET/SPECT system," *IEEE Trans. Nucl. Sci.*, vol. 44, pp. 1114-1119, Jun. 1998.

[99] J. J. Vaquero, J. Seidel, S. Siegel, and M. V. Green, "A depth-encoding PET detector module with improved spatial sampling," *IEEE Nucl. Sci. Symp. Conference Record,* vol. 2, pp. 1255-1258, 1998.

[100] Hamamatsu catalog, *Position-Sensitive Photomultiplier Tube: Type-R3941 Tech. Inform.* Shimokanzo, Japan, Hamamatsu Photonics K. K., 1996.

[101] The figures are from Dr. Christopher J. Thompson's presentation: Preliminary clinical evaluation of an instrument for "positron emission mammography" in the detection of breast cancer, Montreal, QC H3A 2B4 Canada, Sep. 1997.

[102] The figures are from Dr. Christopher J. Thompson's presentation: *Initial experience with "ANIPET" a versatile PET scanner for imaging small animals,* Montreal, QC H3A 2B4 Canada, June 1999.

[103] K. Murthy, M. Aznar, C. J. Thompson, A. Loutfi, R. Lisbona, and J. H. Gagnon, "Results of preliminary clinical trials of the position emission mammography system PEM-I: a dedicated breast imaging system producing glucose metabolic images using FEG," *J. Nucl. Med.*, vol. 41, pp. 1851-1858, Nov. 2000.

[104] A. M. Bergman, C. J. Thompson, K. Murthy, "Technique to obtain positron emission mammography images in registration with x-ray mammograms," *Med. Phys.* vol. 25, pp. 2119-2129, 1998.

[105] J. L. Robar, C. J. Thompson, K. Murthy, R. Clancy, and A. M. Bergman, "Construction and calibration of detectors for high resolution metabolic breast cancer imaging," *Nucl. Inst. Meth. Phys. Res.* A392, pp. 402-406, 1997.

[106] R. Lecomte, J. Cadorette, P. Richard, S. Rodrigue and D. Rouleau, "Design and engineering aspects of a high resolution positron tomography for small animal imaging," *IEEE Trans. Nucl. Sci.*, vol. 41, pp. 1446-1452, Aug. 1994.

[107] R. Lecomte, J. Cadorette, S. Rodrigue D. Lapointer, and D. Rouleau, M. Bentourkia, R. Yao, P. Msaki, and G. Schmutz, "Initial results from the Sherbrooke avalanche photodiode PET scanner," IEEE Trans. Nucl. Sci., vol.42, pp. 1954-1957, June 1996.

[108] R. Lecomte, C. M. Pepin, M. D. Lepage, J.-F. Pratte, H. Dautet, and D. M. Binkley, "Performance analysis of phoswich/APD detectors and low-noise CMOS

preamplifiers for high-resolution PET systems", *IEEE Trans. Nucl. Sci.,* vol. 48, pp. 650-655, Jun. 2001.

[109] R. Lecomte, J. Cadorette, S. Rodrigue, M. Bentourkia, D. Rouleau, R. Yao, P. Msaki, "A high resolution PET scanner based on avalanche photodiode detectors for animal studies," *Engineering in Medicine and Biology Society, 1995., IEEE 17th Annual Conference,* vol. 1, pp. 525-526, 1995.

[110] R. Lecomte, A. Saoudi, D. Rouleau, H. Dautet, D. Waechter, M. Andreaco, M. Casey, L. Eriksson, R. Nutt, "An APD-based quad scintillator detector module with pulse shape discrimination coding for PET," *IEEE Nucl. Sci. Symp. Conference Record,* vol. 3, 1998.

[111] R. Lecomte, C. M. Pepin, D. Rouleau, A. Saoudi, M. S. Andreaco, M. Casey, R. Nutt, H. Dautet, P. P. Webb, "Investigation of GSO, LSO and YSO scintillators using reverse avalanche photodiodes," *IEEE Trans. Nucl. Sci.,* vol. 45, pp. 478-482, June 1998.

[112] A. Saoudi, C. M. Pepin, F. Dion, M. Bentourkia, R. Lecomte, M. Andreaco, M. Casey, R. Nutt, H. Dautet, "Investigation of depth-of-interaction by pulse shape discrimination in multicrystal detectors read out by avalanche photodiodes," *IEEE Trans. Nucl. Sci.,* vol. 46, pp. 462–467, June 1999.

[113] A. Saoudi, R. Lecomte, "A novel APD-based detector module for multi-modality PET/SPECT/CT scanners," *IEEE Trans. Nucl. Sci.,* vol. 46, pp. 479 -484, June 1999.

[114] C. M. Pepin, R. Lecomte, D. Krus, L. Perna, W. Novak, "Evaluation of reflective separators for arrays of small crystals used with avalanche photodiodes, " *IEEE Nucl. Sci. Symp. Conference Record,* vol. 1, pp. 6/52 -6/56, 2000.

[115] A. Chatziioannou, R. W. Silverman, K. Meadors, T. H. Farquhar, S. R. Cherry, "Techniques to improve the spatial sampling of MicroPET-a high resolution animal PET tomograph," *IEEE Trans. Nucl. Sci.,* vol. 47, pp. 422-427, Apr. 2000.

[116] C. M. Pepin, P. Berard, R. Lecomte, "Assessment of reflective separator films for small crystal arrays," *IEEE Nucl. Sci. Symp. Conference Record,* vol. 2, pp. 879-883, 2001.

[117] C. M. Pepin, P. Berard, R. Lecomte, "Comparison of LSO, LGSO and MLS scintillators," *IEEE Nucl. Sci. Symp. Conference Record.* vol. 1, pp. 124 -128, 2001.

[118] A. Saoudi, C. M. Pepin, R. Lecomte, "Study of light collection in multi-crystal detectors," *IEEE Trans. Nucl. Sci.,* vol. 47, pp. 1634 -1639, Aug. 2000

[119] M. D. Lepage, G. Leger, J. Cadorette, J.-D. Leroux, M. Otis, S. Rodrigue, R. Lecomte, "FPGA/DSP-based coincidence unit and data acquisition system for the Sherbrooke animal PET scanner," *IEEE Nucl. Sci. Symp. Conference Record,* vol. 2, pp. 12/173 -12/175, 2000.

[120] M. D. Lepage, G. Leger, J. Cadorette, S. Rodrigue, and R. Lecomte, "FPGA/DSP-based coincidence unit and data acquistion system for the Sherbrooke animal PET scanner," *IEEE Nucl. Sci. Symp. Conference Record,* pp. 12:173-175, 2000.

[121] M. D. Lepage, J.-D. Leroux, v. Selivanov, J. Cadorette, and R. Lecomte, "Design of a prototype read-time image reconstruction system for PET iamgeing," *IEEE Nucl. Sci. Symp. Conference Record,* M9C015, 2002.

[122] R. Lecomte, E. Croteau, M.-E. Gauthier, M. Archambault, A. Aliaga, J. Cadorette, J. Rousseau, F. Bénard, and M. Bentourkia, "Cardiac PET Imaging of Blood Flow, Metabolism and Function in Normal and Infarcted Rats," *IEEE Nucl. Sci. Symp. Conference Record,* M12-5, Nov. 2002.

[123] R. L. Clancy, C. J. Thompson, J. L. Robar, and A. M. Bergman, "A simple technique to increase the linearity and field-of-view in position sensitive photomultiplier tubes," *IEEE Trans Nucl Sci.* vol. 44: pp. 494-498, Jun. 1997.

[124] Hamamatsu catalog, *Position Sensitive Photomultiplier Tube R7600-00-C12 Preliminary Data.* Shimokanzo, Japan, Hamamatsu Photonics K. K., Oct. 1998.

[125] Alpha Spectra, Inc., 715 Arrowest Court, Grand Junction, CO 81505 U.S.A.

[126] M. P. Tornai, G. Germano, E. J. Hoffman, "Positioning and Energy response of PET block detectors with different light sharing schemes," *IEEE Trans. on Nucl. Sci.,* vol. 41, pp. 1458-1463, Aug 1993.

[127] South Bay Technology Inc., 1120 Via Callejon, San Clemente, CA 92673 U.S.A.

[128] J. L. Robar, Construction and Calibration of Detectors for High-Resolution Metabolic Breast Cancer Imaging, M.Sc Thesis, McGill University, pp. 43. Aug. 1996.

[129] Jorway Corporation, 27 Bond Street, Westbury, N.Y. 11590 U.S.A.

[130] F. Cayouette, C. Moisan, N. Zhang, and C. J. Thompson, "Monte Carlo modeling of scintillator crystal performance for stratified PET detectors with DETECT2000," *IEEE Trans. Nucl. Sci.,* vol. 49, pp. 624-628, June 2002.

[131] Epoxy Technology Inc., 14 Fortune Drive, Billerica, MA 01821 U.S.A.

[132] Vantico Inc., Ren Shape Tooling Systems, 4917 Dawn Ave., East Lansing, MI 48823 U.S.A.

[133] Ren Tooling Epoxy Resin systems, *Ren Tooling Epoxy Selector Guide - Technical Document*, Ren Shape Tooling Systems, 4917 Dawn Ave., East Lansing, MI 48823 U.S.A.

[134] Hope Jones, Epoxy Technology, 14 Fortune Drive, Billerica, MA 01821 USA, Tel: 978.667.3805 ext. 237, Fax: 978.667.4784. Email: hjones@epotek.com

[135] Hope Jones, "Epoxy Resin Crystallization", Technical Paper, Epoxy Technology, Inc.

[136] N. Zhang, C. J. Thompson, D. Togane, F. Cayouette, K. Q. Nguyen, "Anode Position and Last Dynode Timing Circuits for Dual-Layer BGO Scintillator With PS-PMT Based Modular PET Detectors", *IEEE Trans. Nucl. Sci.*, vol. 49, pp. 2203-2207, Oct. 2002.

[137] F. Cayouette, C. Moisan, and C. J. Thompson, "Monte-Carlo modeling of scintillator crystal performance for stratified PET detectors with DETECT2000," *IEEE Nucl. Sci. Symp. Conference Record*, vol. 4, pp. 1997-2001, 2002.

[138] Michael J. Hodgin, Engineering Manager of Epoxy Technology Inc. 14 Fortune Drive, Billerica, MA 01821 U.S.A., Tel: 978.667.3805, Fax: 978.663.9782.

[139] Toray Plastics (America), Inc., 50 Belver Avenue, North Kingstown, RI 02852, U.S.A., Tel: 401.294.4511, Fax: 401.294.2154.

[140] J. S. Huber, W. W. Moses, M. S. Andreaco, O. Petterson, "A LSO scintillator array for a PET detector module with depth of interaction measurement," *IEEE Trans. on Nucl. Sci.*, vol. 48, pp. 684-688, 2001.

[141] Labsphere Inc., North Sutton, NH 03260 U.S.A., Tel: 603.927.4266, Fax: 603.927.4694.

[142] Labshpere Inc. Technical guide - A Guide to reflectance coatings and materials, North Sutton, NH 03260 U.S.A.

[143] Labshpere Inc. Reflectance coating & materials selection chart, North Sutton, NH 03260 U.S.A.

[144] M. Cocci, A. Rota, "Light collection on a photocathode from a cylindrical scintillator," *Nucl. Inst. Meth.*, vol. 46, pp. 136-140, 1967.

[145] C. M. Ankebrandt, E. M. Lent, "Increasing the light collection efficiency of scintillation counters," *Rev. Sci. Instr.* vol. 34, pp. 647-651, 1963.

[146] F. W. Kulesza, "What Next for Epoxies?" Design Report, Epoxy Technology, Inc.

[147] A. L. Delmarsh, R. H. Estes, "Selecting Epoxies for Optical and Fiber Optic Applications," Technical Paper: GB-56, Epoxy Technology, Inc.

[148] T. W. Tamulevich, V. E. Moore, "The Significance of Glass Transition Temperature on Epoxy Resins for Fiber Optic Applications," Technical Paper, Epoxy Technology, Inc.

[149] M. J. Hodgin, "Re-working, Removing, and Decapsulating cured Epoxy," Technical Paper, Epoxy Technology, Inc.

[150] Marc Sato, Hamamatsu Corp. Private oral and email discussions on "HA coating from Hamamatsu", e-mail: msato@hamamatsu.com, Jul. 1, 2000.

[151] G. Brisebois, "LT1880 SOT-23 superbeta op amp saves board space in precision applications, design note 266," Linear Technology Corp., 2001.

[152] W. Kester, "Section 1, High speed operational amplifiers," High speed design techniques, Analog Device Inc. pp. 18, 1996.

[153] A. Pullia, R. Bassini, C. Boiano, S. Brambilla, "A cold discharge mechanism for low-noise fast charge amplifiers," *IEEE Trans. Nucl. Sci.*, vol. 48, pp. 530-534, June 2001.

[154] Protel 99SE, Protel DXP, Protel International Limited, PO Box 1876, Dee Why NSW2099, Australia, Phone: 61 2 9984 0016, Fax: 61 2 9984 0017.

[155] G. A. Korn, and T. M. Korn, *Mathematical Handbook for Scientists and Engineers*, McGraw-Hill, Inc., 1968, pp. 718.

[156] A. Jeffery, *Mathematics for engineers and scientists*, Chapman & Hall, 2-6 Boundary Row, London, SE1 8HN, UK, 1996, pp. 187. 745-747.

[157] J. H. Wilkinson, *Ronding Errors in Algebraic Processes*, Prentice-Hall, Inc., Englewod cliffs, N. J. U.S.A., 1963, pp. 4.

[158] R. R. Boyd, *Tolerance analysis of electronic circuits using MATLAB*, CRC Press LLC, 2000 Corporate Blvd. N. W., Boca Raton, Florida 33431, U.S.A., 1999, pp.1-7, 66.

[159] E. R. Mullins, Jr., and D. Rosen, *Probability and Calculus*, Bogden & Quigley, Inc., 19 North Brodaway, Tarrytown-on-Hudson, N. Y. 10591, U.S.A., 1971, pp. 192.

[160] MATLAB, Version 5.3.0.14912a (R11), June 19, 1999. The MathWorks, Inc., 3 Apple Hill Drive, Natick, MA 01760-2098, U.S.A.

[161] Carl de Boor, *Spline ToolBox for Use with MATLAB,* The Math Works, Inc., 24 Prime Park Way, Matick, Mass. 01760-1500, U.S.A., Jan 1994.

[162] T. Yamashita, M. Watanabe, K. Shimizu, and H. Uchida, "High Resolution block Detectors for PET," *IEEE Trans Nucl. Sci.* vol. 37, pp. 589-593, 1990.